Dissertation

submitted to the

Combined Faculty of Natural Sciences and Mathematics

of Heidelberg University, Germany

for the degree of

Doctor of Natural Sciences

Put forward by

Francisco Ignacio Aros Pinochet

born in Santiago, Chile

Oral examination: 6 of July 2021

Towards a Robust Detection of Intermediate-Mass Black Holes in Globular Clusters

Referees: Prof. Dr. Glenn van de Ven

apl. Prof. Dr. Rainer Spurzem

Abstract

Intermediate-mass black holes (IMBHs) with masses between 10^2 to 10^5 solar masses could be the key to explaining the formation of supermassive black holes in the centre of galaxies at high-redshift. The possible formation scenarios of IMBHs point towards dense stellar systems as favoured birthplaces. If an IMBH resides at the centre of such dense stellar systems, the surrounding stars under the IMBH's dynamical influence will show characteristic kinematic signatures. During the last two decades, the community has made significant efforts to find IMBHs through these kinematic signatures, particularly in the centre of the Milky Way's globular clusters (GCs). To date, however, no robust detection has been made.

In this thesis, we explore the internal dynamics of GCs to understand the current limitations for detecting IMBHs and propose alternative lines of evidence of their presence. With this purpose, we use numerical simulations of GCs with and without a central IMBH and apply commonly used dynamical models to estimate the mass of the possible central IMBH. We focus on the limitations of the dynamical modelling itself, particularly those due to common assumptions such as a constant velocity anisotropy and mass-to-light ratio. From an observational viewpoint, we explore the role of binaries in the observed kinematics and the connection between the observed binary fraction and the presence of an IMBH. Finally, we study the implications of the dynamical modelling limitations and the effects of binary systems on the scaling relations, which connect the mass of the central IMBHs with their host stellar system properties.

Zusammenfassung

Intermediäre Schwarze Löcher (IMBHs) mit Massen zwischen 10^2 bis 10^5 Sonnenmassen könnten der Schlüssel zur Erklärung der Entstehung von supermassereichen Schwarzen Löchern im Zentrum von Galaxien bei hoher Rotverschiebung sein. Die möglichen Entstehungsszenarien von IMBHs deuten auf dichte stellare Systeme als bevorzugte Geburtsorte hin. Befindet sich ein IMBH im Zentrum eines solchen dichten Sternsystems, zeigen die umgebenden Sterne unter dem dynamischen Einfluss des IMBHs charakteristische kinematische Signaturen. Während der letzten zwei Jahrzehnte hat die Gemeinschaft erhebliche Anstrengungen unternommen, IMBHs durch diese kinematischen Signaturen zu finden, insbesondere im Zentrum von Kugelsternhaufen (GCs) der Milchstraße. Bis heute ist jedoch noch kein robuster Nachweis gelungen.

In dieser Arbeit erforschen wir die interne Dynamik von GCs, um die derzeitigen Limitationen für die Detektion von IMBHs zu verstehen und schlagen alternative Nachweismöglichkeiten vor. Zu diesem Zweck verwenden wir numerische Simulationen von GCs mit und ohne zentrale IMBH und wenden herkömmliche dynamische Modelle an, um die Masse des möglichen zentralen IMBH abzuschätzen. Wir konzentrieren uns dabei auf die Grenzen der dynamischen Modellierung selbst, insbesondere auf die, die durch gängige Annahmen wie eine konstante Geschwindigkeitsanisotropie und ein Masse-zu-Licht-Verhältnis entstehen. Wir untersuchen die Rolle von Doppelsternen in der beobachtbaren Kinematik und den Zusammenhang zwischen dem Anteil der Doppelsternsysteme und der Anwesenheit eines IMBH. Schließlich untersuchen wir die Konsequenz der Limitationen der dynamischen Modellierung und die Auswirkungen von Doppelsternsystemen auf die Skalierungsrelationen, die die Masse des zentralen IMBHs mit den Eigenschaften ihres Hauptsternsystems verbinden.

Acknowledgements

The following thesis is the culmination of four years of work through my doctoral studies, a journey that has not been short of ups and downs. It was not a solo adventure, but one filled with companions that, in one way or another, supported me to arrive at this very point. Here I will briefly thank those who helped along the way.

My supervisors Anna Sippel, Alessandra Mastrobuono-Battisti and Glenn van de Ven, were instrumental in all the research I have done during my doctoral studies. Particularly Anna and Alessandra that without their continuous support, I wouldn't have arrived at this point. They deserve all the praise for being excellent supervisors. I would also like to thank my collaborators Paolo Bianchini and Abbas Askar, whose insight was of great help during my research. Last but not least, I would like to thank my scientific advisors Nadine Neumayer and Ralf Klessen, and Rainer Spurzem, for refereeing this thesis.

I would like to thank all the support of my family and friend back in Chile, that while being so far away, they gave me the energy to keep moving forward. In the same way, my Chilean friends in Heidelberg, Johanna, Felipe and Josefina, that made me feel at home after moving to Germany. And finally, the friend made along the way, Alina and Melanie, that keep me moving forward in the most challenging times.

To my parents, Marcela and Pedro, for 34 years of unconditional support.

Contents

Chapter 1

Introduction

Like many of the billions of stars in the Milky Way, the Sun travels following the rotational movement of our Galaxy. At roughly 8 kpc from us, at the very centre of the Milky Way, resides a supermassive black hole (SMBH) called Sagittarius A*. This massive point-like object, weighing 4 million times the mass of the Sun, is virtually invisible, however, we can observe its effects on the surrounding gas or stars.

Stars near the SMBH follow an orbital motion that can be approximated to first order by a Keplerian potential, such as the Earth moving around the Sun but with additional effects of general relativity. In the last two decades, the observation of stars orbiting the SMBH in the centre of the Milky Way has allowed us to measure its mass, confirm its point-like nature and even successfully test general relativity. These efforts to characterize the orbits of the stars surrounding the SMBH in the centre of our Galaxy, in particular by the researchers around Andrea Ghez and Reinhardt Genzel, have been awarded the Nobel prize in physics for the year 2020.

Not only the Milky Way has a SMBH in its centre: many other galaxies also host one. While only in the Milky Way we can observe individual stars orbiting the SMBH, the gravitational effect of the SMBH also modifies the movement of stars further away. Observations of the bulk motion of stars in the centres of other galaxies allow us to find a large number of these objects with masses beyond a billion times the mass of the Sun. We can also detect SMBHs via the signatures of gas accretion: infalling gas heats up and becomes extremely bright. These so-called active galactic nuclei also enable us to discover SMBHs at great distances, or early in the universe.

While we can detect SMBHs and measure their masses, the origin and growth of SMBHs is still not well understood. We know that massive stars can end their lives as a stellar mass black hole of a couple to tens of times the mass of the Sun, but growing such black holes to billions of solar masses is not straightforward, and requires extreme amounts of mass accretion. However, if black holes of a thousand to tens of thousands solar masses

exist, these black holes, or intermediate-mass black holes (IMBHs), can potentially serve as a seed for their supermassive counterpart.

In the last decades, significant efforts to detect IMBHs were undertaken. Whereas a few candidates have been identified, there is no clear evidence for them. Thanks to the many SMBHs observed up to today, it has become clear that there is a relation between their mass and the mass of its surrounding stellar system. This relation has served as a hint that IMBHs might exist in lower mass stellar systems such as dwarf galaxies or globular clusters.

Globular clusters (GCs) are dense and compact stellar systems that can be found in almost all galaxies. The GCs in the Milky Way have been the target for many studies trying to find an IMBH at their centres. While many candidates have been brought to light, there is no definitive evidence of the presence of an IMBH in any of them. Finding these elusive objects will help to better understand the formation and growth of their supermassive counterpart, while also bringing answers to the connection between the SMBH and its surrounding stellar system.

In this thesis, I will discuss the efforts taken towards finding IMBHs in the centres of GCs, while also exploring alternatives and improvements for their robust detection or ruling out their presence. But first, in the following pages, I will introduce many of the concepts and ideas I have touched in this brief motivation to my research.

1.1 Intermediate-mass Black Holes

Intermediate-mass black holes (IMBHs), with masses between 10^2 to $10^5\,M_\odot$, sit between the two known populations of black holes (BHs): stellar-mass and supermassive BHs. Since there is no exact definition for the corresponding mass limits, Table 1.1 shows the mass ranges assumed in this thesis for the different black hole populations.

While these are the commonly assumed limits, they are not strict and as it will be discussed in Section 1.1.2, BHs which are the remnants of massive and metal-free stars can have masses larger than $100\,M_\odot$ (see discussion in Section 1.1.2).

Despite the scarce observational evidence of IMBHs, there are many physical motivations for their existence. This Section will discuss the motivations and possible formation scenarios for the existence of IMBHs.

TABLE 1.1: Mass ranges for black holes.

Population	Mass range $[M_\odot]$
stellar-mass	$3 - 60$
intermediate-mass	$10^2 - 10^5$
supermassive	$> 10^5$

1.1.1 IMBHs as seeds of Supermassive Black Holes

All massive galaxies have a supermassive black hole (SMBH) with masses between $10^5\,M_\odot$ and $10^9\,M_\odot$ at their centres (see e.g., Kormendy & Ho, 2013; van den Bosch, 2016; Dullo et al., 2021). The first hints of their presence at the centres of galaxies date back to AGN observations in the 1960s, as gas accretion into a massive compact object was thought as the reason behind the short variability and high luminosity of AGNs. From the mid-1980s, the improvement in observational techniques allowed the search for SMBHs in nearby galaxies, with Messier 32 being the first one to be suggested to have a SMBH from its kinematics (Tonry, 1984, 1987). Since then, many SMBHs have been found using kinematic as well as their accretion signatures in AGNs (Kormendy & Ho, 2013).

The Milky Way is no exception, with a SMBH of $\sim 4\times10^6\,M_\odot$ in its centre and located at a distance of $\sim 8\,$kpc from the Sun (Ghez et al., 2008), making it the nearest SMBH. The first detections of the radio source known as Sgr A* at the Galactic centre (Balick & Brown, 1974; Brown & Liszt, 1984) were followed by different studies characterising the radio source, which first suggested a massive BH as the origin for the radio source (Rogers et al., 1994; Beckert et al., 1996). The kinematics of stars near Sgr A* provided the first evidence of a SMBH (Genzel et al., 1997; Ghez et al., 1998). Later on, the precise astrometric measurements of stellar orbits around the SMBH provided definitive proof (Ghez et al., 2000; Eckart et al., 2002). Sgr A* has become the single most studied SMBH, where recent observations of the orbits of stars around Sgr A* (in particular the second pericentre passage of the S2 star) precisely proved general relativity effects on their orbits (Gravity Collaboration et al., 2018a,b). As it is the case in many other galaxies as well (e.g., Georgiev & Böker, 2014), the Milky Way's central SMBH is surrounded by a nuclear star cluster, a dense cluster of approximately tens of million stars (see Neumayer et al., 2020, for a review).

Despite the many SMBHs discovered at the centres of galaxies and the unique laboratory that is provided by Sgr A*, there is little we know about the origin and growth of SMBHs. How fast SMBHs grow in the early universe is particularly relevant due to observations of ultraluminous AGNs at redshifts of $z > 6$ that could host SMBHs of $\sim 10^9\,M_\odot$ (see e.g., Mortlock et al., 2011; Wu et al., 2015; Bañados et al., 2018). Whereas these observations are just the tip of the iceberg, as they are biased towards to the most massive BHs, their existence implies strong constraints on the formation scenarios and growth of SMBHs.

The question is, then, how fast can a seed BH grow in the early universe? If we take a $100\,M_\odot$ black hole as an example and leave it to accrete at the Eddington limit[1] continuously, it will grow to a mass of $M_\bullet = 10^9\,M_\odot$ in about $0.7 - 0.8\,$Gyr (Haiman, 2013; Inayoshi et al., 2020). Under these conditions, it would be possible to have a large

[1]The Eddington limit is the maximum luminosity at which the outwards radiation pressure and inwards gravitational force are in equilibrium.

SMBH at $z \sim 6$. However, Bañados et al. (2018) show that for the highest redshift SMBH found so far (J1342+0928, with a mass of $M_\bullet = 8 \times 10^8\,M_\odot$ and at $z = 7.54$, which corresponds to an age of the univers about $\sim 0.6\,\mathrm{Gyr}$), accretion at the Eddington rate requires a seed BH of $\sim 2000\,M_\odot$ already in the first 70 Myr of the universe (roughly $z \sim 38$). Both cases assume a continuous accretion at the Eddington limit during the whole time of growth; however, this might not necessarily be the case, as the accretion rate can also vary over time (Haiman, 2013; Inayoshi et al., 2020). While episodes of super- and hyper-Eddington accretion may happen during the BH growth (Haiman, 2013; Inayoshi et al., 2020); these also require specific conditions beyond the focus of this thesis.

The alternative is to start with a more massive seed. Whereas the $100\,M_\odot$ black hole from the previous example is a possible remnant of the first stars, more massive black holes could have formed (Volonteri, 2010; Haiman, 2013; Inayoshi et al., 2020). The formation of IMBHs with masses of $1000\,M_\odot$ in the early universe provides an alternative solution for the SMBH growth's timing problems.

1.1.2 Formation scenarios for IMBHs

There are different paths for the formation of BHs with masses larger than $100\,M_\odot$. Some are only possible under the early universe's conditions, whereas others could still happen later on or within the local universe's conditions.

The pristine conditions of the primordial gas help form massive and metal-free stars called Population III stars. Pop III stars in the range of $25 < M_*/M_\odot < 140$ can leave a remnant BH of masses $10 < M_\bullet/M_\odot < 100$ (Zhang et al., 2008; Volonteri, 2010). For Pop III stars in the range of 140 to $260\,M_\odot$, pair-instability supernovae can entirely disrupt the star without leaving any remnant (Volonteri, 2010). On the other hand, higher masses stars can directly collapse into a BH (Madau & Rees, 2001; Volonteri, 2010). In particular, if the fragmentation of the collapsing primordial gas is halted, a supermassive star could form and directly collapse into an IMBH of $10^4\,M_\odot$; however, the conditions for suppressing fragmentation are rare (see, Inayoshi et al., 2020). Note that the initial formation of a supermassive star is an intermediate step of the "direct collapse" scenario of a massive gas cloud (see Greene et al., 2020, and references therein).

A more promising path for forming an IMBH is through a runaway collision (or collapse) in the centre of dense stellar systems, such as GCs and nuclear star clusters. In these systems, collisions are common due to their high stellar density (Portegies Zwart et al., 1999; Portegies Zwart & McMillan, 2002, and references therein). Furthermore, simulations of dense young clusters (see e.g., Portegies Zwart et al., 2004; Gürkan et al., 2004; Rizzuto et al., 2021) show that stellar collisions can build a very massive star ($M_* \sim 500 - 1000\,M_\odot$) in $\sim 10 - 50\,\mathrm{Myr}$, a star that can ultimately end in an IMBH of

$M_\bullet \sim 100-500\,M_\odot$. For this process to ocurr, it is necessary to achieve central densities of $\rho > 10^6\,M_\odot/\mathrm{pc}^3$ (Giersz et al., 2015; Rizzuto et al., 2021). The presence of primordial binaries can enhance the build-up of the very massive star or subsequent IMBH (Giersz et al., 2015), in particular binaries of massive stars ($M_* > 15\,M_\odot$) (González et al., 2021). Mapelli (2016) and Spera & Mapelli (2017) show that it is impossible to form an IMBH at solar metallicity through runaway collapse; however, it can happen at lower metallicities of $Z \lesssim 0.02 Z_\odot$, which is a metallicity that many Galactic GCs have (Harris, 1996, 2010 edition). This is also true at the metal-free conditions of the first Myrs of the universe (Inayoshi et al., 2020).

Alternatively, Giersz et al. (2015) show that the runaway process can happen without the need of forming a very massive star. Instead, a series of collisions and mergers of stellar remnants, mainly stellar-mass black holes, can drive the build-up of an IMBH. This process begins after the first supernovae and requires forming a BH subsystem within the dense stellar system. Moreover, this process requires densities of $\rho > 10^8\,M_\odot/\mathrm{pc}^3$. In the simulations done by Giersz et al. (2015), 20% of their simulated clusters had significant BH growth and formed an IMBH via this process.

If the stellar system is not dense enough at the core or if the runaway process was not efficient enough to grow an IMBH, a single BH could grow over time through mass transfer from a binary companion and dynamical encounters (Miller & Hamilton, 2002; Giersz et al., 2015). This so-called "slow" scenario happens later on in the stellar system evolution and becomes important once the dense stellar system undergoes core-collapse (Giersz et al., 2015).

The recent observation of the gravitational wave signal GW190521, from a binary BH merger that resulted in a BH of $M_\bullet = 142\,M_\odot$ (Abbott et al., 2020a,b), gives additional support for the "fast" (runaway) and "slow" scenarios. One, if not both, progenitors with estimated masses of $M_\bullet = 85\,M_\odot$ and $M_\bullet = 66\,M_\odot$ fall in the BH mass gap of pair-instability supernovae ($50-135\,M_\odot$ Belczynski et al., 2016). These BHs could have formed via previous mergers, which has motivated a new look on the runaway collision scenario in star clusters (Fragione et al., 2020; González et al., 2021; Rizzuto et al., 2021; Liu & Lai, 2021).

1.1.3 Scaling relations at lower BH masses

The masses of SMBHs appear to follow a correlation with their host galaxies' different properties, particularly with the host galaxy's central velocity dispersion. Ferrarese & Merritt (2000) and Gebhardt et al. (2000) first showed that SMBHs ranging from 10^6 to $10^9\,M_\odot$ follow a tight correlation with the host galaxy's central velocity dispersion, known as the $M_\bullet - \sigma$ relation. The correlation is indeed remarkable as the sphere of influence of the SMBH, which is the region where the central black hole dominates the

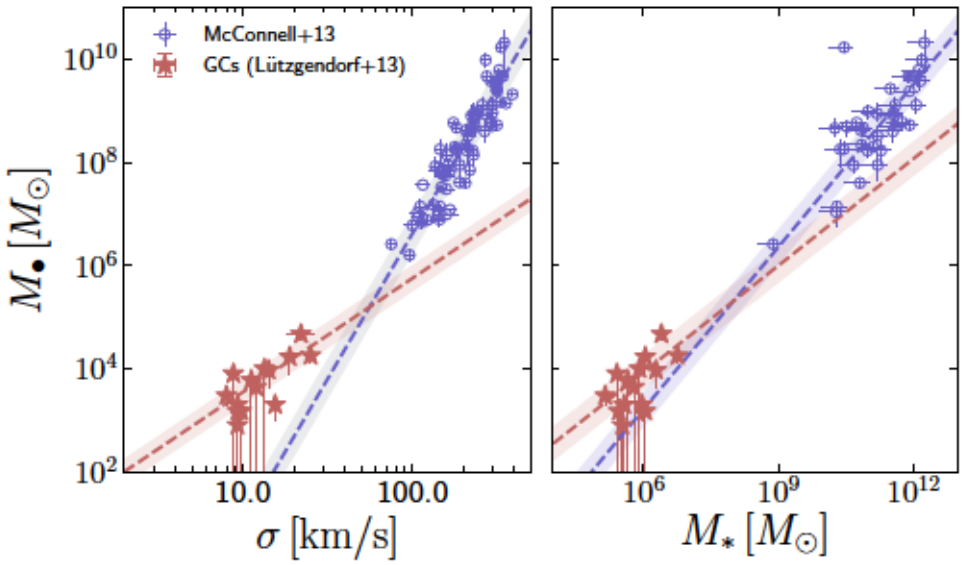

FIGURE 1.1: $M_\bullet - \sigma$ and $M_\bullet - M_*$ scaling relations. This Figure, adapted from Lützgendorf et al. (2013b), show the mass of the central BH for galaxies (McConnell & Ma, 2013) and globular clusters (Lützgendorf et al., 2013b), with respect to their central velocity dispersion (σ, left panel) and stellar mass (M_*, right panel). The dashed lines represent the scaling relation, whereas the shadowed regions show the scatter of each correlation. GCs do not follow the scaling relation for galaxies, the significant mass loss of GCs during their evolution could be responsible for this effect.

stellar dynamics, is significantly smaller ($\lesssim 10\,\mathrm{pc}$) than the region represented by the central velocity dispersion ($\lesssim 1\,\mathrm{kpc}$).

The physical phenomena behind the $M_\bullet - \sigma$ and other scaling relations are still unclear, as it could be a combination of co-evolution (for example, due to AGN feedback) and mergers (e.g., Kormendy & Ho, 2013). Furthermore, the correlation and scatter changes depending on the type of galaxy and the method used to measure the SMBH's mass. Jahnke & Macciò (2011) show that simulations of consecutive mergers of less massive stellar systems with central black holes in the mass range of IMBHs can reproduce the observed scaling relation and scatter, without requiring AGN feedback. Extending the $M_\bullet - \sigma$ and other scaling relations to the range of IMBH masses ($M_\bullet < 10^5\,M_\odot$) could help to further understand the origin of the scaling relations.

The search for IMBHs in dwarf galaxies and globular clusters has pushed forward the lower limits of these scaling relations. Lützgendorf et al. (2013b) used their and literature values of estimated masses for Galactic GCs to analyse the scaling relations' behaviour at lower masses. Figure 1.1 shows $M_\bullet - \sigma$ and $M_\bullet - M_*$ scaling relations for candidate IMBHs in Galactic GCs and SMBHs in nearby galaxies (adapted from Figure 2 of Lützgendorf et al., 2013b). The difference in the slope between GCs and galaxies may indicate that different effects are causing the scaling relations. However, GCs undergo significant mass loss during their evolution. Consequently, their current

mass and velocity dispersion might not represent their initial conditions, which would move the points towards the left of the scaling relations for galaxies.

1.1.4 Connection with Globular Clusters

As mentioned at the beginning of this section, there is scarce evidence for the existence of IMBHs. The accretion signatures by an ultraluminous X-ray source known as ESO 243-49 HLX-1 suggest an IMBH with a lower mass limit of $M_\bullet \sim 500\,M_\odot$ (Farrell et al., 2009). A more recent candidate from the gravitational wave signal, GW190521, puts the resulting merger product at $M_\bullet \sim 140\,M_\odot$. Whereas other studies in extragalactic systems find central BHs in the range of $M_\bullet \sim 10^5\,M_\odot$ (see, Greene et al., 2020), not many fall within the $10^3 - 10^4\,M_\odot$ range. A few recent candidates at the centre of dwarf galaxies with masses of $M_\bullet \sim 10^3\,M_\odot$ have been suggested by Nguyen et al. (2019); Woo et al. (2019).

From the formation scenarios discussed in Section 1.1.2, it is natural to search for IMBHs at the centre of dense stellar systems, such as low-mass NSCs and GCs. Furthermore, if the scaling relations connecting the central BH and the stellar system masses hold at lower stellar system mass, GCs could host IMBHs on the $10^3 - 10^4\,M_\odot$ range. IMBHs born at the centre of young CGs could have sinked along with their host GC to the galaxy centre and become the seed for a SMBH (Ebisuzaki et al., 2001; Portegies Zwart et al., 2006; Mastrobuono-Battisti et al., 2014; Petts & Gualandris, 2017; Askar et al., 2021).

The following Section 1.2 provides a description of GCs and their internal dynamics, and then Section 1.3 covers the many efforts to detect IMBHs in GCs.

1.2 Globular clusters

In the previous section, we have discussed the physical motivations for the existence of IMBHs. These objects might have formed in dense stellar systems such as globular clusters (GCs). Finding IMBHs in GCs could support the proposed formation scenarios of IMBHs, and also provide a better understanding of the growth of SMBHs and their connection with the host galaxy. This Section introduces GCs and their properties, followed by a description of the GCs internal dynamics and evolution. Finally, it discusses the multiple signatures that an IMBH can produce in a GC and previous work to search for IMBHs in them.

FIGURE 1.2: Image of the GC NGC 6121 or Messier 4. Composite image created with opical and infrared filters from the Wide Field Imager in the MPG/ESO 2.2-metre telescope at ESO's La Silla Observatory. Credits: ESO.

1.2.1 What is a globular cluster?

GCs are dense stellar systems with a characteristic spherical shape (and so their name); although, some also show flattening (van den Bergh, 2008). Figure 1.2 shows an image of the globular cluster NGC 6121 (Messier 4). They are commonly found in galaxies and, as a population, GCs can trace the build-up of their host galaxy (Brodie & Strader, 2006). Our Galaxy hosts approximately 150 GCs discovered so far, with new candidates towards the Galactic bulge (Minniti et al., 2017) just recently discovered. GCs are quite old: many of the MW's GCs have ages around $10-12\,\mathrm{Gyrs}$ (VandenBerg et al., 2013), thus representing the relics of early star formation and merging history of the Galaxy.

GCs are composed of hundreds of thousands up to a few million stars, with a half-light radius of $R_\mathrm{h} \sim 3\,\mathrm{pc}$ and masses between $10^4 - 10^6\,M_\odot$. Figure 1.3 shows the distribution of half-light radii R_h in panel (a), metallicities $[Fe/H]$ in panel (b), central density ρ_c in panel (c) and masses $\log(M_\mathrm{GC})$ in panel (d) for Galactic GCs. Given their sizes and masses, GCs have high central densities $\rho_\mathrm{c} \sim 10^4\,M_\odot/\mathrm{pc}^3$. Many of them reach central densities of $\rho_\mathrm{c} \sim 10^5 - 10^6\,M_\odot/\mathrm{pc}^3$, values at which IMBH formation and growth can happen (as discussed in Section 1.1.2). Furthermore, GCs are usually metal-poor with

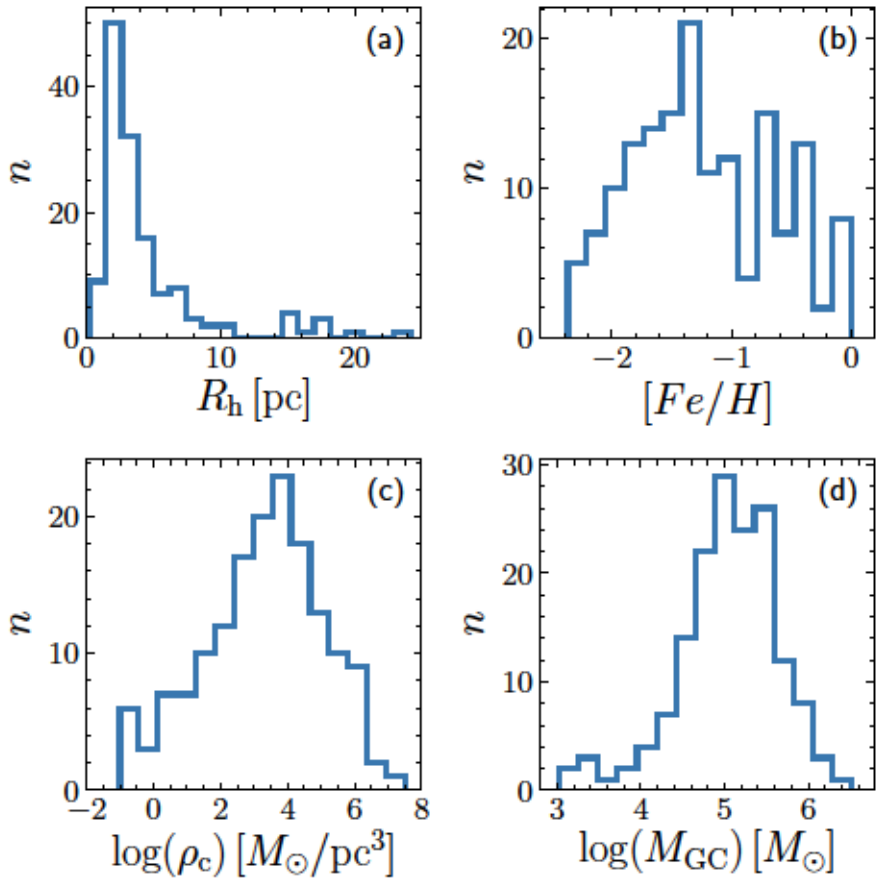

FIGURE 1.3: Main properties of Galactic globular clusters. Panel (a) shows the half-light radius R_h and panel (b) the metallicity $[Fe/H]$ of the clusters, both from Harris (1996) (2010 edition). Panel (c) show the estimated central density $\log(\rho_c)$, while panel (d) the estimated total mass M_{GC} of the Galactic GCs, both properties estimated from N-body models by Baumgardt & Hilker (2018). For all panels, n is the number of GCs per bin.

many Galactic GCs in the range of metallicities where the formation of a very massive star through runaway collisions was possible in the early evolution (see Section 1.1.2), namely $[Fe/H] < -1.7$.

GCs have a characteristically well-defined colour-magnitude diagram[2] (CMD). Figure 1.4 shows the CMD for the globular cluster NGC 6121 (as in Figure 1.2), which follows the main-sequence (MS) until the turn-off point (MSTO) to the subgiant (SG) and red giant branch (RGB). The simplicity of the CMD of GCs is only apparent, as they are more complex than initially thought. Improved photometry showed that GCs have multiple parallel main-sequences (see, e.g., Piotto et al., 2007; Bellini et al., 2010; Milone et al., 2012b) and that some stars in GCs have enhanced element abundances (Carretta et al., 2009). Most old GCs have multiple populations (see Bastian & Lardo, 2018; Gratton et al., 2019, for a review) that show different spatial distributions and

[2]The CMD is also known as the Hertzsprung–Russell (H-R) diagram, which compares the luminosity and the temperature (or spectral type). These diagrams show the different steps of stellar evolution, where a population of stars with the same age is characterized by a single curve called isochrone.

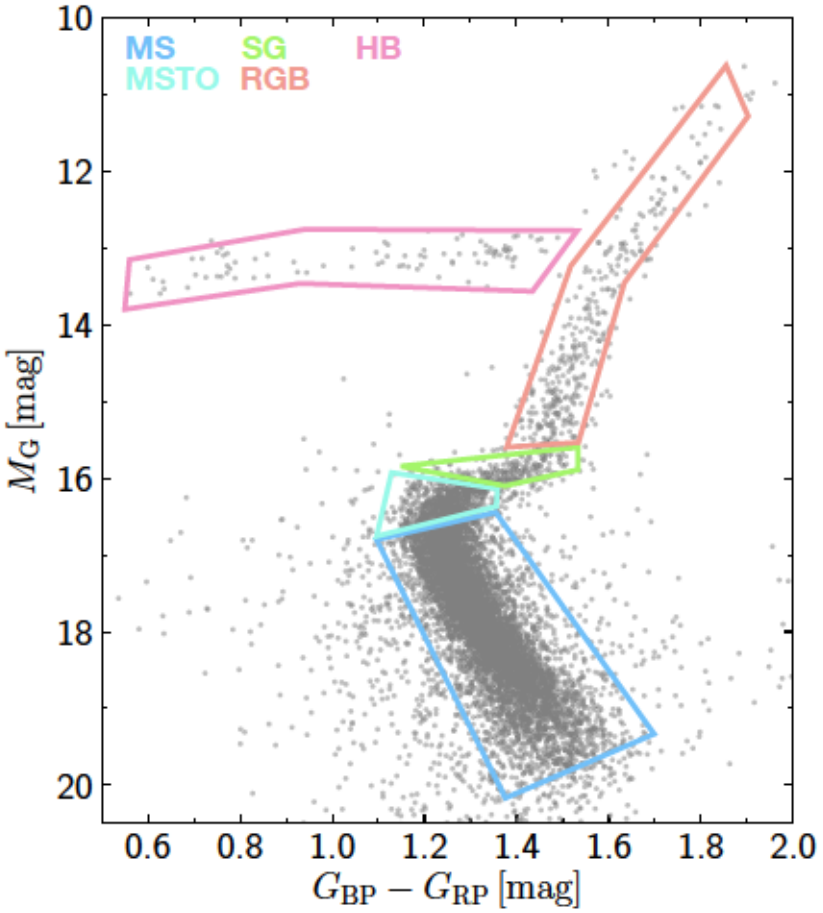

FIGURE 1.4: Color-magnitude diagram for the globular cluster NGC 6121 (Messier 4), using Gaia colors (Gaia Collaboration et al., 2016, 2018). The highligthed region represent different stellar evolutionary stages: main-sequence (MS), main-sequence turn-off point (MSTO), subgiant (SG), red giant branch (RGB) and the horizontal branch (HB).

kinematics (Cordero et al., 2017; Kamann et al., 2020a). However, despite the different element abundances, the multiple populations still share a narrow metallicity spread and only slight age differences (Martocchia et al., 2018; Saracino et al., 2020). The latter means that most stars in a GC were born roughly at the same time, and their position in the CMD can be linked to their mass as more massive stars evolve faster.

GCs have a non-negligible fraction of binary stars $f_{\rm bin} \sim 10\%$ (Sollima et al., 2007; Milone et al., 2012a), with $f_{\rm bin} = n_s/(n_s + n_b)$ where n_s refers to the number of single stars and n_b the number of binary stars. Whereas this amount is low compared to the binary fraction of field stars of $f_{\rm bin} > 50\%$ (Duquennoy & Mayor, 1991), binaries have an essential role in the evolution of GCs. In the CMD, binaries add to the colour scatter along the MS and move in the upward-right direction from the MS, depending on the binary components' mass ratio (Milone et al., 2012a). Alternatively, multi-epoch observations provide another way to identify binaries using their orbital motions and variability in their line-of-sight velocities (Pryor et al., 1988; Cote & Fischer, 1996; Giesers et al., 2019), see also discussion in Section 4.2.2. The presence of blue straggler

stars and millisecond pulsars also provides indirect evidence for binaries in GCs. The binary stellar evolution and (or) dynamical interaction of binaries can produce blue stragglers stars (Mapelli et al., 2006). As it is discussed further in Section 1.2.2 and Chapter 4, binaries have a crucial role in the dynamical evolution of GCs. In particular in the late stages of the GC's dynamical evolution.

GCs also have a significant component of stellar remnants. Deep observations of GCs show the white dwarf sequence (see, e.g., Richer et al., 1997; Monelli et al., 2005; Moehler & Bono, 2008), while the detection of pulsars and millisecond pulsars in GCs show that they also host neutron stars (see, e.g., Anderson et al., 1990; Camilo et al., 2000; Ransom, 2008; Freire, 2013). Furthermore, GCs host not only white dwarf and neutron stars but also stellar-mass BHs. The first detections of X-ray signatures produced by accreting stellar-mass BHs (Maccarone et al., 2007; Strader et al., 2012a) opened the window for many more studies searching for stellar-mass BHs (Miller-Jones et al., 2015; Bahramian et al., 2017). Whereas most candidate stellar-mass BHs in GCs originates from X-ray signatures, another detection method uses kinematic evidence of binary stars where one components is a BH (Giesers et al., 2018, 2019). Both ways identify BHs with a companion star in a binary system; this is not necessarily the case for all BHs in a GC, and the cluster could still retain many more BHs. As discussed in Section 1.1.2, the presence of stellar-mass BHs plays a role in forming IMBHs, particularly for the slow formation channel.

1.2.2 Internal dynamics and evolution of globular clusters

The internal dynamics and dynamical evolution of GCs have been studied thoroughly in the last since the early-1960s (Michie, 1961; King, 1966). The development of numerical simulations have pushed even further the understanding of the dynamical evolution of GCs (Aarseth, 1999). This Section introduces the main elements of the dynamical evolution of GCs based on the descriptions by Heggie & Hut (2003); Binney & Tremaine (2008). Further readings on the topic include Spitzer (1987); Meylan & Heggie (1997).

The description of the internal dynamics of any stellar system depends on how relevant the stellar encounters and interactions are for the overall dynamical evolution of the stellar system. At a first-order, the dynamical state of a stellar system is given by the velocity distribution of stars and the gravitation potential given by the mass of the whole stellar system; stars will follow the orbit defined by the gravitational potential, their position and velocity (or the total energy they have). However, encounters between stars will alter their initial orbital motion, and after many subsequent interactions, stars will eventually "forget" their original orbit.

The diffusive process behind the alteration of a star's orbit by encounters is known as **two-body relaxation**, as it is driven by an accumulation of many interactions between

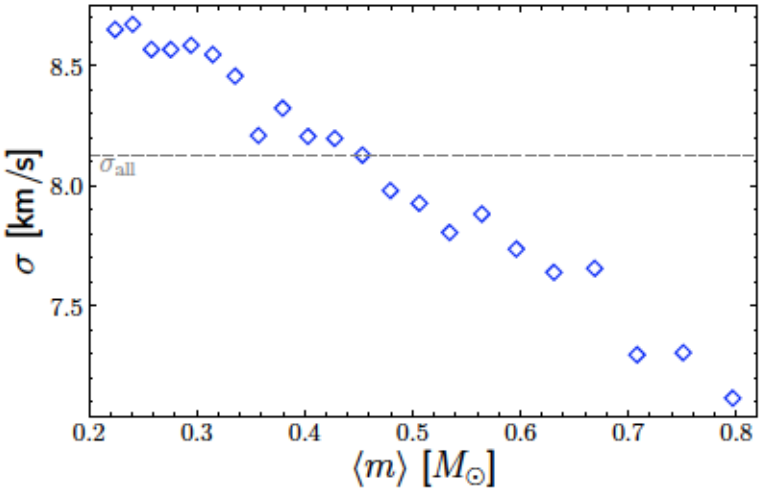

FIGURE 1.5: Velocity dispersion σ for stars with similar mass ranges within the MS, given by their mean mass $\langle m \rangle$, for a 12 Gyr old simulated GC. Due to the cluster's evolution towards (partial) energy equipartition, massive stars transfer kinetic energy to low-mass stars, the higher values of velocity dispersion show the increase in kinetic energy of low-mass stars.

two stars. The **relaxation time** is the required time for the encounters to change the original orbit significantly, and it is approximately given by:

$$t_{\rm relax} \sim \frac{0.1N}{\ln(N)} t_{\rm cross}\,, \tag{1.1}$$

where N is the number of stars in the stellar system, and $t_{\rm cross}$ is the time for a star to cross the stellar system (Binney & Tremaine, 2008). GCs containing $N \sim 10^6$ stars, with velocity dispersions of $\sigma \sim 10$ km/s and sizes in the order of $R_{\rm h} \sim 10$ pc, will have a crossing time around $t_{\rm cross} \sim 1$ Myr and a relaxation time in the order of $t_{\rm relax} \sim 0.8 - 1$ Gyr. For a given stellar system, the relaxation time changes with radius, as the velocity dispersion, sizes and number of stars also change; the usual value used is the relaxation time within the half-mass radius, $t_{\rm rh}$. In the case of the Milky Way's globular clusters, the median relaxation time is $t_{\rm rh} = 1.5$ Gyr (Baumgardt & Hilker, 2018). As the GCs' ages are in the range of $10 - 12$ Gyr (VandenBerg et al., 2013), they had undergone multiple relaxation times, making two-body interactions the dominant driver for their dynamical evolution.

During the two-body interactions, stars interchange kinetic energy evolving towards a state of energy equipartition. The difference in masses of the interacting stars drives the energy transfer, where more massive stars lose kinetic energy and transfer it to lower mass stars Spitzer (1969). GCs do not achieve full energy equipartition during their dynamical evolution; however, even a partial level of energy equipartition has an effect on the internal dynamics of GCs (Trenti & van der Marel, 2013; Bianchini et al., 2016b).

At a local level (i.e., at any given region of a GC), populations of stars with different

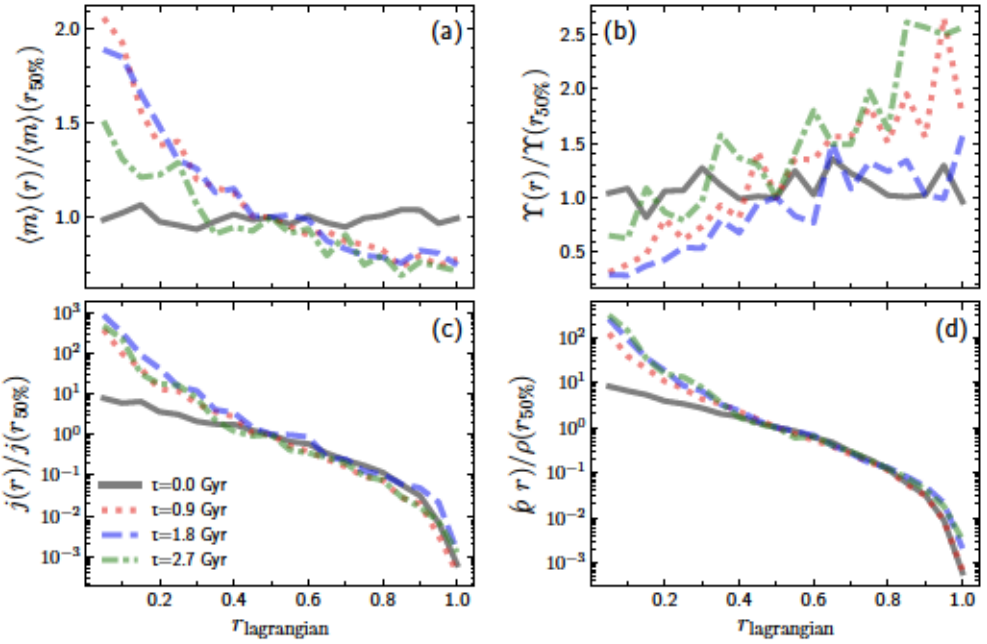

FIGURE 1.6: Mean mass $\langle m \rangle$(r), mass-to-light ratio Υ(r), luminosity density j(r) and mass density ρ(r) of a simulated GC at different evolutionary times. In grey the initial condition at $t = 0$ Gyr is given, in red condition after $t = 0.9$ Gyr, in blue after $t = 1.8$ Gyr and in green after $t = 2.7$ Gyr. Each profile normalized to their respective values at the half-mass radius ($r_{50\%}$) and in function of the Lagrangian radius of the cluster. A consequence of energy equipartition is mass segregation (panel a), where massive stars populate the cluster centre and low mass stars the outer layers. With mass segregation, the mass-to-light ratio also changes (panel b) increasing with radius as low-mass and fainter stars accumulate in the outer layers. Stellar remnants such as white dwarfs, neutron stars and stellar-mass black holes can also increase the mass-to-light ratio at the GC's centre. Panels (c) and (d) show that as the cluster evolves, both the luminosity and mass density form a cusp as the GC's core becomes more dense.

stellar masses will have different velocity dispersions. Figure 1.5 shows the velocity dispersion and average masses for stars along the stellar MS within the GC's half-light radius. As mass increases, the velocity dispersion of each mass population decreases. Whereas Figure 1.5 shows the case for a simulated cluster, observations of faint stars along the main sequence show the same behaviour (Bellini et al., 2014; Heyl et al., 2017).

As massive stars lose kinetic energy, their orbits shrink and sink towards the GC's centre. On the other hand, low mass stars expand their orbits, moving outwards. The consequence of this process is mass segregation, where massive stars accumulate towards the centre and the low mass stars populates the outer layers of the cluster. Panel (a) of Figure 1.6 shows the evolution of the mean mass $\langle m \rangle$ of a simulated cluster with time, tracing the mass segregation as the cluster's centre increases its mean mass, pushing low-mass stars outside. Mass segregation also affects the mass-to-light ratio Υ. Panel (b) of Figure 1.6 shows that as the cluster evolves, the mass-to-light ratio Υ increases with radius as low-mass stars have a larger mass-to-light ratio than massive stars. Although this simulated cluster only had five neutron stars at $t = 2.7$ Gyr, the

presence of massive remnants, in particular stellar-mass black holes, will increase the mass-to-light ratio at the cluster's centre (see discussion in Section 3.4.2). Bianchini et al. (2017) show that it is possible to infer the shape of the mass-to-light profile by knowing the cluster's dynamical age, which can be estimated by either the level of energy equipartition (Bianchini et al., 2016a) or the amount of mass segregation in the GC, in particularly using the distribution of blue-straggler stars (see, e.g. Ferraro et al., 2012; Hypki & Giersz, 2017; Ferraro et al., 2018; Pasquato & Di Cintio, 2020).

Panels (c) and (d) in Figure 1.6 show that the luminosity $j(r)$ and mass density $\rho(r)$ of a GC form a central cusp. As the cluster evolves, the accumulation of massive stars increases the central density of the cluster, while ejecting most low-mass stars from the core. Once the core does not have enough energy to support the gravitational potential, it contracts in a process known as "gravothermal catastrophe" or "core collapse" (Lynden-Bell & Wood, 1968; Spitzer, 1969). The core collapse marks the start of the final stages in the dynamical evolution of a GC, which end with decoupled core and a sparse halo of stars. During the core collapse, as the core density increases, the formation and hardening of binaries provides an additional source of energy to the core, expanding it. The core expands until it cannot support the gravitational push and contracts again. After the initial core collapse, the cluster's core undergoes several cycles of expansions and contractions known as "gravothermal oscillations" (Heggie, 1984; Makino, 1996).

Whereas more massive stars accumulate towards the cluster centre, low-mass stars form a dispersed halo surrounding the core. If the GC is isolated, its final fate is to dissipate as stars become unbound. This process accelerates with the presence of an external tidal field, and GCs can lose a significant fraction of their initial mass during their evolution (see e.g., Heggie, 2001; Heggie & Hut, 2003). Many Milky Way's GCs show tidal tails formed by stars that have been lost due to this dissipation process (Grillmair et al., 1995; Chun et al., 2010; Leon et al., 2000; Odenkirchen et al., 2001, 2003; Jordi & Grebel, 2010; Sollima, 2020), the dynamical modelling of these tidal tails provide an alternative method to study the Milky Way's potential and dark matter content (Küpper et al., 2010; Mastrobuono-Battisti et al., 2012; Bonaca et al., 2019).

Primordial binary stars in GCs play a significant role as a non-renewable source of energy. As mentioned before, the formation and hardening of binaries during core-collapse provide an additional energy source to the core of the GC. Primordial binaries will segregate faster to the cluster's core, as binaries are more massive than single stars on average. As they populate cluster core, encounters between binaries and single stars (or other binary stars) will heat the core by two processes. The first process is the so-called 'hardening': that happens when the binding energy of a binary is larger than the kinetic energy of the surrounding stars; during an interaction with a third star, the binary will transfer energy while becoming more gravitationally bound. On the other hand, if the binding energy is lower than the kinetic energy of the surrounding stars, the binary will transfer energy through the destruction of the initial binary and the

subsequent formation of a new binary. Through these processes, primordial binaries can delay the time of core-collapse and provide energy during the following post-core collapse period until the binary population is depleted (McMillan et al., 1990; Heggie & Aarseth, 1992; Giersz, 2001; Fregeau et al., 2003; Heggie & Hut, 2003; Heggie et al., 2006; Trenti et al., 2007a).

In a similar way to binaries, if the GC retains a significant fraction of stellar-mass BHs, they will also work as a source of energy. As stellar-mass BHs segregate to the cluster centre, they halt core-collapse and quench mass segregation (Mackey et al., 2008; Breen & Heggie, 2013a,b; Sippel & Hurley, 2013; Morscher et al., 2013, 2015; Weatherford et al., 2018). This translate to more extended cores. The presence of an IMBH in the centre of a GC will have a similar effect, halting core collapse and quenching mass segregation with the subsequently extended core. This is a consequence of the higher stellar densities surrounding the IMBH, where the encounters and scattering of stars become more efficient (Baumgardt et al., 2004; Trenti et al., 2007b; Gill et al., 2008a).

1.3 Searching IMBHs in GCs

As mentioned in Section 1.1.4, GCs are good candidates where to search for IMBHs, and as such, many studies have focused on finding signatures of IMBHs within Galactic GCs within the last two decades. However, no clear evidence has been found so far, and the discussion is still as open as ever. This section will introduce the different signatures indicating the presence of an IMBH while discussing the main candidates and the limitations behind the lack of clear evidence.

1.3.1 Signatures of IMBHs

Similarly to supermassive black holes, the two main ways to detect and measure the mass of an IMBH are accretion and dynamical signatures. If gas is accreted into the IMBH, it will heat up and can be observed in either X-ray or radio emission (Pooley & Rappaport, 2006). However, there is no detection of accretion signatures in GCs consistent with an IMBH (Strader et al., 2012b; Tremou et al., 2018), and radio data puts upper limits for IMBH masses in Galactic GCs of $M_\bullet < 1000\,M_\odot$ (Tremou et al., 2018). Whereas the lack of radio signals could indicate that IMBHs are rare or non-existent, IMBHs with masses up to a few hundreds $M_\odot$ are not massive enough to have a radio signature (Tremou et al., 2018).

The second way to detect an IMBH comes from their dynamical interaction with the surrounding stars in the cluster's centre. GCs with a central IMBH will show three main signatures: a shallow cusp in the surface brightness, a rise in velocity dispersion towards the cluster's centre and an extended core (see, Baumgardt et al., 2005; Trenti

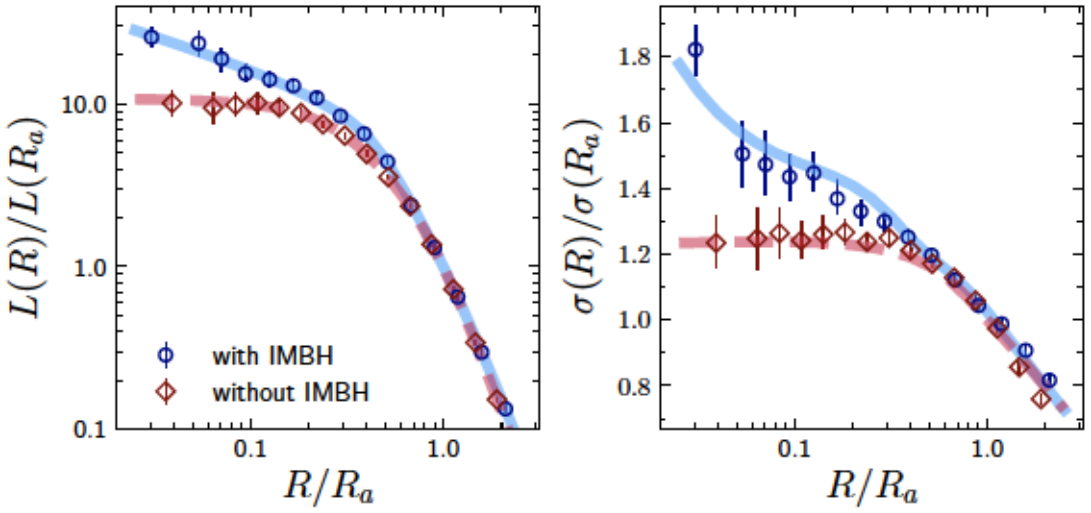

FIGURE 1.7: Surface brightness L and velocity dispersion σ for simulated clusters with and without an IMBH from the MOCCA-Survey I (Askar et al., 2017). Both normalized to the values at the scale radius for the central cusp R_a. The presence of an IMBH (blue circles) will produce a characteristic cusp in both the surface brightness and velocity dispersion. Signatures that contrast the flat profiles of a cluster without an IMBH (red diamonds).

et al., 2007b; Noyola & Baumgardt, 2011). The left panel of Figure 1.7 shows the surface brightness (L) for a simulated cluster with (blue-continuous line) and without and IMBH (red-dashed line). As expected, the simulated GCs hosting an IMBH has a steeper central profile compared to the one without an IMBH. Noyola & Baumgardt (2011) explore a sample of simulated GCs with and without a central IMBH, finding that those hosting an IMBH have a shallow cusp in their surface density, with a logarithmic slope between -0.1 and -0.4 have an IMBH. However, clusters undergoing core collapse might have similar central slopes (Vesperini & Trenti, 2010). As IMBHs can halt mass segregation and the subsequent core collapse (Trenti et al., 2007b; Gill et al., 2008a), it is unlikely for clusters that show an advanced stage or have already undergone core collapse to host any IMBH (Noyola & Baumgardt, 2011).

The right panel of Figure 1.7 shows line-of-sight velocity dispersion (σ) for a cluster with and without an IMBH; the former has a characteristic rise in velocity dispersion towards the centre due to the presence of an IMBH. This rise in velocity dispersion is a consequence of stars following the Keplerian potential of the IMBH. Modelling the velocity dispersion is a valuable method to determine the mass of a central black hole, and many studies searching for a central IMBH in GCs have used this approach to estimate the mass of a possible IMBH. However, no clear kinematic evidence has been found yet, and most cases only find upper limits. Table 1.2 summarises the estimated masses for IMBH candidates in GCs from an extensive list of studies in the last 20 years using kinematic signatures, indicating the type of data used and the alternative possibilities that can explain the observed kinematics. The diversity of kinematic data (line-of-sight

TABLE 1.2: Summary of IMBH studies in the literature. This table compiles the many studies searching IMBHs in Galactic and nearby clusters using kinematic signatures. It includes the GC's name, the type of data used, the estimated mass or upper limit $M_\bullet$, the alternative explanation for cases when no IMBH is claimed and their respective references.

GC Name	Data	$M_\bullet\,[M_\odot]$	alternative	Ref.
G 1	RV	$2.0^{+1.4}_{-0.8} \times 10^4$		1
	RV	no IMBH		2
	RV	$1.8 \pm 0.5 \times 10^4$		3
NGC 104 (47 Tuc)	RV	$< 1.5 \times 10^3$		4
	PMs	No IMBH	stellar-mass BHs	5
NCG 1851	RV	$< 2.0 \times 10^3$		6
NGC 1904 (M 79)	RV	$3.0 \pm 1.0 \times 10^3$		6
NGC 2808	RV	$< 1 \times 10^4$		7
NGC 5139 (ω Cen)	RV	$4.0^{+0.75}_{-1.0} \times 10^4$		8
	PMs	$< 1.8 \times 10^4$		9
	RV	$4.7 \pm 1.0 \times 10^4$		10
	RVs + PMs	no IMBH	anisotropy	11
	RVs + PMs	4.0×10^4		12
	RVs + PMs	no IMBH	stellar-mass BHs	13
	RVs + PMs	no IMBH	stellar-mass BHs	14
NGC 5272 (M 3)	RV	$< 3.0 \times 10^3$		15
NGC 5286	RV	$1.5 \pm 1.0 \times 10^3$		16
NGC 5694	RV	$< 8.0 \times 10^3$		6
NGC 5824	RV	$< 6.0 \times 10^3$		6
NGC 6093	RV	$< 8.0 \times 10^2$		6
NGC 6205 (M 13)	RV	$< 8.6 \times 10^3$		15
NGC 6266 (M 62)	PMs	$< 4.0 \times 10^3$		17
	RV	$2.0 \pm 1.0 \times 10^3$		6
NGC 6341 (M 92)	RV	$< 9.8 \times 10^2$		15
NGC 6388	RV	$1.7 \pm 9.0 \times 10^4$		18
	RV	$< 2.0 \times 10^3$		19
	RV	$2.8 \pm 0.4 \times 10^4$		20
NGC 6397	RV	$6.0 \pm 2.0 \times 10^2$		21
	RVs + PMs	no IMBH	stellar-mass BHs	22
NGC 7078 (M 15)	RV	$3.3 \pm 2.2 \times 10^3$		23
	PMs	no IMBH	stellar remnants	24
	RV	no IMBH	stellar remnants	25
	RVs + PMs	no IMBH	extended dark mass	26

References: (1) Gebhardt et al. (2002); (2) Baumgardt et al. (2003); (3) Gebhardt et al. (2005); (4) McLaughlin et al. (2006); (5) Mann et al. (2019); (6) Lützgendorf et al. (2013a); (7) Lützgendorf et al. (2012); (8) Noyola et al. (2008); (9) van der Marel & Anderson (2010); (10) Noyola et al. (2010); (11) Zocchi et al. (2017); (12) Baumgardt (2017); (13) Baumgardt et al. (2019b); (14) Zocchi et al. (2019); (15) Kamann et al. (2014); (16) Feldmeier et al. (2013); (17) McNamara et al. (2012); (18) Lützgendorf et al. (2011); (19) Lanzoni et al. (2013); (20) Lützgendorf et al. (2015); (21) Kamann et al. (2016); (22) Vitral & Mamon (2021); (23) Gerssen et al. (2002); (24) McNamara et al. (2003); (25) Baumgardt et al. (2003); (26) den Brok et al. (2014).

radial velocities or proper motions) and the variety of modelling methods (dynamical models, distribution function models or numerical simulations) further complicate the picture.

The rise in velocity dispersion expected from an IMBH might also be a consequence of other dynamical effects. For example, a bias towards radial orbits in the velocity distribution of stars, can increase the observed velocity dispersion towards the centre and reduce the estimated mass of the possible IMBH (van der Marel & Anderson, 2010; Zocchi et al., 2017). Similarly, an extended dark mass due to the presence of stellar-mass black holes could produce a similar signature in the velocity dispersion as the one from an IMBH (Zocchi et al., 2019; Baumgardt et al., 2019b; Mann et al., 2019; Vitral & Mamon, 2021), in particular for IMBHs with a low mass fraction compared to the cluster mass. Chapter 3 focuses on the aforementioned dynamical effects and their consequences on the detection of a central IMBH.

1.3.2 Observational limitations for the detection of an IMBH

The prominence and extent of the cusp in velocity dispersion depend mainly on the IMBH's mass fraction with respect to the GC's mass and its radius of influence. The radius of influence ($r_{\rm inf}$) is the radius where the circular velocity due to the IMBH's Keplerian potential is equal to the velocity dispersion:

$$r_{\rm inf} = \frac{GM_\bullet}{\sigma(r_{\rm inf})}\,, \tag{1.2}$$

where $M_\bullet$ is the mass of the IMBH and σ is the velocity dispersion of the stars, which in turn depends in the velocity distribution of stars and the mass of the GCs (Binney & Tremaine, 2008). The main observational limitation for the detection of an IMBH is the small sizes of the radius of influence. For example, mass estimations on the possible IMBH at the centre of NGC 5139 (ω Cen), in the order of $M_\bullet \sim 4\times10^4\,M_\odot$, define a projected radius of influence of $R_{\rm inf} \sim 5''$ (or 0.1 pc) at a distance of $d = 4.8$ kpc from the Sun (Noyola et al., 2010), which is considerably small compared to its core radius of $R_{\rm c} = 2.37'$ (3.4 pc) and half-light radius of and $R_{\rm h} = 5'$ (7.0 pc) (Harris, 1996, 2010 edition).

The determination of the kinematic centre of a GC is essential for the identification of an IMBH. In the case of NGC 5139, van der Marel & Anderson (2010) pointed out that with a different kinematic centre, 12″ from the previously used by Noyola et al. (2008), the previous estimated mass for the central IMBH of $M_\bullet = 4.0^{+0.75}_{-1.0}\times10^4\,M_\odot$ (Noyola et al., 2008) changes to an upper-limit of $M_\bullet < 1.8\times10^4\,M_\odot$ (van der Marel & Anderson, 2010). However, further analysis by Noyola et al. (2010) show that the estimated masses do not change significantly for both centres. The kinematic data used by both studies could hide a possible explanation for this discrepancy. Noyola et al. (2008, 2010) use

line-of-sight radial velocities, whereas van der Marel & Anderson (2010) use proper motions. Chapter 3 explores the different constraints on the dynamical modelling of a GC with a central IMBH. As discussed later in Chapter 4, the presence of binary stars can increase the observed velocity dispersion of line-of-sight velocities; this is not the case for proper motions that remain mainly unaffected. The presence of binaries, therefore, could explain the difference between line-of-sight and proper motion velocity dispersion in NGC 5139.

Given the high stellar density at the centre of GCs, the crowding of stars limits the observations around the cluster's centre. A single bright star could dominate the observed kinematics of integrated spectra or line-of-sight velocities (de Vita et al., 2017). An interesting example is the case of NGC 6388, where different observations put the central velocity dispersion of the cluster at $\sigma = 25\,\mathrm{km/s}$ (Lützgendorf et al., 2011) or $\sigma = 13\,\mathrm{km/s}$ (Lanzoni et al., 2013), which implies the presence of an IMBH of $M_\bullet = 1.7 \times 10^4\,M_\odot$ or an upper limit of $M_\bullet < 2.0 \times 10^3\,M_\odot$, respectively. Follow up analysis by Lützgendorf et al. (2015), shows that the lower velocity dispersion measured by Lanzoni et al. (2013) could have been dominated by scattered light and represent the mean velocity field. The development of new analysing techniques improved the management of crowded areas in GCs (see, Kamann et al., 2014, 2016), and the enhanced resolving power of the next generation of instruments at E-ELT and JWST will further improve the observation of crowded areas.

The presence of binaries might also be relevant for the detection of IMBHs. As discussed thoroughly in Chapter 4, binaries can increase the observed line-of-sight velocity dispersion, particularly towards the cluster centre. This increase results in overestimations for the IMBH mass and larger upper limits when an IMBH is not detected (see discussion in Section 5.4).

1.4 Outline of the thesis

This thesis will follow up in the vast diversity of IMBH searches in GCs, pointing to areas that require improvement and seeking alternative indications for the presence of an IMBH. The research work in this thesis also aims to motivate the connection between dynamical modelling and simulations as a powerful way to improve the dynamical modelling of GCs and better understand their observed properties.

Chapter 2 introduces the main methods used in this thesis: dynamical modelling and simulations. For the dynamical modelling, the Chapter briefly builds into basic dynamical knowledge to describe some of the techniques used in the literature, with a particular interest in the Jeans Equations, providing a simple example of how to model a simple globular cluster. Concerning simulations, this Chapter introduces the importance of numerical simulations to understand the evolution of GCs and the development of such

simulations. It compares the direct N-body and the Monte Carlo methods, focusing on the latter one as all simulations used in this thesis come from Monte Carlo models.

Chapter 3 discuss the dynamical limitations of the Jean Equations modellings. This Chapter follows the published work by Aros et al. (2020). We use Jean Equations in five simulated GCs with and without an IMBH to test the reliability of the dynamical modelling. To do so we also consider almost perfect data and do not include any of the observational limitation mentioned in section 1.3.2. Furthermore, we do not consider kinematic errors in the data and only account for the effects of stochasticity. This allows us to only focus on the limitation of the dynamical models. Whereas we can easily find the mass of a high-mass IMBH with a mass fraction with respect to the cluster mass of $M_\bullet/M_* = 4.0\%$, the same cannot be said of a low-mass IMBH ($M_\bullet/M_* = 0.3\%$) for which only upper limits are found. Cases without an IMBH also show large upper limits that are still consistent with IMBHs of $M_\bullet \sim 10^3\,M_\odot$. We suggest that the main effect behind this is the lack of constraints on the mass profile of the clusters, in particular on the one with a large fraction of stellar-mass black holes.

Chapter 4 analyses the effect of undetected binaries in the kinematic data of GCs. The results of this chapter have been submitted for publication. We find that the presence of binaries increases the observed line-of-sight velocity dispersion up to $\sim 60\%$ of the actual velocity dispersion (in the most extreme case). However, in simulated GCs with a central IMBH, the fraction of retained binaries decreases significantly. On average, they have 67% fewer binaries within their core radius than clusters without an IMBH. We use these results to suggest that the retained binary fraction will help identify GCs with a central IMBH.

In Chapter 5, we further analyse the results presented in Chapters 3 and 4. The Chapter describes work in progress at the time of this thesis. We extend the dynamical modelling to a much larger sample and place them in the context of the scaling relations introduced in Section 1.1.3. We find that GCs hosting IMBH with a low mass fraction $M_\bullet/M_* < 2.0\%$ are harder to identify and our models can only account for upper limits. In the $M_\bullet - \sigma$ relation, we find that GCs with a significant retained fraction of stellar-mass black holes have similar behaviour to clusters with an IMBH. Finally, we discuss the effects of the binaries in the estimated masses of IMBHs and their effect on the $M_\bullet - \sigma$ relation.

Finally, Chapter 6 summarises the main results from Chapters 3, 4 and 5, putting them in the broad context presented in the introduction. Chapter 6 also includes follow-up research that could further improve the results presented in this thesis.

Chapter 2

Methods: Stellar dynamics and numerical simulations

This thesis explores the limitations of dynamical models when measuring the mass of a central intermediate-mass black hole (IMBH) in globular clusters (GCs). To do so, we apply dynamical models to mock data obtained from numerical simulations of GCs. This Chapter discusses the two main methods used in an introductory and broader manner. Chapters 3, 4 and 5 contain their own "methods" sections that focus on their respective specific objectives.

2.1 Stellar dynamics

As discussed in Section 1.3.1, if an IMBH is present in the centre of a GC, the surrounding stars will follow the gravitational potential of the IMBH and show a characteristic rise in the observed velocity dispersion. Through this kinematic signature, one is able to infer the possible mass of the central IMBH. To do so, we need to model the GC's dynamical state. This section provides a general overview of the dynamical models used throughout the thesis; for further details, refer to Binney & Tremaine (2008).

There are two regimes in which we can model the dynamics of a stellar system: collisional and collisionless. The orbit of a star will follow the overall potential of the stellar system. However, as mentioned in Section 1.2.2, encounters between stars can perturb the initial orbit of the star. If many encounters follow, the star will eventually "forget" its initial orbit due to the gravitational potential. If the encounters dominate the dynamics of the system, then the stellar system is **collisional**. On the other hand, if the encounters are not relevant, the stellar system is **collisionless**. We can assume that the stellar system remains collisionless if the dynamical time scales that we are modelling are significantly smaller than the relaxation time (see Section 1.2.2). If, however, the time scales are

longer than the relaxation time, then we must consider the diffusive effects of the stellar encounters.

Stellar encounters and the two-body relaxation process dominate the dynamical evolution of GCs (see Section 1.2.2). If we want to follow the overall dynamical evolution of GCs then we should follow the collisional dynamics regime. However, here we are interested primarly in the *instantaneous* dynamical state of the GCs, given by their observed stellar distribution and kinematics. In this case, we can assume that the collisionless dynamics regime provides a sufficient representation of the current dynamical state, while at the same time allowing for significant computational simplifications.

Whereas some of the concepts presented in the following apply both dynamical regimes, this introductory description is provided assuming the system is indeed collisionless.

2.1.1 Basic concepts

The motion of stars follows the gravitational interaction due to a single mass or a mass distribution through the well known gravitational force. A more straightforward representation of this mutual interaction comes from considering the **gravitational potential** Φ, in which case stars move following:

$$\frac{d^2\mathbf{x}}{dt^2} = -\nabla\Phi(\mathbf{x})\,. \tag{2.1}$$

The gravitational potential will depend on the mass distribution acting on the star. It can be due to a point-like mass, in which case the gravitational potential has the form:

$$\Phi(r) = -\frac{GM}{r}\,, \tag{2.2}$$

where G is the gravitational constant, M is the point-like mass, and r is the distance between the point-like mass and the star; this is the so-called Kepler potential. On the other hand, if we have an extended mass distribution as is the case for any stellar system, the Poisson equation gives us the gravitational potential:

$$\nabla^2\Phi(\mathbf{x}) = 4\pi G\rho(\mathbf{x})\,, \tag{2.3}$$

where $\rho(\mathbf{x})$ is the mass density of the stellar system.

The path which a star follows, given the gravitational potential, is the **stellar orbit**. Periodic solutions of Equation 2.1 are known as bound orbits and for spherical potentials they will resemble an elliptical shape that can be closed as in the case of the Keplerian potential or open for most other potentials. The eccentricity of the orbit indicates how elongated the orbit is. Section 2.2.3 discusses the Keplerian orbit case, particularly when characterizing binary stars.

The different positions and velocities that any given star has during its orbital motion form the 6-dimensional phase space containing the position and velocity $(\mathbf{x}, \mathbf{v})$ of the star. During the orbital motion, there are functions of the phase space variables that stay constant with time: the **integrals of motion**. The dynamical models used throughout this thesis follow spherical potentials, these potentials have only two integrals of motion: the Hamiltonian $H(\mathbf{x}, \mathbf{v}) = \frac{1}{2}\mathrm{v}^2 + \Phi(\mathbf{x})$, which is linked to the energy, and the angular momentum $\mathbf{L} = \mathbf{r} \times \mathbf{v}$.

The **distribution function** $f(\mathbf{x}, \mathbf{v})$ (DF) provides the probability of finding any given star in the phase space of position and velocity, which allows us to describe the dynamical state of any stellar system. Whereas the DF is not directly observable, the different velocity moments of the DF can provide us with the observable properties of the stellar system.

The zero-order velocity moment provides the probability of a star to be at a certain position $\mathbf{x}$, $\nu(\mathbf{x})$:

$$\nu(\mathbf{x}) = \int f(\mathbf{x}, \mathbf{v}) d\mathbf{v}\,. \tag{2.4}$$

Whereas this quantity cannot be directly observed, it is related to different observables. For a system with N stars, the **number density** is given by $n(\mathbf{x}) = N\nu(\mathbf{x})$. Furthermore, if all stars have the same mass and luminosity, we can define the **mass density** $\rho(\mathbf{x}) = M_{\rm tot}\nu(\mathbf{x})$ and the **luminosity density** $j(\mathbf{x}) = L_{\rm tot}\nu(\mathbf{x})$, where $M_{\rm tot}$ and $L_{\rm tot}$ are the total mass and luminosity of the stellar system. In practice, as stars will have different masses and luminosities, the observed luminosity and mass densities (if the latter is available) will only provide an approximation to $\nu(\mathbf{x})$.

The first velocity moment is given by :

$$\langle \mathrm{v} \rangle(\mathbf{x}) = \int \mathrm{v} f(\mathbf{x}, \mathbf{v}) d\mathbf{v}\,, \tag{2.5}$$

and provides the **mean velocity** of the stellar system. The second velocity moment:

$$\langle \mathrm{v}^2 \rangle(\mathbf{x}) = \int \mathrm{v}^2 f(\mathbf{x}, \mathbf{v}) d\mathbf{v}\,, \tag{2.6}$$

is also known as the mean-squared velocity and relates with the root-mean-squared velocity as $\mathrm{v}_{\rm rms} = \sqrt{\langle \mathrm{v}^2 \rangle}$. A more commonly used observable is the **velocity dispersion** σ, which is given by:

$$\sigma^2 = \langle \mathrm{v}^2 \rangle - \langle \mathrm{v} \rangle^2\,. \tag{2.7}$$

In general, a stellar system will have a **velocity dispersion tensor** that collects the different velocity components for each coordinate σ_i^2 and the cross-terms between coordinates $\sigma_{i,j}^2$. The ratio between the diagonal elements of the velocity dispersion tensor is known as the **velocity anisotropy** of the stellar system. For example, in a spherical

system with coordinates (r, θ, ϕ), the velocity anisotropy β is given by:

$$\beta = 1 - \frac{\sigma_\theta^2 + \sigma_\phi^2}{2\sigma_r^2} \tag{2.8}$$

Where σ_r^2, σ_θ^2 and σ_ϕ^2 are the diagonal components of the velocity dispersion tensor. For $\beta = 0$, the stellar system is isotropic, which means $\sigma_r^2 = \sigma_\theta^2 = \sigma_\phi^2$. If $\beta > 0$, then the stellar system is radially anisotropic, which means that stellar orbits will be preferentially radial (i.e. the orbits will be more eccentric). On the other hand, if $\beta < 0$ the stellar system is tangentially biased, and most stars follow less eccentric or circular orbits.

A stellar system that is collisionless and is in dynamical equilibrium will follow the **collisionless Boltzmann equation**:

$$\frac{\partial f}{\partial t} + \mathbf{v} \cdot \frac{\partial f}{\partial \mathbf{x}} - \frac{\partial \Phi}{\partial \mathbf{x}} \cdot \frac{\partial f}{\partial \mathbf{v}} = 0\,, \tag{2.9}$$

which describes the conservation of the probability for finding a star at a given position in the phase space $(\mathbf{x}, \mathbf{v})$. In the **steady-state** case, the DF does not implicitly depend on time and $\partial f / \partial t = 0$.

The Jeans theorem (Jeans, 1915) indicates that steady-state DFs, which are functions solely of integral of motions, are solutions to the collisionless Boltzmann equation. For spherical systems, we can build isotropic DFs that are functions of the energy through the Hamiltonian $f(H)$ or anisotropic DFs that also depend on the angular momentum $f(H, \mathbf{L})$.

2.1.2 Modelling approaches

As we mentioned in Section 2.1.1, the DF defines the dynamic state of a stellar system; therefore, it is only natural to find its underlying DF. One of the simplest DFs for GC-like stellar systems is the Plummer model (Plummer, 1911), which is frequently used as an approximated representation of the initial state of a cluster in numerical simulations. This choice is partly due to their straightforward mathematical form. A different family of DFs models, known as lowered isothermal models, allows for lower stellar densities at larger radius making them finite, as is the case for GCs. Furthermore, the velocity distribution of the lowered isothermal models resembles a Maxwellian velocity distribution, which is expected for relaxed stellar systems such as GCs. The King model (King, 1966) is one of the most well-known lowered isothermal models and provides a good fit to the surface luminosities of GCs, particularly for more relaxed GCs (Zocchi et al., 2012). Whereas both the Plummer and King models have isotropic DFs, the Michie models (Michie, 1963) have a DF of the form $f(H, \mathbf{L})$ that allows for

velocity anisotropy. Further development of DF models have focussed on the inclusion of multi-mass components (Da Costa & Freeman, 1976; Gieles & Zocchi, 2015; Zocchi et al., 2016; Peuten et al., 2017), the effects of mass segregation and dissolution (Claydon et al., 2019; Gomez-Leyton & Velazquez, 2019) and the internal rotation of GCs (Varri & Bertin, 2012; Bianchini et al., 2013).

Finding the underlying DF of a given stellar system is not straightforward, and it is limited to cases where the appropriate family of functions is known, which is the case of the lowered isothermal models and GCs.

An alternative is to bypass the DF and focus on its velocity moments. The Jeans equations (Jeans, 1922) allow us to model the observed kinematics of a stellar system without relying on the DF and, in the process, to estimate the mass distribution of the stellar system. The Jeans equations have been highly successful to model a variety of stellar systems from GCs to galaxies. Particularly for GCs, many of the studies searching for IMBHs used the Jeans equations (see Section 3.1). The dynamical models used thorough this thesis follow the Jeans equations. Further details on the implementation of the Jeans equation follow in Sections 2.1.3 and 3.2.3. Although their success in modelling the stellar system dynamics, the Jeans equations have two main caveats:

(a) They act solely on the DF's velocity moments and the gravitational potential, and we do not know the DF behind them. Therefore, it is not trivial to prove that the model follows a physical DF.

(b) As they are not closed, further assumptions, such as the velocity anisotropy of stellar systems, are necessary to solve them.

A possible way to overcome the main limitations and assumptions of the Jeans equation models is to build orbit based models. These models follow the so-called Schwarzschild's method (Schwarzschild, 1979) in which bundles of stellar orbits, with different integrals of motion, are evolved under a given potential. The combination of orbits that better represents the observed kinematics of the stellar system constrains the mass distribution of the stellar system and its underlying DF. Orbit based models do not need any assumption for the velocity anisotropy as this is a byproduct of the sampled orbital library. Some of the applications of orbit based models to GCs include the works by Gebhardt et al. (2005); van de Ven et al. (2006); van den Bosch et al. (2006); Noyola et al. (2008).

2.1.3 The Jeans equations

In this thesis, we use dynamical models based on the Jeans equations, which allow us to model the velocity moments rather than the DF directly. This section will briefly describe how to measure the mass of central IMBH through the Jeans equations by

applying the method to mock data sampled from a Plummer model with a central IMBH.

The Jeans equation for a steady-state spherically symmetric stellar system is given by:

$$\frac{d}{dr}\left(\nu(r)\langle \mathrm{v}_r^2\rangle\right) + \nu(r)\left(\frac{d\Phi}{dr} + \frac{2\langle \mathrm{v}_r^2\rangle - \langle \mathrm{v}_\phi^2\rangle - \langle \mathrm{v}_\theta^2\rangle}{r}\right) = 0\,, \tag{2.10}$$

where $\Phi(r)$ is the gravitational potential, $\nu(r)$ is the zeroth order velocity moment given by Equation 2.4, and $\langle \mathrm{v}_r^2\rangle$, $\langle \mathrm{v}_\theta^2\rangle$,and $\langle \mathrm{v}_\phi^2\rangle$ are the second velocity moments. For a given $\nu(r)$ and $\Phi(r)$ we can solve the Jeans equation to find the second velocity moments. However, as we only have one equation for three unknowns, the Jeans equation requires additional assumptions on the velocity anisotropy of the stellar system to solve it. In this case, for simplicity, we assume that the underlying DF is isotropic and of the form $f(H)$. In Section 3.2.3 we will deal with the anisotropic case. Under this assumption, the Jeans equation simplifies to:

$$\frac{d}{dr}\left(\nu(r)\langle \mathrm{v}_r^2\rangle\right) + \nu(r)\frac{d\Phi}{dr} = 0\,, \tag{2.11}$$

and the second velocity moment is:

$$\langle \mathrm{v}_r^2\rangle = \frac{1}{\nu(r)}\int_r^\infty \nu(r')\frac{d\Phi}{dr'}dr'\,. \tag{2.12}$$

In practice, we use observable stellar tracers such as the number density $n(r)$ or the luminosity density $j(r)$ instead of $\nu(r)$.

The first step is, of course, to define which type of data we need. In general, for any stellar system besides our Galaxy we only have the positions of the stars in the sky and the observed velocities which can be radial velocities along the line-of-sight (i.e. spectroscopic data) or proper motions, which are the movement of stars in the plane of the sky (i.e astrometric data). Note that for stellar systems that are not resolved due to their distance, we will only have integrated spectroscopic data. As we are missing one positional coordinate, we can only compare the observed kinematics with a weighted average of the second velocity moment along the line of sight, which in our simple case is given by:

$$\langle \mathrm{v}_{\mathrm{los}}^2\rangle(R) = \frac{1}{N(R)}\int_R^\infty \frac{n(r)dr}{\sqrt{r^2-R^2}}\langle \mathrm{v}_r^2\rangle\,. \tag{2.13}$$

As we are working under the assumption of spherical models, the mean velocities are all zero. Furthermore, we can assume that the observed velocity dispersion is a good representation of the second velocity moment, so that $\sigma_{\mathrm{los}} = \langle \mathrm{v}_{\mathrm{los}}^2\rangle^{1/2}$.

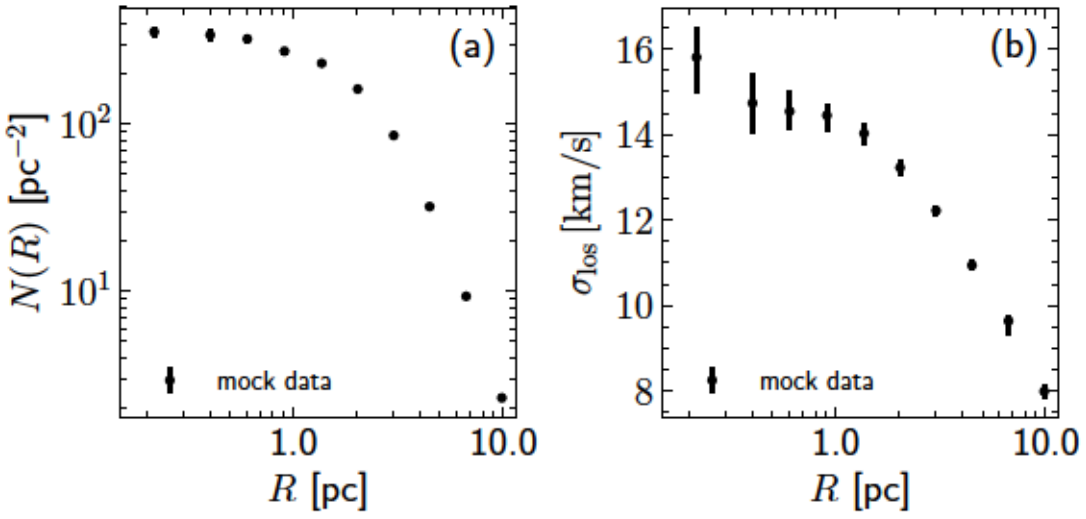

FIGURE 2.1: Surface number density (a) and velocity dispersion (b) for mock data sampled form a Plummer model with $M_{tot} = 10^6\,M_\odot$ and an IMBH of $M_\bullet = 10^4\,M_\odot$.

For this introductory example, we will use mock data sampled from a Plummer model[1] with a central IMBH and a mass density profile that is given by:

$$\rho(r) = \rho_0 \frac{1}{r^{0.1}} \frac{1}{(1+(r/a)^2)^{5/2}}\,, \tag{2.14}$$

with a central density $\rho_0 = 143.2\,M_\odot \mathrm{pc}^{-3}$ of and scale radius $a = 3.13\,\mathrm{pc}$. The total mass of the mock stellar system is $M_* = 10^6\,M_\odot$, and the IMBH corresponds to 1% of the total mass (i.e. $M_\bullet = 10^4\,M_\odot$). Figure 2.1 shows the surface number density $N(R)$ and line-of-sight velocity dispersion σ_{los} for the mock data. These two are the main ingredients required to model and estimate the mass of the central IMBH.

The text step is to deproject the tracer density. In this case, we use the number density, whereas in Chapter 3 and 5, we use the surface luminosity. We deproject the number density using the following formula:

$$n(r) = \frac{-1}{\pi} \int_r^\infty \frac{dR}{\sqrt{R^2 - r^2}} \frac{dN}{dR}\,, \tag{2.15}$$

which is the solution for the Abel integral equation. Figure 2.2 shows the initial surface number density (solid line) and the resulting 3D number density (dashed line).

Once we know the tracer density, the next ingredient for finding the second velocity moment is the gravitational potential. For spherically symmetric potentials, we can find that

$$d\Phi/dr = \frac{GM(r)}{r^2}\,. \tag{2.16}$$

[1]The mock data is part of the models developed by Eugene Vasiliev for the 5th Gaia Challenge and are available on `http://astrowiki.ph.surrey.ac.uk/dokuwiki/doku.php?id=gc5_mocks`

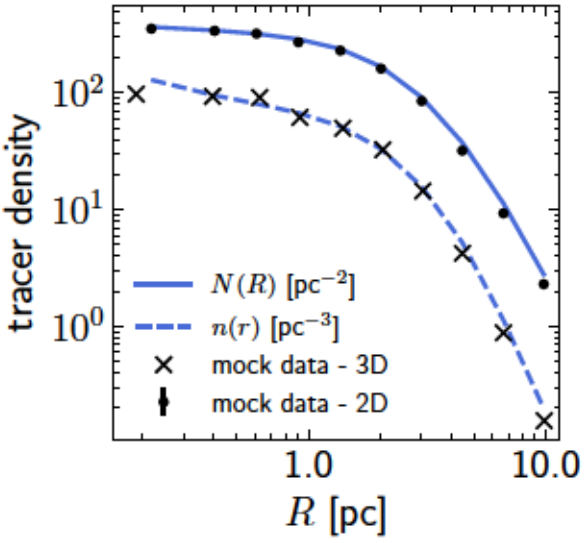

FIGURE 2.2: Tracer densities for the mock data. We deproject the observed surface number density $N(R)$ (solid lines) to find the 3D number density $n(r)$ (dashed lines). We see that the deprojected number density is a good representation of the 3D number density directly measured form the mock data (black crosses).

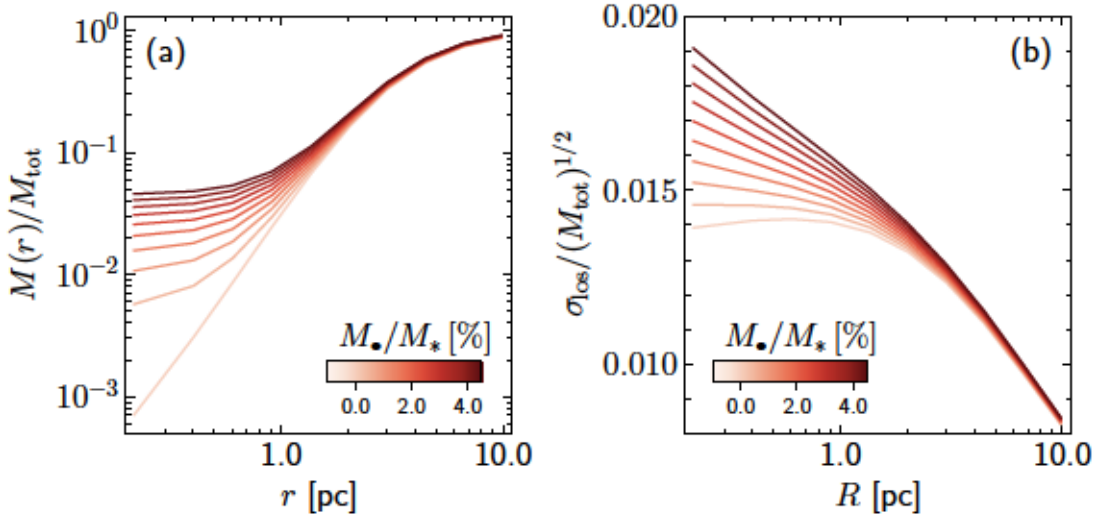

FIGURE 2.3: Mass and velocity dispersion models for different central IMBHs. As the mass of the central IMBH increases, we see that it rapidly dominates the stellar system mass in the centre (panel a). In the same way, as the IMBH mass increases, the central cusp in velocity dispersion becomes more clear (panel b). This feature allows us to constrain the mass of the central IMBH with the observed velocity dispersion.

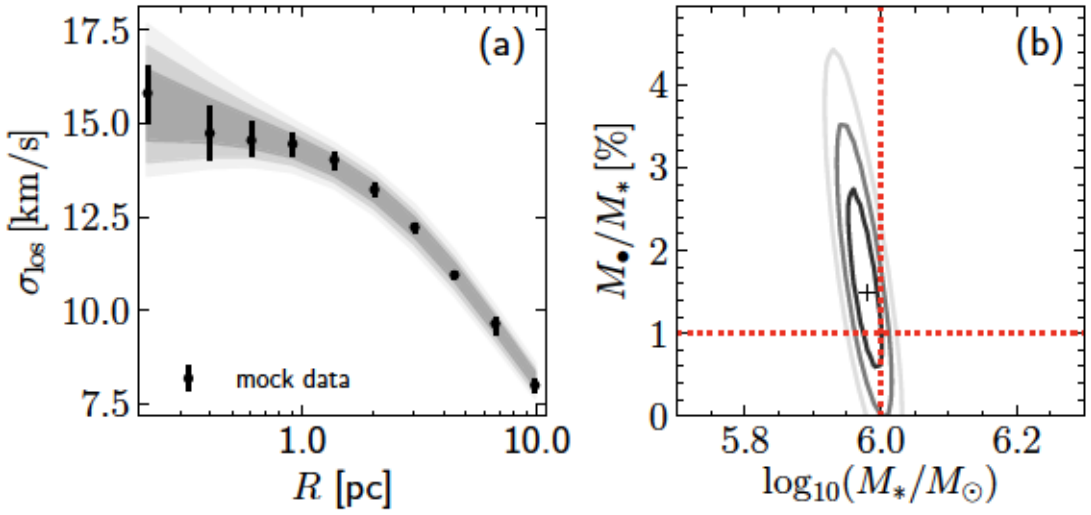

FIGURE 2.4: Results of the χ^2 fit. Given the models in Figure 2.3, we can compare to the data to find the best fit model. Panel (a) shows the observed velocity dispersion and the regions defined by the 68%, 95% and 99.7% confidence regions. Panel (b) shows the resulting best-fit (cross) and confidence regions for the fit, along with the known values (dotted red lines). The expected values are consistent within the 1sigma confidence region.

Therefore, we can use the cumulative mass profile instead of Φ. We build mass profiles of the form:

$$M(r) = M_\bullet + M_*(r)\,, \tag{2.17}$$

where $M_*(r)$ is the mass of the stellar component and is given by:

$$M_*(r) = 4\pi \int_0^r \rho(r') r'^2 dr'\,. \tag{2.18}$$

In practice, we can add as many mass components as we need. In this case, we will assume that the mass density is proportional to the number density and use the total mass as a scalling factor:

$$\rho(r) = M_{\rm tot} \frac{n(r)}{n_{\rm tot}}\,. \tag{2.19}$$

In Chapters 3 and 5 we use the mass-to-light ratio instead to convert from the tracer luminosity density to the mass density. Panel (a) of Figure 2.3 shows the mass profiles for IMBHs with different mass fractions.

For the mass model, we can now obtain the second velocity moment using Equation 2.12 and then use Equation 2.13 to find a comparable value to the observations. Panel (b) of Figure 2.3 shows the line-of-sight velocity dispersion for IMBHs with different mass fractions, from 0% up to 4%. As the mass of the central IMBH increases, the central rise in velocity dispersion becomes steeper. By using these dynamic models, we can build velocity dispersion profiles that can match the effect of an IMBH, as discusses in section 1.3.1 (see also Figure 1.7).

The last step is to compare the models with observations. In this case, we minimize the residuals by calculating the χ^2 for each model given by:

$$\chi^2 = \sum \frac{\left(\sigma_{\rm los} - \langle \mathrm{v}_{\rm los} \rangle^{1/2}\right)^2}{\left(\delta\sigma_{\rm los}\right)^2}, \tag{2.20}$$

where $\sigma_{\rm los}$ is the observed velocity dispersion, $\delta\sigma_{\rm los}$ is the observational error and $\langle \mathrm{v}_{\rm los} \rangle$ is the second velocity moment given by Equation 2.13. Alternatively, we can use the velocities of individual stars in a discrete manner and calculate the likelihood of each model. Figure 2.4 shows the results of the fit, where the grey areas and contours represent the 1,2 and 3-sigma levels of the fit. We find that our estimation of the masses is consistent with the real values within errors.

In Chapters 3 and 5, we follow a similar approach to estimate the masses of IMBH in simulated data.

2.2 Numerical simulations

As discussed in Section 1.2.2, the dynamical evolution of GCs is dominated by two-body interactions. Whereas the dynamical models presented in Section 2.1 provide a good representation of the stellar system at a given time, numerical simulations prove to be a more helpful method to study the evolution of GCs.

This Section introduces two commonly used numerical approaches to simulate GCs: direct N-body and Monte Carlo (MC) simulations. The analysis presented in this thesis uses simulated GCs evolved with the Monte Carlo method. However, a broad description of the direct N-body method helps to better understand the MC models.

2.2.1 Direct N-body simulations

Direct N-body simulations are used for various astrophysical problems and different spatial scales: from planetary systems, stellar systems, galaxies to galaxy clusters scales. The main advantage is that N-body simulations do not assume any particular dynamical evolution and instead directly follow the gravitational interactions between the particles (e.g. planets, stars, dark matter). The direct N-body method follows each particle by solving the gravitational force equation, which corresponds to a system of N equations:

$$\frac{d^2\mathbf{x}_i}{dt^2} = -G\sum_{j\neq i}^{N} m_j \frac{\mathbf{x}_j - \mathbf{x}_i}{|\mathbf{x}_j - \mathbf{x}_i|^3}, \tag{2.21}$$

where $\mathbf{x}_i$ is the position vector of the i-th particle in the system, m_i its mass and G the gravitational constant. The direct N-body method evolves the position and velocities

of each particle given a short time step Δt. An important component in the precision of the simulated system is the size of the time step, particularly for GC like systems where close encounters between stars are dominant and the presence of binaries plays a significant role. The implementation of variable time-steps and high-order integrators helped to reduce their computational cost (Makino, 1991).

The first algorithms for solving the N-body problem appeared in the early 1960s (von Hoerner, 1960; Aarseth, 1963) with up to a few tens of stars. The development of more extensive simulations, particularly for GC-like systems, has continued on par with the improvement of computational power, in particular for simulations evolved using software libraries such as the `nbody` code (see Aarseth, 1999, for a review up to its 6th iteration, `nbody6`) and `Starlab` (Hut, 2003). The need for more computational power pushed for creating specific machines like `GRAPE` (Sugimoto et al., 1990) and `HARP` (Makino et al., 1993), and the development of highly parallelisable codes that currently run on graphic processing units (GPUs, Berczik et al., 2011; Nitadori & Aarseth, 2012; Wang et al., 2015). The largest direct N-body simulation today contains 10^6 stars (Wang et al., 2016).

Direct N-body simulations have been instrumental for understanding the dynamical evolution of GCs. From exploring the evolution of binaries (McMillan et al., 1990; Trenti et al., 2007a), core-collapse and post core-collapse evolution (Spurzem & Aarseth, 1996), mass loss under realistic tidal fields (Fukushige & Heggie, 2000; Baumgardt & Makino, 2003; Ernst et al., 2009), internal rotation (Ernst et al., 2007; Tiongco et al., 2017, 2018), the retention of stellar mass BHs (Breen & Heggie, 2013a,b; Sippel & Hurley, 2013; Wang et al., 2016), formation of IMBHs (Portegies Zwart et al., 2004; Rizzuto et al., 2021) and their effects (Baumgardt et al., 2005; Trenti et al., 2007b; Noyola & Baumgardt, 2011; Lützgendorf et al., 2013c), to multiple stellar populations (Vesperini et al., 2013; Mastrobuono-Battisti & Perets, 2013; Hong et al., 2015; Hénault-Brunet et al., 2015; Gavagnin et al., 2016; Mastrobuono-Battisti & Perets, 2016; Tiongco et al., 2019) and their possible origin through mergers between GCs (Amaro-Seoane et al., 2013; Hong et al., 2015; Mastrobuono-Battisti et al., 2019), to name some examples. N-body simulations aiming to represent specific GCs (e.g., Hurley et al., 2008; Heggie & Giersz, 2014, for M4) have also motivated the development of large libraries to constraint structural parameters and dynamics of GCs (Baumgardt, 2017; Baumgardt & Hilker, 2018; Baumgardt et al., 2019a).

2.2.2 Monte Carlo simulations

In the same way that the collisionless Boltzmann equation describes the evolution of the DF for collisionless systems, the Fokker-Plank equation describes the temporal evolution of a DF when diffusive effects, such as two-body encounters, are significant. By solving

the Fokker-Plank equation, it is possible to follow the evolution of stellar systems dominated by relaxation processes. The Monte Carlo (MC) approach provides a statistical way to solve the Fokker-Plank equation (Hénon, 1971b; Spitzer & Hart, 1971).

First, we assume that the stellar system is spherically symmetric and that for time-steps Δt larger than the crossing time and much smaller than the relaxation time, perturbations due to two-body interactions are not relevant. Only their cumulative effect over the relaxation time will significantly change the DF and the gravitational potential. The MC method consists in applying random perturbation to the orbits of tests stars during the time-step Δt. Two main ways have been developed over the years: the first is to follow the orbit of the test stars continuously while the perturbation is applied (Spitzer & Hart, 1971), the second consists in randomly choosing positions on the orbital path of the test stars t then calculate the average perturbation over the orbit (Hénon, 1971b,a).

Although direct N-body and MC approaches are intrinsically different, the later has been developed tested to resemble GCs evolved via direct N-body simulations (see, eg., Giersz et al., 2008, 2013). The main advantage of MC simulations over N-body is that they are comparatively inexpensive in terms of computational requirements, which permits evolving more extensive simulations ($N \sim 10^5 - 10^6$ stars) in a shorter time and exploring a broader sample of initial conditions.

MC simulations have also been developed to study the dynamical evolution of GCs (Giersz, 1998, 2001), exploring the presence of binaries and formation scenarios for blue-stragglers stars (Giersz & Spurzem, 2000; Fregeau et al., 2003; O'Leary et al., 2006; Hypki & Giersz, 2013) and, more recently, multiple stellar populations in GCs (Vesperini et al., 2021; Sollima, 2021). MC simulations have been particularly successful in exploring the retention and subsequent evolution of stellar-mass black holes in GCs (Morscher et al., 2013, 2015). This has allowed different works comparing MC simulations to observable properties of Milky Way's GCs to estimate the retained fraction of stellar-mass BHs (Askar et al., 2018b; Weatherford et al., 2020). Furthermore, MC simulations have been very successful to follow up the dynamical formation channels for binary black hole mergers and observation rates (O'Leary et al., 2006; Rodriguez et al., 2016; Askar et al., 2017; Hong et al., 2018). MC simulations have also explored different formation scenarios for IMBHs (Giersz et al., 2015; González et al., 2021) and binary black hole mergers rates under the presence of a central IMBH (Hong et al., 2020).

The MC simulations used throughout this thesis are part of the `MOCCA`-Survey I (Askar et al., 2017), which is a collection of around 2000 simulated GCs with different initial conditions and evolved with the "MOnte Carlo Cluster simulAtor" (`MOCCA`) code. The `MOCCA` code, developed by Giersz et al. (2013); Hypki & Giersz (2013), follows the orbit-average implementation first described by Hénon (1971b) and further improved by

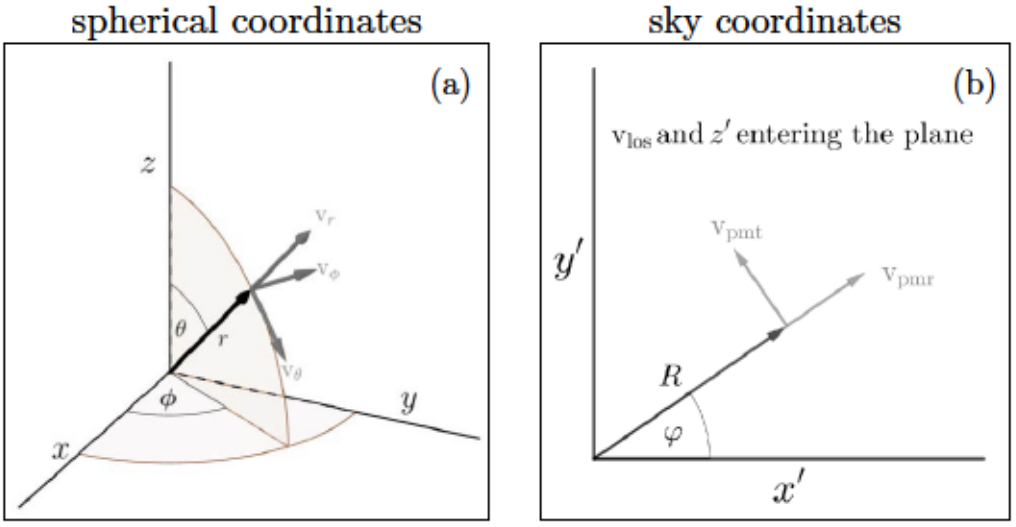

FIGURE 2.5: Spherical (a) and sky (b) coordinate systems used throughout this thesis.

Stodolkiewicz (1986). In Sections 3.2.1 and 4.2.1 specific implementations of the code and their importance for the research presented in this thesis are discussed further.

2.2.3 From simulations to observed kinematics

The analysis presented in Chapters 3, 4 and 5 requires the positions and velocities of each single and binary star in sky coordinates, that is defined by the position (x', y') in the sky, the line-of-sight velocity v_{los} (or radial velocity, RV) and the radial v_{pmr} and tangential v_{pmt} proper motions (see panel (b) of Figure 2.5). Clusters evolved with `MOCCA` have spherical symmetry, so single and binary stars have only (r, v_r, v_t). Therefore, we need to randomly sample the missing spherical coordinates $(\theta, \phi, v_\theta, v_\phi)$ before transforming the positions and velocities into cartesian coordinates and subsequently to sky coordinates.

First we randomly sample values of θ and ϕ, uniformly over a sphere. This is done by sampling values from a uniform distribution, so that:

$$\phi = U(0, 2\pi) \tag{2.22}$$

$$\cos(\theta) = U(-1, 1) \tag{2.23}$$

Then we sample v_θ and v_ϕ so that $v_t^2 = v_\theta^2 + v_\phi^2$ and:

$$v_\theta = v_t \cos(\omega) \tag{2.24}$$

$$v_\phi = v_t \sin(\omega) \tag{2.25}$$

where ω is sampled form an uniform distribution between 0 and 2π.

With the full spherical coordinates for each single and binary star, we transform into cartesian coordinates following:

$$x = r\cos(\phi)\sin(\theta) \tag{2.26}$$
$$y = r\sin(\phi)\sin(\theta) \tag{2.27}$$
$$z = r\cos(\theta) \tag{2.28}$$
$$\mathrm{v}_x = \mathrm{v}_r\cos(\phi)\sin(\theta) - \mathrm{v}_\phi\sin(\phi) + \mathrm{v}_\theta\cos(\phi)\cos(\theta) \tag{2.29}$$
$$\mathrm{v}_y = \mathrm{v}_r\sin(\phi)\sin(\theta) + \mathrm{v}_\phi\cos(\phi) + \mathrm{v}_\theta\sin(\phi)\cos(\theta) \tag{2.30}$$
$$\mathrm{v}_z = \mathrm{v}_r\cos(\theta) - \mathrm{v}_\theta\sin(\theta) \tag{2.31}$$

Equations 2.26 to 2.31 give us the positions and velocities for every single star and the centre of mass of binary stars. In Chapter 4, we study the effects of binary stars in the observed kinematics and their behaviour under the presence of an IMBH. For this analysis, we need the individual velocities for each component of the binary star. In addition to the positions and velocities for the centre of mass of binary stars and the stellar parameter for each component (mass, luminosity, size, stellar types and magnitudes), the semi-major axis a and eccentricity e for each binary orbit are directly obtained as output of the `MOCCA` simulation.

If no external forces are acting on the binary, the motion of each binary component reduces to a single Keplerian orbit[2] with period T and angular momentum L given by:

$$T = 2\pi\sqrt{\frac{a^3}{G(m_1+m_2)}}, \tag{2.32}$$
$$\mathrm{L} = \frac{2\pi a^2}{T}\sqrt{1-e^2}, \tag{2.33}$$

where m_1 and m_2 are the masses of each binary component, while the semi-major axis a and eccentricity e are known from the simulation. Then, the position and velocity along the Keplerian orbit in polar coordinates (r, φ) is given by:

$$r(\varphi) = \frac{a(1-e^2)}{1+e\cos(\varphi-\varphi_0)} \tag{2.34}$$
$$\mathrm{v}_r(\varphi) = \frac{e\sin(\varphi-\varphi_0)}{1+e\cos(\varphi-\varphi_0)}\frac{\mathrm{L}}{r(\varphi)} \tag{2.35}$$

where φ_0 is the orbital phase that, for simplicity, we set $\varphi_0 = 0$. We find the radial position and velocity at a given time t using $\varphi(t) = (2\pi/T)t$, and select a random position along the orbit by sampling from a uniform distribution between 0 and T for each binary star. Note that due to our assumption on the orbital phase, the two binary components

[2]This is the well-known two-body problem, in which the equations of motion for each component combine into a single equation, where the positions are measured with respect to the binary centre of mass and the binary components are represented by a single object with reduced mass of $\mu = (m_1 m_2)/(m_1+m_2)$.

will be at their closest distance at $t = 0$. In Chapter 4, we evaluate the positions and velocities of the binary at different epochs, starting from the initially randomly sampled time.

We transform the position and velocity from polar coordinates to cartesian coordinates $(\mathbf{x}, \mathbf{v})$ and obtain the position and velocities of each component of the binary:

$$\mathbf{x}_1 = \frac{m_2}{m_1 + m_2}\mathbf{x}, \quad \mathbf{v}_1 = \frac{m_2}{m_1 + m_2}\mathbf{v} \tag{2.36}$$

$$\mathbf{x}_2 = \frac{m_1}{m_1 + m_2}\mathbf{x}, \quad \mathbf{v}_2 = \frac{m_1}{m_1 + m_2}\mathbf{v} \tag{2.37}$$

During this process, the orbital plane was constrained in the x-y plane. As a last step, we randomly orientate the orbital plane by selecting two angles sampled uniformly over a sphere (as in equations 2.22 and 2.23) and rotating the orbital plane given those angles. Each binary component's final position and velocity is added to the binary's centre of mass position and velocity.

Once all positions and velocities for single and binary stars are sampled in cartesian coordinates, we transform into sky coordinates. To do so, we take (x, y) as the sky coordinates (x', y'), $-z$ as the line-of-sight direction z', and $-\mathrm{v}_z$ as the line-of-sight velocity $\mathrm{v}_{\mathrm{los}}$. For the radial and tangential proper motions, we transform $(\mathrm{v}_x, \mathrm{v}_y)$ into $\mathrm{v}_{\mathrm{pmr}}$ and $\mathrm{v}_{\mathrm{pmt}}$ with:

$$\mathrm{v}_{\mathrm{pmr}} = \mathrm{v}_x \cos(\varphi) - \mathrm{v}_y \sin(\varphi) \tag{2.38}$$

$$\mathrm{v}_{\mathrm{pmt}} = \mathrm{v}_x \sin(\varphi) + \mathrm{v}_y \cos(\varphi) \tag{2.39}$$

where φ is given by $\varphi = \arctan(y'/x')$[3].

In Chapter 3 and 5 we use the positions and velocities in sky coordinates to construct radial profiles for the kinematics. We use the luminosity of each star also to generate surface luminosity profiles. Section 3.3.1 describes the process to get the radial profiles. In both Chapters, we either exclude the binary stars or use their centre of mass velocity for the kinematics. On the other hand, in Chapter 4, we obtain the observed velocities for binaries by considering a luminosity-weighted velocity combining both components. Section 4.2 describes how we treat the observed kinematics for binary stars.

[3]Please note that for most numerical methods arctan() is defined between $-\pi$ and $+\pi$, we change the range to $(0, 2\pi)$ by adding 2π to the angles with $\varphi < 0$.

Chapter 3

Dynamical modelling of globular clusters: challenges for the robust determination of IMBH candidates

This chapter is in press as "Dynamical modelling of globular clusters: challenges for the robust determination of IMBH candidates" by ***F.I. Aros****, A. C. Sippel, A. Mastrobuono-Battisti, A. Askar, P. Bianchini and G. van de Ven. Monthly Notices of the Royal Astronomical Society, Volume 499, Issue 4, December 2020, Pages 4646–4665,* `https://doi.org/10.1093/mnras/staa2821`*. The labels of a few variables were changed from the original to be consistent with the full thesis.*

3.1 Introduction

With masses between $10^2\,M_\odot$ and $10^5\,M_\odot$, intermediate-mass black holes (IMBHs) are still an elusive population. Ultra-luminous X-ray sources are thought to be accretion signatures of IMBHs, ESO 243-49 HLX-1 being one of the most promising candidates with a minimum mass of $500\,\mathrm{M}_\odot$ (Farrell et al., 2009). Recently the gravitational wave observatories LIGO and Virgo detected a $\sim 140\,M_\odot$ black hole (Abbott et al., 2020a,b). In the local neighbourhood a few candidates have been suggested through dynamical analysis of nearby globular clusters (GCs) (see e.g. Noyola et al., 2008; van der Marel & Anderson, 2010; Lützgendorf et al., 2013a, 2015). Despite their scarce evidence, IMBHs are thought to be the missing link between stellar mass black holes (BHs, with masses of $\sim 10\,M_\odot$) and supermassive black holes (with masses larger than $\sim 10^5\,M_\odot$). Furthermore it has been suggested that IMBHs could be the seeds for supermassive

black holes observed at high redshifts in the early universe (see e.g. Haiman, 2013, for a review). Possible paths for the formation of IMBHs are the direct collapse of a massive star (Madau & Rees, 2001; Spera & Mapelli, 2017) and the runaway merger of stars in dense stellar systems (Portegies Zwart et al., 2004), which happens early in the evolution of the stellar system (see also Giersz et al., 2015). A third path may occur later in the evolution of dense stellar systems, where an IMBH can grow from dynamical interactions (Giersz et al., 2015). The latter two scenarios suggest that a dense stellar systems, such as GCs, could host a central IMBH.

GCs are bound stellar systems of $\sim 10^5 - 10^6$ stars, with total masses around $5 \times 10^5 M_\odot$. As their name suggests, most of them have a characteristic spherical shape. GCs are compact stellar systems with half-light radii[1] of the order of a few parsecs. Their compactness and high stellar density make them bright enough to be observed, not only in our galaxy or the local group but also beyond (Harris & van den Bergh, 1981; Brodie & Strader, 2006). Given their relatively high ages, bigger than $\sim 10\,\mathrm{Gyr}$, GCs are considered the relics of the formation epoch of galaxies (Vandenberg et al., 1996; Carretta et al., 2000). The Galactic GCs half-mass relaxation times range from $\sim 100\,\mathrm{Myr}$ to $\sim 10\,\mathrm{Gyr}$ (Harris, 1996, 2010 edition), making them unique systems for dynamical studies. The short relaxation times allow for mass segregation, i.e. the sorting of higher mass stars towards the cluster centre (Spitzer, 1987), while evolving towards a state of partial energy equipartition (see Spitzer, 1969; Trenti & van der Marel, 2013; Bianchini et al., 2016b).

Different methods have been utilized to find IMBHs in GCs, each relying on two types of signature: accretion of gas by the IMBH or dynamical effects due the presence of the IMBH. On one hand, the accretion signatures in Galactic GCs are dim or non-existent, pointing towards possible IMBHs masses lower than $1000\,M_\odot$ or no IMBHs at all (Tremou et al., 2018). On the other hand, (most of) the IMBH candidates in Galactic GCs have been suggested using dynamical signatures. Stars under the direct influence of the central IMBH will follow a Keplerian potential producing a central cusp in the velocity dispersion profile of the GC (Gebhardt et al., 2002; Noyola et al., 2008, 2010; van der Marel & Anderson, 2010; Lützgendorf et al., 2011, 2012, 2013a, 2015; Kamann et al., 2014, 2016, to name a few).

Even with the vast literature analyzing the dynamical signatures at the centres of GCs, there is still no consensus regarding the presence or absence of IMBHs in Galactic GCs. The central cusp in velocity dispersion is limited to stars within the radius of influence[2] of the IMBH (r_{inf}), which is typically just a fraction of the core radius. Due to the small

[1] Unless mentioned otherwise we refer to half-light radius as the the projected radius containing half of the light in the GC (R_h), while the half-mass radius is the 3D radius containing half of the mass in the GC ($r_{50\%}$).

[2] The radius of influence r_{inf} is the distance from the centre of the GC where the cumulative mass of stars (and stellar remnants) is equivalent to the mass of the central IMBH, and hence depends crucially on the mass of the IMBH.

size of the radius of influence, errors in the determination of the kinematic centre or contamination by bright stars due to crowding in the centre of the GC might hamper the dynamical analysis. Using IFU data of the central region of NGC 5139 (ω Cen), Noyola et al. (2008) find evidence of a $\sim 40000\,M_{\odot}$ IMBH. For the same cluster, using a sample of proper motion from HST, van der Marel & Anderson (2010) only find an upper limit of $18000\,M_{\odot}$ for the possible IMBH. Both studies have a difference in the position of the kinematic centre, separated by 12" (or $\sim 0.3\,$pc at the distance of NGC 5139), which corresponds to $1 \sim 2$ times the $r_{\rm inf}$, depending on the inferred IMBH mass as given above. However, using another sample of radial velocities, Noyola et al. (2010) show that the detection of the IMBH holds for the different kinematic centres. The discrepancy between both estimates could arise from either the different kind of kinematic data or modeling technique applied. Similarly in the case of NGC 6388, where Lützgendorf et al. (2011, 2015) find evidence for an IMBH using velocity maps from integrated spectra, while Lanzoni et al. (2013) do not observe the central velocity dispersion cusp when using the radial velocities of individual stars. More recent observations from IFU with MUSE by Kamann et al. (2018) further support the presence of a central cusp in velocity dispersion. No matter which observational technique is used, the highly crowded centres of GCs add a complex observational challenge.

In addition to the observational limitations due to a small $r_{\rm inf}$, the detection of an IMBH is also made difficult by the limitations in the dynamical models, used to actually identify an IMBH in the observational data. While usually a constant (global) mass-to-light ratio and velocity anisotropy (see Section 3.2.3) are assumed for the dynamical models, these quantities can vary significantly in a GC. For NGC 5139 van der Marel & Anderson (2010) show how an extended dark mass due stellar remnants is also consistent with the observed velocity dispersion profile. This possibility was also recently explored by Zocchi et al. (2019) who uses a multi-mass dynamical model, based on distribution functions, to include a central cluster of stellar-mass black holes, proving that this dark extended population could also produce the central rise in velocity dispersion in NGC 5139. Using a library of N-body simulations, Baumgardt et al. (2019b) also showed that a cluster of stellar-mass black holes at the centre of NGC 5139 was favoured over a central IMBH, in particular due to their distinctive effect on the high velocity stars at the centre of the GC. A similar case was shown by Mann et al. (2019) for 47 Tuc, where a multi-mass dynamical model with a central cluster of black holes was consistent with the kinematic data, ruling out the necessity for a central IMBH suggested by Kızıltan et al. (2017). This has been confirmed by Hénault-Brunet et al. (2019a) with a different type of multi-mass models.

Simulations of GCs with a central IMBH provide us with a benchmark to study the observational and dynamical modelling limitations which hinder a robust detection of an IMBH via its dynamical signatures. Work in this direction has been done by de Vita et al. (2017). In their work, the authors explore the recovery of IMBH masses in GCs

combining Monte Carlo simulations of GCs with a central IMBH (Askar et al., 2017) and mock IFU observations from SISCO (Bianchini et al., 2015), addressing the effects of crowding, contamination due bright stars and the cluster center. They find that, even when the actual mass profile is fully known, it is challenging to detect low-mass IMBH or rule out the IMBH solution in cases without a central IMBH. In addition, they show that when the IMBH is detected, the inferred mass is systematically underestimated. They suggest that the reason could be unquantified effects due energy equipartition and binaries.

In this work we explore the limitations of dynamical modelling based on Jeans equations to detect a central IMBH and the feasibility of rejecting an IMBH solution when it is truly absent. For this, we will assume rather *perfectly* sampled observational data from realistic simulations of GCs and analyse it with simple, but commonly used, dynamical models. We introduce a set of Monte Carlo simulations in Sections 3.2.1 and 3.2.2 and analyze them with Jeans models[3] described in Section 3.2.3. We focus on the limitations in the dynamical modelling itself, which assumes constant mass-to-light ratio and velocity anisotropy (see Section 3.2.3), we apply the same modelling pipeline to the simulated GCs in Section 3.3.1 and then analyse the result of the fittings in Section 3.3.2. In Section 3.4 we discuss the reliability of our dynamical models and we conclude with our summary in Section 3.5.

3.2 Methods and Model Setup

We investigate the kinematic signatures of the presence of an IMBH using Monte Carlo N-body models, evolved to 12 Gyr, to analyze and understand the dynamical signatures of the presence of an IMBH, as described in the following sections.

3.2.1 MOCCA and the Monte Carlo method

The MOCCA-Survey Database I (Askar et al., 2017) is a collection of about 2000 simulated star clusters with different initial conditions that were evolved using the MOCCA code (MOnte Carlo Cluster simulAtor, Hypki & Giersz, 2013; Giersz et al., 2013). The MOCCA code is a 'kitchen sink' package that combines treatment of dynamics with prescriptions for stellar/binary evolution and other physical processes that are important in determining the evolution of a realistic star cluster.

Dense star clusters are collisional systems and their evolution is governed by 2-body relaxation. In MOCCA, the treatment for relaxation is based on the orbit-averaged Monte Carlo method (Hénon, 1971b,a) for following the long term evolution of spherically symmetrical star clusters. This method was subsequently improved by Stodolkiewicz (1982,

[3]Hereafter we refer as 'models' exclusively to the dynamical models.

TABLE 3.1: Initial properties of simulated GCs that were used for our analysis. The first column indicates the simulation name, given by the central object at 12 Gyr, while the second column indicates the symbol used for refer each simulation in all figures. N indicates the initial number of stellar systems, $f_{\rm bin}$ provides the initial binary fraction of the cluster. All these simulations were initially King (1966) models, their central concentration is given by the parameter W_0. $r_{50\%}$ is the initial half-mass radius of the cluster. r_t gives the initial tidal radius. $R_{\rm GC}$ is the Galactocentric radius of the cluster. The final column indicates the prescription for black hole (BH) natal kick, for 'Fallback' cases, BH masses and natal kicks are computed using the mass fallback prescriptions of Belczynski et al. (2002). For 'No Fallback' cases, BHs are given natal kicks that follow a Maxwellian distribution with $\sigma = 265$ kms ^{1} (Hobbs et al., 2005). The metallicity of all simulations was $Z = 0.001$.

Simulation	**Symbol**	**N**	$f_{\rm bin}$ [%]	W_0	$r_{50\%}$ [pc]	r_t [pc]	$R_{\rm GC}$ [kpc]	**Central Density** [$M_\odot$pc^{-3}]	**BH Natal Kicks**
no IMBH/BHS		1.2×10^6	10	6	2.40	60	3.17	9.8×10^4	No Fallback
no IMBH+BHS		1.2×10^6	10	3	1.20	60	3.17	3.1×10^5	Fallback
high-mass IMBH		1.2×10^6	5	9	1.20	60	3.21	3.5×10^7	No Fallback
low-mass IMBH		7.0×10^5	5	9	2.40	60	4.20	2.1×10^6	No Fallback
post core-collapse		1.2×10^6	5	9	7.04	60	3.21	2.3×10^5	No Fallback

1986) and Giersz (1998, 2001). In this approach, relaxation is treated as a diffusive process and velocity perturbations are computed by considering an encounter between two neighboring stars. Energy and angular momentum of stars are perturbed at each timestep to mimic the effects of two-body relaxation. The Monte Carlo method combines the particle based approach of N-body methods with a statistical treatment of relaxation. This allows for inclusion of additional physical processes that are important when simulating the evolution of a realistic star cluster. In `MOCCA`, stellar and binary evolution are implemented using the prescriptions provided by the single (`SSE`) and binary (`BSE`) codes (Hurley et al., 2000, 2002). For computing the outcome of strong dynamical interactions involving binary-single stars and binary-binary stars, `MOCCA` uses the `FEWBODY` code (Fregeau et al., 2004) which was developed to carry out small-N scattering experiments, in which case, the timestep for `FEWBODY` is set to resolve the interaction. Within one `MOCCA` timestep, many of such interactions can occur and it is also the case for binary systems interacting with an IMBH. `MOCCA` also includes a realistic treatment for the escape process in tidally limited star clusters as described by Fukushige & Heggie (2000). In this treatment, the escape of an object from the cluster is not instantaneous but delayed, and some potential escapers can get scattered to lower energies and become bound to the cluster again (Baumgardt, 2001).

The main advantage of using the Monte Carlo method to simulate the dynamical evolution of a realistic star cluster is speed. `MOCCA` can compute the evolution of a million-body star cluster within a week. This advantage makes Monte Carlo codes suitable for probing the influence of the initial parameter space on the dynamical evolution of GCs. Given its underlying assumptions, the Monte Carlo method is limited to simulating spherically symmetric clusters with a timestep that is a fraction of the relaxation time. Therefore, it is well suited for following the long term evolution of a GC, but is not ideal for following the evolution on dynamical timescales. Results from `MOCCA` have been extensively compared with the results for direct N-body simulations (Giersz et al., 2008, 2013; Wang et al., 2016; Madrid et al., 2017). The evolution of global GC parameters and the number of specific objects in `MOCCA` and direct N-body simulations are in good agreement (Wang et al., 2016; Madrid et al., 2017). These comparisons also serve to calibrate free parameters in the `MOCCA` code connected with the escape processes and interaction probabilities (Giersz et al., 2013).

3.2.2 The Monte Carlo simulations

We analyze five simulated GCs with and without IMBHs, taken from the `MOCCA`-Survey Database I (Askar et al., 2017). Their initial conditions are given in Table 3.1 and each is named to indicate the type of central object they contain at 12 Gyr (see also Table 3.2). The *no IMBH/BHS* simulation does not contain an IMBH or a significant number of BHs at 12 Gyr. The *no IMBH+BHS* contains 148 stellar remnants BHs (of the order

of $\sim 10\,M_\odot$ each) at at 12 Gyr. The *high-mass IMBH* cluster hosts a central IMBH of $\sim 13000\,M_\odot$ at 12 Gyr, while the *low-mass IMBH* contains an IMBH of $\sim 500\,M_\odot$ at 12 Gyr. The simulated cluster labeled *post core-collapse* has reached core-collapse at 12 Gyr and does not contain an IMBH or a significant number of stellar mass BHs.

All these GCs initially followed a King (1966) profile and had 1.2×10^6 stellar systems[4], except for the *low-mass IMBH* which initially had 7×10^5 stellar systems. In all cases, a metallicity of $Z = 0.001$ (corresponding to [Fe/H] ~ -1.3) was used for the stars. The initial binary fraction for these simulated GCs is indicated in the third column in Table 3.1, their initial binary properties assume a thermal eccentricity distribution, a uniform mass ratio distribution and a semi-major axis distribution which is uniform in logarithmic scale (between $2(R_1 + R_2)$ and 100 AU, where R_1 and R_2 are the zero-age main sequence stellar radii of the binary components). The simulated GCs had an initial tidal radius of 60 pc and are assumed to have a circular orbit with a velocity of 220 km/s around a point mass like potential for the galaxy, which total mass is equal to the enclosed mass inside the Galactocentric radius of each simulated GC (see Table 3.1).

In all simulated GCs, except the *no IMBH+BHS*, BHs were given the same natal kicks as neutron stars at the moment of formation. The natal kick velocity follows a Maxwellian distribution with $\sigma = 265$ km/s (Hobbs et al., 2005). For the *no IMBH+BHS* cluster, BH masses and natal kicks were modified according to the mass fallback prescription provided by Belczynski et al. (2002). This mass fallback prescription introduces a 'fall back' factor which gives the fraction of the stellar envelope that falls back on the remnant following its formation. This factor can significantly reduce natal kicks for BHs that have progenitors with zero-age main sequence masses between 20 to $50\,M_\odot$. The reduced natal kicks for BHs allows the *no IMBH+BHS* cluster to retain about 1300 BHs after 50 Myr of evolution. It had long been thought that BHs that are retained in GCs would efficiently eject themselves through strong dynamical interactions leaving behind at best 1 or 2 BHs up to a Hubble time (Sigurdsson & Hernquist, 1993; Kulkarni et al., 1993). However, recent theoretical and numerical works have shown that BH depletion might not be so efficient and GCs with moderately long relaxation times that are dynamically young could contain a sizeable number of BHs up to a Hubble time (Morscher et al., 2013; Sippel & Hurley, 2013; Breen & Heggie, 2013a,b; Heggie & Giersz, 2014; Morscher et al., 2015; Wang et al., 2016; Arca Sedda et al., 2018; Askar et al., 2018b; Weatherford et al., 2018, 2019; Kremer et al., 2019). In the same way, the presence of BHs in globular clusters has been sugested by the combination of radio and X-ray observations (Maccarone et al., 2007; Strader et al., 2012a; Chomiuk et al., 2013; Miller-Jones et al., 2015; Bahramian et al., 2017; Shishkovsky et al., 2018; Dage et al., 2018), and kinematics (Giesers et al., 2018, 2019). These observation suggest the posibility of multiple BHs in

[4]In this context, single and binary systems are understood as 'stellar systems'. The simulated clusters start with 1.2×10^6 single+binary systems, rather than 1.2×10^6 stars.

GCs. At 12 Gyr, the *no IMBH+BHS* model has lost a significant fraction ($\sim 90\%$) of its retained BHs as the cluster evolves, but still retains about 148 of them.

The two simulated clusters that include a central IMBH are called *high-mass IMBH* and *low-mass IMBH*. Both follow the formation scenarios and growth of IMBHs in GCs as seen in `MOCCA` simulations, which are described in Giersz et al. (2015) and summarized in the following (see also Arca Sedda et al., 2019, for an analysis on all `MOCCA` simulations that include an IMBH). The *high-mass IMBH* cluster had initially a central density of $3.5 \times 10^7\, M_\odot \mathrm{pc}^{-3}$. Typically, for simulations with such high central densities, runaway mergers of main sequence stars in the first 50 Myr lead to the formation of massive main sequence stars which can then form an IMBH seed either through a merger or collision with a stellar mass BH or through direct collapse (see e.g. Portegies Zwart et al., 2004; Spera & Mapelli, 2017). This formation scenario occurs early in the evolution of the GC and is described as the 'FAST' scenario in Giersz et al. (2015). On the other hand, in the model *low-mass IMBH* model, the IMBH forms after more than 9 Gyr of cluster evolution via the 'SLOW' scenario described in Giersz et al. (2015). In this scenario, the IMBH forms from the growth of a stellar mass BH by mergers and collisions during the core collapse stage of cluster evolution. The IMBH formed via the 'SLOW' scenario have masses in the range of $10^2 - 10^3\, M_\odot$ at 12 Gyr. Both simulations with a central IMBH do not have any stellar BHs within $r_{50\%}$, because the IMBH efficiently ejects or merges with stellar mass BHs in the cluster (Leigh et al., 2014; Giersz et al., 2015).

The channel of formation also has an impact on the interaction between the IMBH and the surrounding stars. IMBHs formed early on through the 'FAST' scenario produce a more clear central rise in velocity dispersion, while an IMBH formed via the 'SLOW' scenario could lack such clear features at 12 Gyr, as it forms later on during the evolution of the GC (Giersz et al., 2015). In principle, in MOCCA simulations, a low-mass IMBH can wander around the centre of the cluster, which in turn can hamper the formation of the velocity dispersion cusp. As the IMBH mass grows its movement around the center decreases, and it should stay fixed for IMBHs with $M_\bullet > 1000\, M_\odot$. In MOCCA simulations, IMBHs with $M_\bullet > 1000 \sim 2000\, M_\odot$ should produce a clear central rise in the velocity dispersion and surface brightness profiles (Giersz et al., 2015).

At 12 Gyr the IMBH in the *low-mass IMBH* simulation is almost the innermost object, however, its displacement with respect to the cluster centre is small (2×10^{-4} pc or ~ 10 mas at 5 kpc) and it should not have an effect in the dynamical models. However, as pointed out by de Vita et al. (2018), through direct N-body simulations, large displacements of an IMBH with respect the cluster centre will require tailored data-modelling comparisons and dynamical models under the assumption of spherical symmetry (as the one used in this work and described below in Section 3.2.3) might introduce a bias on the estimated masses of the IMBH.

The *post core-collapse* simulation starts out as tidally-filling, with a half-mass radius of $\sim$ 7 pc. The cluster undergoes stronger mass loss due to tidal stripping which decreases the number of stars and shortens its relaxation time. Therefore, the cluster is dynamically older and has evolved to a post core-collapse phase at 12 Gyr.

For all the five simulated GCs, we extracted the 12 Gyr `MOCCA` snapshot which contains the radial position, radial velocity, tangential velocity and stellar parameters of each star. The details of how the snapshot was used for our dynamical modelling is provided in subsequent sections. In Table 3.2, we provide the 12 Gyr properties of each of the five simulated clusters. We have included in this table, the total mass of the cluster ($M_{\rm tot}$), its half-mass ($r_{50\%}$) and half-light radii (R_h), total luminosity ($L_{\rm tot}$), binary fraction ($f_{\rm bin}$), mass-to-light ratio within the half-mass radius ($\Upsilon_{50\%}$), the inner ($\beta_{50\%}$) and outer velocity anisotropy ($\beta_{\rm out}$, see Equation 3.3), the mass of the central IMBH ($M_\bullet$) and the total mass in stellar BHs ($M_{\rm bh}$) within the half-mass radius.

3.2.3 Dynamical modelling

We build dynamical models to characterize the 3D mass profile of the simulated GCs. Our models are built by solving the Jeans equations (Jeans, 1922), which allows us to characterize the internal dynamical state of a stellar system via the velocity moments of its distribution function (DF) $f(\mathbf{x}, \mathbf{v})$. The following description of the Jeans equations is based on Chapter 4 of Binney & Tremaine (2008) and Section 2 of van der Marel & Anderson (2010).

The dynamical state of a collisionless system is fully determined by the Collisioneless Boltzmann Equation:

$$\frac{\partial f}{\partial t} + \sum_{i=1}^{3} \left(v_i \frac{\partial f}{\partial x_i} - \frac{\partial \Phi}{\partial x_i} \frac{\partial f}{\partial v_i} \right) = 0 \,, \tag{3.1}$$

which represents the conservation of the probability of finding a star within the phase-space of position $\mathbf{x}$ and velocity $\mathbf{v}$ given the DF $f(\mathbf{x}, \mathbf{v})$ and the potential Φ. However, solving and relating Equation 3.1 to observable quantities is not trivial. A simpler approach is to integrate Equation 3.1 over the velocity space assuming the system is in equilibrium ($\partial f / \partial t = 0$). This provides a set of equations, known as Jeans equations, depending only on the velocity moments, rather than on the more complex DF. The zeroth velocity moment will correspond to the probability of finding a star at a certain position $\nu(\mathbf{x})$. This is not a direct observable and it has to be evaluated using either the number density $n(\mathbf{x}) = N_{\rm tot}\nu(\mathbf{x})$ or the luminosity density $j(\mathbf{x}) = L_{\rm tot}\nu(\mathbf{x})$ as proxies (where $N_{\rm tot}$ and $L_{\rm tot}$ are the total number of stars and total luminosity). Here we use the latter as proxy of the zeroth velocity moment and express all the equations below in terms of $j(\mathbf{x})$ rather than $\nu(\mathbf{x})$. The first velocity moment is the mean velocity $\langle \mathrm{v} \rangle$,

TABLE 3.2: Summary of the properties of the simulated GCs at 12 Gyr. These values were measured directly from the simulations. The first column indicates the simulation name, given by the central object at 12 Gyr, while the second column indicates the symbol used for refer each simulation in all figures. The number of stellar systems (N) includes single and binaries stars. $M_{\rm tot}$ is the total mass of the cluster and $r_{50\%}$ is the half-mass radius, while $L_{\rm tot}$ is the total cluster luminosity and R_h is the projected half-light radius. The binary fraction ($f_{\rm bin}$) represent the global fraction including all stellar systems in the simulation. The half-mass mass-to-light ratio ($\Upsilon_{50\%}$) and the half-mass velocity anisotropy ($\beta_{50\%}$) were measured including all stellar systems within the half-mass radius ($r_{50\%}$), while the outer velocity anisotropy ($\beta_{\rm out}$) includes all stars with radii larger than $r_{50\%}$. $M_\bullet$ is the mass of the central IMBH, while $M_{\rm bh}$ is the total mass of stellar black holes within $r_{50\%}$.

Simulation	**Symbol**	**N**	$M_{\rm tot}$ $[\times 10^5\, M_\odot]$	$r_{50\%}$ [pc]	$L_{\rm tot}$ $[\times 10^5\, L_\odot]$	R_h [pc]	$f_{\rm bin}$ [%]	$\Upsilon_{50\%}$ $[M_\odot/L_\odot]$	$\beta_{50\%}$	$\beta_{\rm out}$	$M_\bullet$ $[M_\odot]$	$M_{\rm bh}$ $[M_\odot]$
no IMBH/BHS		1048918	3.56	5.29	1.99	2.50	6.8	1.38	0.03	0.12	0.0	39.98
no IMBH+BHS		971004	3.29	4.99	1.81	2.84	5.7	1.39	0.11	0.37	0.0	1437.61
high-mass IMBH		942585	3.07	5.50	1.81	2.63	2.0	1.26	0.10	0.30	12883.4	0.0
low-mass IMBH		496159	1.70	6.13	0.95	2.02	3.0	1.40	0.04	0.08	519.3	0.0
post core-collapse		388631	1.42	5.14	0.83	1.91	3.7	1.24	0.00	-0.03	0.0	15.60

while the second velocity moment $\langle v^2 \rangle = \sigma^2 + \langle v \rangle^2$ includes the effects of the velocity dispersion σ and the mean velocity $\langle v \rangle$.

We build spherically symmetric dynamical models by assuming a DF that depends only on the Hamiltonian $H(\mathbf{x}, \mathbf{v})$ and the total angular momentum L. For these models, the first velocity moments are $\langle v_r \rangle = 0$, $\langle v_\varphi \rangle = 0$ and $\langle v_\theta \rangle = 0$, while for the second velocity moments $\langle v_\varphi^2 \rangle = \langle v_\theta^2 \rangle$ holds. This allows to define a tangential component as $\langle v_t^2 \rangle = \langle v_\theta^2 \rangle + \langle v_\phi^2 \rangle$ and have an expression for the Jeans equation, which depends only of two unknowns variables $\langle v_r^2 \rangle$ and $\langle v_t^2 \rangle$:

$$\frac{d}{dr}\left(j(r)\langle v_r^2 \rangle\right) + j(r)\left(\frac{d\Phi}{dr} + \frac{2\langle v_r^2 \rangle - \langle v_t^2 \rangle}{r}\right) = 0\,. \tag{3.2}$$

The dependency of the second velocity moments $\langle v_r^2 \rangle$ and $\langle v_t^2 \rangle$ is usually described by the velocity anisotropy β as:

$$\beta = 1 - \frac{\langle v_t^2 \rangle}{2\langle v_r^2 \rangle}\,, \tag{3.3}$$

(see Binney & Tremaine, 2008) which could take any functional form and allows us to rewrite Equation 3.2 as follows:

$$\frac{d}{dr}\left(j(r)\langle v_r^2 \rangle\right) + \left(j(r)\langle v_r^2 \rangle\right)\left(\frac{2\beta}{r}\right) = -\frac{d\Phi}{dr}\,. \tag{3.4}$$

In our case, we assume a constant velocity anisotropy through the stellar system, under this condition the second velocity moment $\langle v_r^2 \rangle$ is:

$$\langle v_r^2 \rangle(r) = \frac{1}{j(r)r^{2\beta}} \int_r^\infty dr' j(r') r'^{(-2\beta)} \frac{\partial \Phi}{\partial r'}(r')\,. \tag{3.5}$$

The expression for $\langle v_r^2 \rangle$ is embedded into the coordinate system centred in the stellar system, but as external observers we usually do not have the full 6-dimensional information (i.e. the three position and three velocities). At most we have available the individual position of each star projected in the sky (x', y'), the line-of-sight velocity (v_{LOS}), the radial (v_{PMR}) proper motion and the tangential (v_{PMT}) proper motion. These are shown in Figure 3.1.

To relate $\langle v_r^2 \rangle$ with the observations we integrate it along the line-of-sight to get a weighted average for the second velocity moments:

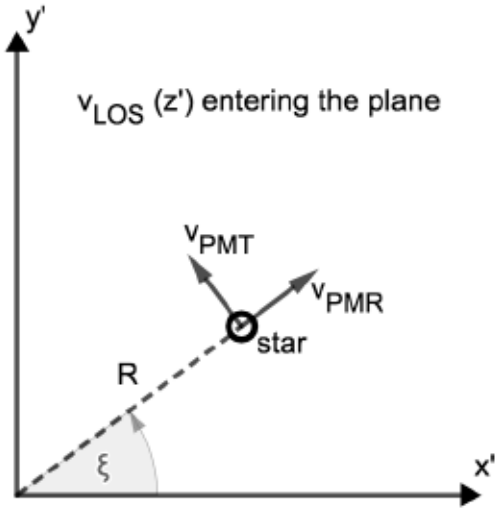

FIGURE 3.1: Sky coordinates for the projected velocity components. The star is located at a projected distance R from the cluster centre in the plane of the sky ($x'y'$ plane). The line-of-sight velocity (v_{LOS}) is perpendicular to the plane of the sky, while the radial proper motion (v_{PMR}) follows the direction of the radial vector defined by R, and the tangential proper motion (v_{PMT}) follows the direction of the ξ angle between R and x'.

$$\langle v^2_{LOS}\rangle(R) = \frac{1}{I(R)}\int_R^\infty \frac{j(r)dr}{\sqrt{r^2-R^2}}\left(1-\beta\left(\frac{r}{R}\right)^2\right)\langle v_r^2\rangle\,, \tag{3.6}$$

$$\langle v^2_{PMR}\rangle(R) = \frac{1}{I(R)}\int_R^\infty \frac{j(r)dr}{\sqrt{r^2-R^2}}\left(1-\beta+\beta\left(\frac{r}{R}\right)^2\right)\langle v_r^2\rangle\,, \tag{3.7}$$

$$\langle v^2_{PMT}\rangle(R) = \frac{1}{I(R)}\int_R^\infty \frac{j(r)dr}{\sqrt{r^2-R^2}}(1-\beta)\langle v_r^2\rangle\,, \tag{3.8}$$

where $R=\sqrt{x'^2+y'^2}$ is the radial distance projected in the sky from the centre of the GC to the star and $I(R)$ is the surface brightness of the GC. We model the surface brightness in a similar way as (van der Marel & Anderson, 2010), using the following function:

$$I(R) = I_0\times(R/a_0)^{-s_0}\times(1+(R/a_0)^{\alpha_1})^{-s_1/\alpha_1}\times(1+(R/a_1)^{\alpha_2})^{-s_2/\alpha_2}\,, \tag{3.9}$$

where, I_0 is a scaling factor, a_0 and a_1 are the inner and outer scale radii, s_0 gives the slope of a possible central cusp, while s_1, s_2 and α_1, α_2 control the mid and outer slopes. This parametric form allows us to to explore a broad range of surface luminosity profiles and easily perform a deprojection to get the luminosity density:

$$j(r) = \frac{-1}{\pi}\int_r^\infty \frac{dR}{\sqrt{R^2-r^2}}\frac{dI}{dR}\,. \tag{3.10}$$

To determine the internal mass density profile, we assume a constant mass-to-light ratio

Υ_0 and define the stellar mass density profile as $\rho_\star(r) = \Upsilon_0 j(r)$. This simplification is commonly adopted. The total mass of the GC contained within the radius r is then $M(r) = M_\bullet + M_\star(r)$, where $M_\bullet$ is the mass of the possible central black hole and $M_\star(r)$ is the stellar mass given by:

$$M_\star(r) = 4\pi \int_0^r \rho_\star(r') r'^2 dr' \,. \tag{3.11}$$

We express the derivative of the potential Φ as:

$$\frac{d\Phi}{dr} = \frac{GM_\bullet}{r^2} + \frac{GM_\star(r)}{r^2} \,, \tag{3.12}$$

where the potential will have a Keplerian component given by the central black hole mass ($M_\bullet$) and an extended component given by the mass distribution of stars ($M_\star$).

3.3 Analysis and Results

3.3.1 Pipeline

For all the different data sets mentioned in Section 3.2.1 and Table 3.2, we have applied the following blind approach, also summarized in Figure 3.2:

(1) For each GC we select a subsample of stars as our kinematic tracers. The selection, which is the same for each of the GCs, impose a luminosity cut and the exclusion of all binary systems.

We selected all stars brighter than one magnitude below the main sequence turn-off as kinematic tracers, which is equivalent to select stars brighter than $m_V = 18.5$ mag at a distance of $D = 5$ kpc (without extinction). As shown in Figure 3.3 for the *no IMBH/BHS* simulation, this selection excludes most of the stellar main-sequence along with the white dwarf sequence and fainter remnants (neutron stars and stellar black holes). Our magnitude cut resembles the fainter limit adopted by Watkins et al. (2015) for HST proper motions of galactic GCs, however, astrometric catalogs can achieve even fainter magnitudes at the central (see Anderson & van der Marel, 2010; Libralato et al., 2018, for HST proper motions) and outer regions of GCs (Heyl et al., 2017; Bianchini et al., 2019a, for HST and Gaia proper motions respectively). On the other hand, while state-of-the-art line-of-sight observations are pushing towards fainter magnitudes, below the main sequence turn-off (e.g. MUSE Giesers et al., 2019), their observational errors are still large compared to the typical velocity dispersion of GCs. The magnitude cut is agreement with such limitations and allows us to compare line-of-sight velocities and proper motions of our selected kinematic tracers. We have included in Figure A.1, in the appendix, the color-magnitude diagrams for all five simulated GCs.

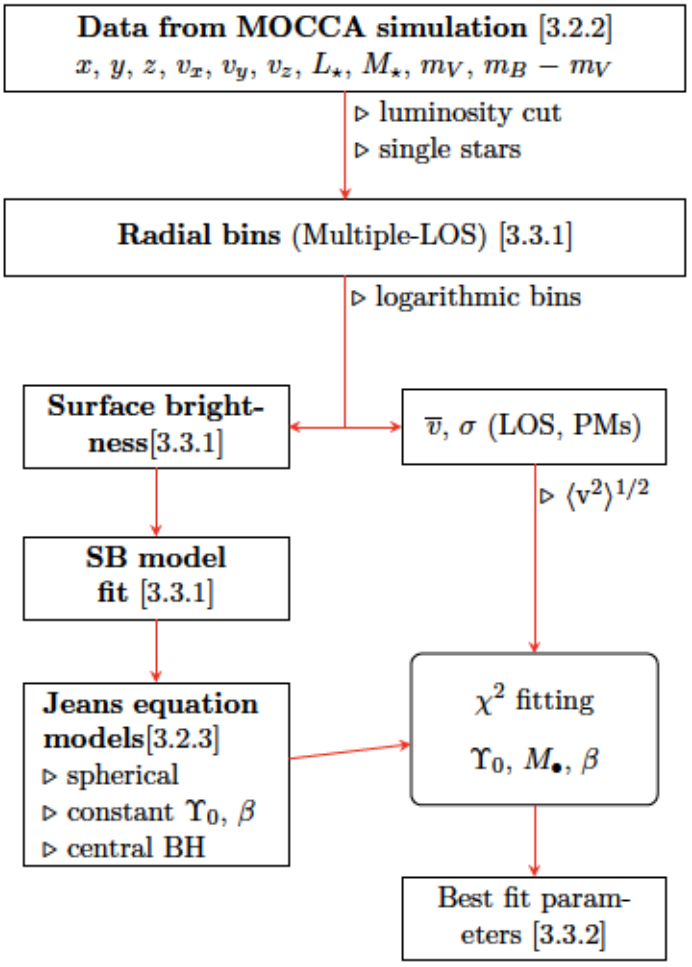

FIGURE 3.2: Pipeline for the dynamical analysis of the simulated GCs as described in Section 3.3.1. We start by extracting the required data from to simulated GCs, projected in the sky, from which we generate surface brightness and kinematic radial profiles. The surface brightness profile is used as an input for the dynamical models, which in turn are fitted to the kinematic profiles.

Within the selected sample of stellar systems in each simulation, a fraction of them will correspond to binary systems (as shown by the open squares in Figure 3.3). Binary stars will have different effects in the measured velocity dispersion depending on the type of kinematic sample. For line-of-sight velocities the observed radial velocity will be dominated by the orbital velocity of the brightest component rather than their centre of mass velocity, this additional velocity will increase the measured velocity dispersion. Panel (a) of Figure 3.4 shows the effect of the binary systems (open squares) in the line-of-sight velocity dispersion compared to a sample that exclude all binaries (filled squares). The individual velocities of each binary component were projected using the `COCOA`[5] code (Askar et al., 2018a), then we used the luminosity weighted velocity for each binary system. The bias produced by the orbital velocities of each binary system increases towards the centre of the cluster where binaries become harder.

[5] `https://github.com/abs2k12/COCOA`

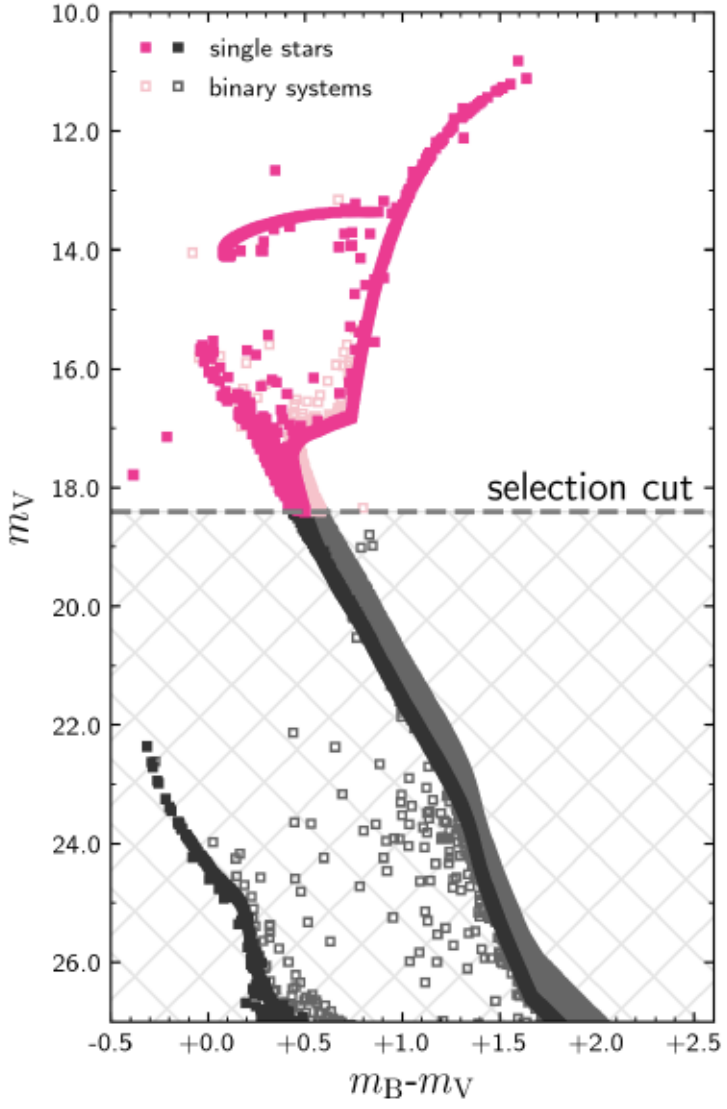

FIGURE 3.3: Color-Magnitude diagram for the *no IMBH/BHS* simulation. Single stars are represented by filled symbols, while binary systems are represented by open symbols. We impose a luminosity cut by selecting all stars brighter than one magnitude below the main sequence turn-off (or an apparent magnitude of $m_V \sim 18.5$ mag at a distance of $D = 5$ kpc, without extinction). This limit is consistent with current observations of line-of-sight velocities and it excludes the most main-sequence stars, the white dwarf sequence, neutron stars and stellar black holes in the cluster.

Panel (b) in Figure 3.4 shows the effects in the line-of-sight velocity dispersion for different populations of binary systems, the short period binaries ($P < 30$ days) dominates the rise in velocity dispersion observed in panel (a), while the long period binaries ($P \geq 1$ year), which do not have a large amplitude in their orbital velocity, have a shallower effect. On the other hand, proper motion velocities will not be significantly affected by the orbital motion of the binary system, as the observations will follow the velocity of the centre of mass.

However, as binary system are more massive than single stars, they will have a systematically lower velocity dispersion than single stars because of partial energy equipartition effects (see Bianchini et al., 2016a, for a discussion). As we expect a larger fraction of binaries towards the centre due mass segregation, the binary systems will bias the measured velocity dispersion to a lower value (see Figure A.2). This will equally affect line-of-sight velocities and proper motions.

Identifying all binaries and excluding them is not usually possible and a few contaminants might remain in real observational samples, even more given our luminosity cut. However, efforts in the direction to identify binary systems in GCs have been done (see for example Milone et al., 2012a; Giesers et al., 2019; Belokurov et al., 2020). The different effects of binaries on the measured velocity dispersion are highly non-trivial and might play against a robust determination of the presence of an IMBH. In this work we explicitly focus on the limitation introduced by the dynamical modelling in the IMBH mass assessment, and we leave for a follow up contribution the detailed study of the complex interplay between presence of binaries and observational biases. Furthermore, the sample without binaries is, within errors, still consistent with the sample that only includes long period binaries, which are more likely to be misidentified with line-of-sight multi epoch observations. For this reason we have excluded all binary systems from our kinematic sample in the current analysis.

(2) Crowding and the determination of the kinematic centre are two observational effects that have played against the robust determination of IMBHs in GCs (Noyola et al., 2008; van der Marel & Anderson, 2010; Lützgendorf et al., 2013a; Lanzoni et al., 2013; de Vita et al., 2017). In the case of the former we assume that we can resolve all stars in the selected sample, while for the centre we use the same centre for the luminosity and kinematics. The grey shaded area in panel (a) of Figure 3.4 shows the effects in the measured velocity dispersion due an error in the kinematic centre determination up to 0.15 pc, approximately 20% of the GC core radius (see de Vita et al., 2017). In comparison the determination of the centre in NGC 5139 is $\sim 10\%$ of its core radius (Noyola et al., 2010).

(3) With the selected sample we generate radial profiles using the projected data in the (x, y) plane. The profiles follow fixed logarithmic radial bins, which allow us to have information in the central region without requiring an excessive number

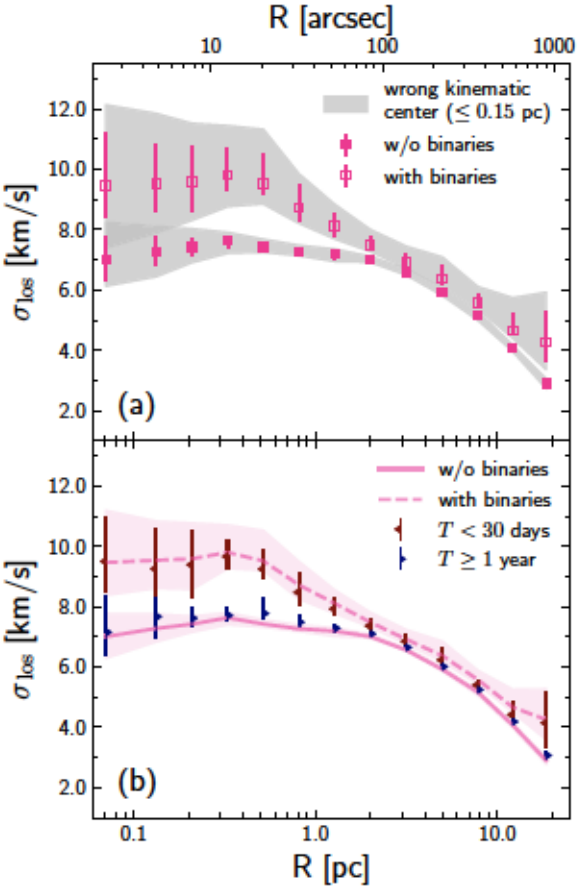

FIGURE 3.4: Line-of-sight velocity dispersion for the *no IMBH/BHS* simulation. The simulated GCs have a non-negligible fraction of binary systems which can increase the observed line-of-sight velocity dispersion, as their measured radial velocity will be dominated by their orbital velocity rather than their centre of mass velocity. The binary systems become harder as their sink towards the centre of the GC. Their intrinsic orbital velocity get larger and its effect in the observed velocity dispersion becomes more significant. Panel (a) shows the measured velocity dispersion for the selected stellar systems (as in Figure 3.3). The sample with binary systems (open squares) has a systematically larger velocity dispersion than the sample which only considers single stellar systems (solid squares), this difference increases towards the center where it becomes $\sim 2\,\mathrm{km/s}$. The gray shaded areas show the effect on the velocity dispersion caused by an error in the kinematic centre up to $\mathrm{R} = 0.15\,\mathrm{pc}$ (or $\sim 6\,\mathrm{arcsec}$ at a distance of 5 kpc), this is equivalent to 20% of the core radius of the GC. Not all binary system have the same influence in the measured velocity dispersion, this is shown in panel (b). Short period binaries (with $P < 30\,\mathrm{days}$, left-side triangles) dominate the increase in velocity dispersion, while binaries with longer periods ($P \geq 1\,\mathrm{year}$, right-side triangles) do not add a significant bias into the velocity dispersion, being similar to the case without binaries. The binary fraction in the selected sample is $f_{\mathrm{bin}} = 7.8\%$ while the fraction of binary stellar system that fall into the short period binaries is only $f_{\mathrm{bin}} = 2\%$. The shaded areas in panel (b) represent the error bars for the samples without binaries and with all binaries.

of bins. Using a fixed binning, and therefore having a varying number of tracers per bin, could potentially lead to low statistics, especially in the central bins. We manage the effect of low statistics by observing the GC from different line-of-sights. As the simulations have spherical symmetry, this approach allows us to have a distribution of values for each bin without altering the intrinsic radial profiles. We sampled 1000 different line-of-sights uniformly distributed in a spherical shell, then for each bin we adopt the median to build the radial profiles and the 16^{th}, and 84^{th} percentiles as an error bar (as the distribution is not necessarily symmetric). Our approach is a simplified version of the projection method described by Mashchenko & Sills (2005), where the probability of each particle to be found in a given bin is calculated as if it were observed from all line-of-sights.

Figure 3.5 shows the luminosity surface density L(R), mass surface density Σ(R), the mean line-of-sight velocity $\overline{v}$(R) and line-of-sight velocity dispersion σ(R) profiles for the *no IMBH/BHS* simulation (pink squares). As a comparison we also include the profiles when all single stars are considered (black diamonds). No major differences are observed regarding the luminosity surface density, as both samples are dominated by the same bright stars (panel (a) in Figure 3.5). The mass surface density of the selected sample is significantly lower than the full sample of single stars, as our selected sample only adds up to the 4.2% of the total mass of the simulated *no IMBH/BHS* cluster. The velocity dispersion is lower in our selected sample within R_h, which is an expected effect of energy equipartition (see e.g. Trenti & van der Marel, 2013; Bianchini et al., 2016b). It is important to be aware of these differences, as our tracers do not provide the full information about the mass profile of the cluster.

(4) We fit the luminosity surface density profile given by the functional form defined in Equation 3.9. This allows us to cover different types of luminosity surface density profiles and deproject them for the dynamical models. We fit the luminosity surface density with `EMCEE` (Foreman-Mackey et al., 2013), a Monte Carlo Markov Chain (MCMC) sampler, which allows us to explore the multi-parameter space. From the fitting we save the best-fit parameters as input for our dynamical models. Figure 3.6 shows the luminosity surface brightness profiles and the fit from our MCMC approach for all the different simulations.

(5) We build a grid of dynamic models via the Jeans equations as described in Section 3.2.3, based on the best-fit parameters to the surface brightness profile. Each model is defined by three parameters: the mass-to-light ratio (Υ_0), the velocity anisotropy (β) and the mass of the central IMBH ($M_\bullet$). The grid is given by the parameter space: $0.5 \leq \Upsilon_0 \leq 3.5$, $-1.0 \leq \log(M_\bullet/M_\odot) \leq 5.0$ and $-1.0 \leq \beta \leq 1.0$.

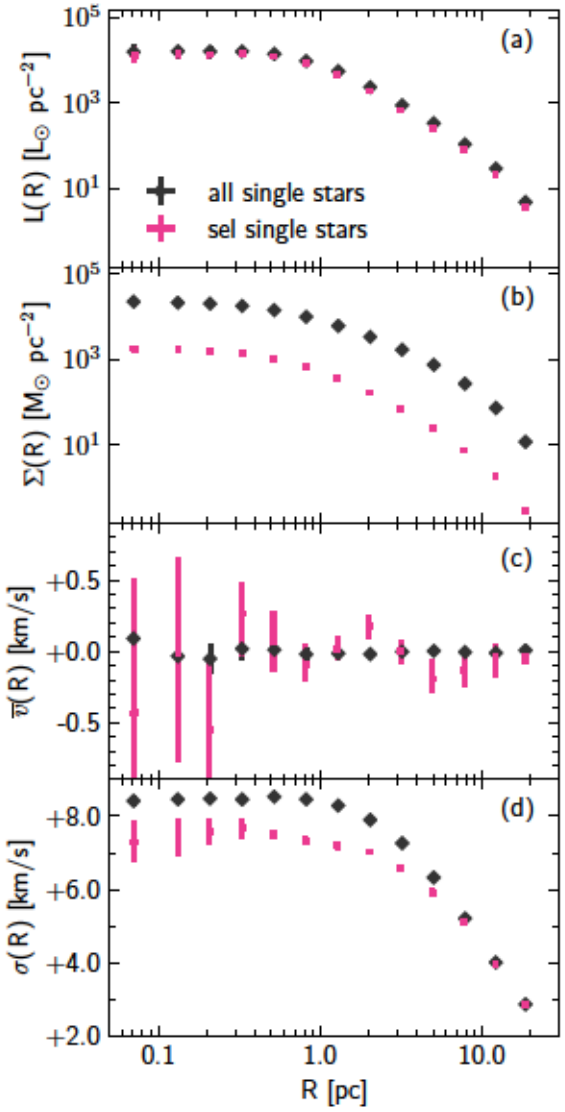

FIGURE 3.5: Radial profiles projected in the sky for the *no IMBH/BHS* simulation. In panel (a), we observe no major difference on the luminosity surface density (L(R)) between all the stars and the selected sample, this is expected as the luminosity surface density is dominated by the bright stars. This is not the case for the mass surface density (Σ(R)) in panel (b) where the selection is approximately ~ 13 times lower than the full sample. Panels (c) and (d) shows the line-of-sight mean velocity and velocity dispersion, only in the latter we observe a $\sim 10\%$ difference within $1\,R_h$ due energy equipartition effects.

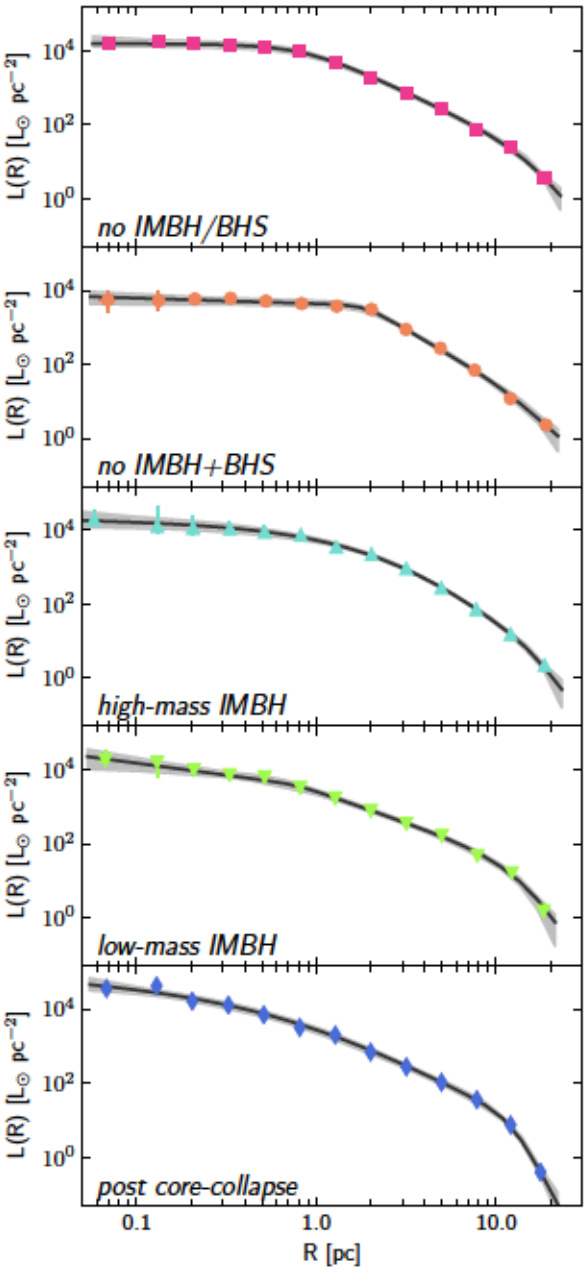

FIGURE 3.6: Surface brightness profile and best fit model. For each GC we fit a functional form for the luminosity surface density as given by Equation 3.9. The best fit in each case (black line) will serve as the main ingredient to our dynamical models, as we assume a constant mass-to-light ratio.

For each model we calculate the Chi-square (χ^2_k) as:

$$\chi^2_k = \sum \frac{\left(\langle \mathrm{v}_k \rangle^{1/2}_{\mathrm{data}} - \langle \mathrm{v}_k \rangle^{1/2}_{\mathrm{model}}\right)^2}{\left(\delta \langle \mathrm{v}_k \rangle^{1/2}_{\mathrm{data}}\right)^2}, \tag{3.13}$$

where k represent each of the observed velocities (LOS, PMR and PMT). We explore the best fit parameters first with only line-of-sight velocities, then with only proper motions and finally with all of them.

3.3.2 Results

We applied the pipeline described in Section 3.3.1 to all simulated GCs introduced in Section 3.2.2 and Tables 3.1 and 3.2. Figure 3.7 shows our fitted dynamical models when only line-of-sight velocities (LOS) are used, while Figure 3.8 shows the case when radial (PMR) and tangential (PMT) proper motions are used together to constrain the best-fit parameters. Figure 3.9, on the other hand, shows the results when LOS and proper motions are used together to constrain the parameters. In each figure we show the respective second velocity moment profiles ($\langle \mathrm{v}^2 \rangle^{1/2}$) used in the χ^2 minimization on the left-side panels and the parameter space on the right-side panels. We adopt three relative $\Delta\chi^2$ regions[6] given by $\Delta\chi^2 = 3.5$, $\Delta\chi^2 = 7.8$ and $\Delta\chi^2 = 11.3$ as a guide to our dynamical model and parameter distribution from the χ^2 minimization. We included the best-fit parameters as an open circle on the right-side panels, while the expected values from the simulation are included as an '$\times$' (see Table 3.2). For the *no IMBH+BHS* simulation, we indicate with an arrow the total mass in stellar black holes within the central parsec of the cluster. Table 3.3 summarizes the best-fit parameters for all models and kinematic data, the errors in each parameter are given by the $\Delta\chi^2 = 7.8$ region in the Figure (approximately 2σ).

3.3.2.1 Constraints from line-of-sight velocities (LOS) only

Our models can identify the presence of a central IMBH inside the two GCs which do indeed contain one (see the right side panels of Figure 3.7). In the case of the *high-mass IMBH* GC, our best fit value is $M_\bullet \sim 2 \pm 2 \times 10^4\, M_\odot$[7]. While we obtain a detection within the $\Delta\chi^2 = 3.5$ region ($\sim 1\sigma$) which also contains the real value ($M_\bullet = 12883.4\, M_\odot$), we cannot fully exclude a lower mass IMBH nor the no IMBH solution with larger confidence levels. This is likely due the lacks of constrains in the velocity anisotropy,

[6] The non-linearity and complexity of our model does not allow us to have a clear value for the degrees of freedom in our χ^2 minimization. The three values adopted here represent the 1σ, 2σ and 3σ for a χ^2 distribution with 3 degrees of freedom. This is the case for the $\Delta\chi^2$ of a linear model with 3 free parameters.

[7] The quoted error bars represent the $\chi^2 \leq 7.8$ confidence region.

TABLE 3.3: Best-fit parameters for all the simulated GCs and velocity data used for the fits. The error bars represent the region defined by $\Delta\chi^2 \leq 7.8$ (approximately 2σ, see footnote 6). The first row for each GC indicates the expected values as indicated in Table 3.2.

Model	Data	Υ_0	$\log(M_\bullet/M_\odot)$	β
no IMBH/BHS		1.38	–	0.03
	RVs	$1.4^{+0.45}_{-0.55}$	$3.3^{+0.75}_{-4.35}$	$-0.4^{+0.55}_{-0.65}$
	PMs	$1.4^{+0.25}_{-0.25}$	$-1.0^{+4.45}_{-0.05}$	$-0.3^{+0.35}_{-0.75}$
	ALL	$1.4^{+0.25}_{-0.25}$	$-1.0^{+4.45}_{-0.05}$	$-0.3^{+0.35}_{-0.45}$
no IMBH+BHS		1.39	–	0.11
	RVs	$1.5^{+0.85}_{-0.75}$	$3.0^{+1.25}_{-4.05}$	$-0.0^{+0.35}_{-1.05}$
	PMs	$1.6^{+0.55}_{-0.55}$	$2.7^{+1.25}_{-3.75}$	$-0.1^{+0.45}_{-0.95}$
	ALL	$1.5^{+0.55}_{-0.35}$	$2.8^{+1.05}_{-3.85}$	$-0.0^{+0.25}_{-0.75}$
high-mass IMBH		1.26	4.11	0.10
	RVs	$1.1^{+0.95}_{-0.65}$	$4.3^{+0.25}_{-5.35}$	$-0.5^{+1.25}_{-0.55}$
	PMs	$1.3^{+0.65}_{-0.55}$	$4.1^{+0.25}_{-0.25}$	$-0.0^{+0.45}_{-1.05}$
	ALL	$1.2^{+0.55}_{-0.45}$	$4.2^{+0.15}_{-0.35}$	$-0.2^{+0.65}_{-0.85}$
low-mass IMBH		1.40	2.72	0.04
	RVs	$1.4^{+0.25}_{-0.35}$	$3.2^{+0.25}_{-0.95}$	$-0.8^{+0.85}_{-0.25}$
	PMs	$1.4^{+0.25}_{-0.25}$	$2.5^{+0.65}_{-3.55}$	$-0.2^{+0.45}_{-0.85}$
	ALL	$1.4^{+0.15}_{-0.25}$	$2.8^{+0.35}_{-3.85}$	$-0.3^{+0.45}_{-0.65}$
post core-collapse		1.24	–	0.0
	RVs	$1.1^{+0.25}_{-0.25}$	$3.0^{+0.35}_{-4.05}$	$-1.0^{+0.95}_{-0.05}$
	PMs	$1.1^{+0.15}_{-0.15}$	$-1.0^{+3.75}_{-0.05}$	$-0.2^{+0.25}_{-0.55}$
	ALL	$1.1^{+0.15}_{-0.15}$	$1.0^{+1.75}_{-2.05}$	$-0.3^{+0.25}_{-0.45}$

as the parameter region with lower mass IMBHs is dominated by highly radial velocity anisotropy ($\beta \gtrsim 0.5$). For the *low-mass IMBH* we find a detection at $\Delta\chi^2 = 7.8$ level ($\sim 2\sigma$), where the IMBH best fit value is $M_\bullet \sim 1.5 \pm 1.4 \times 10^3\, M_\odot$, around 3 times the mass of the actual IMBH ($M_\bullet = 519\, M\odot$). This overestimation goes in hand with the high tangential anisotropy of $\beta = -0.8$, inferred from the best fit model (see discussion in Section 3.4.1 below).

For the *no IMBH/BHS* and *no IMBH+BHS* GCs we obtain upper limits of $M_\bullet \lesssim 11000\, M_\odot$ and $M_\bullet \lesssim 17000\, M_\odot$, respectively. While the whole mass range from the correct solution ($M_\bullet = 0\, M_\odot$) to the just mentioned upper limits is allowed by the model within the $\chi^2 \leq 7.8$ confidence region, the best fit models indicates a central IMBH of $M_\bullet \sim 2^{+11}_{-2} \times 10^3\, M_\odot$ for the *no IMBH/BHS* and $M_\bullet = 1^{+17}_{-1} \times 10^3\, M_\odot$ for the *no IMBH+BHS*. Finally, although the *post core-collapse* GC does not have a central IMBH, the best fit model suggests a central IMBH of $M_\bullet = 1^{+1.5}_{-1} \times 10^3\, M_\odot$, which is detected within 1σ. In a similar fashion than for the *low-mass IMBH*, the inferred mass of the IMBH is bound to a tangential anisotropy ($\beta = -1.0$, at the edge of our parameter space).

As expected, we cannot constrain the velocity anisotropy with only LOS velocities. Figure 3.7 shows the existence of a correlation between the mass of the possible IMBH

and the velocity anisotropy for each of the five analyzed GCs. Dynamical models with a significant tangential anisotropy allow for a larger central IMBH mass (commonly refered to as mass-anisotropy degeneracy, see Section 3.4.1). Note that for all GCs, the correlation becomes stronger for dynamical models with central IMBH masses higher than $1000\,M_\odot$. In all simulated GCs, we observe that our models are consistent with the observed kinematics. For the case of the *no IMBH+BHS* simulation, we notice that our models overestimate the second velocity moment at $R \gtrsim 2R_h$ (or $R \gtrsim 6\,\mathrm{pc}$).

3.3.2.2 Constraints from proper motions (PMs) only

The second velocity moments for the proper motions have a different parametric dependency with the velocity anisotropy (see Equations 3.7 and 3.8), adding an additional constraint. This improves the constraints for our models when compared with the case with only line-of-sight velocities, as the degeneracy between the velocity anisotropy and the mass of the central IMBH is reduced. Our models, however, show some limitations as when using proper motions, they become less consistent with the observed kinematics. For the *no IMBH/BHS*, *low-mass IMBH* and *post core-collapse* GCs, the models fail to mutually fit the radial (PMR) and tangential (PMT) proper motions.

With the additional constraints provided by proper motions, we find a clear 3σ detection for the *high-mass IMBH* GC and a best fit value of $M_\bullet \sim 1.2^{+1.2}_{-0.6} \times 10^4\,M_\odot$, which is consistent with the real mass of the central IMBH.

The best fit for the *low-mass IMBH* reduces to $M_\bullet \sim 0.3^{+1.2}_{-0.3} \times 10^3\,M_\odot$, which slightly underestimates the mass of the central IMBH. While we recover a best fit value which is more consistent with the real IMBH mass, we do not find a clear detection at 1σ nor 2σ, the 2σ errors allow for a range of masses of $[0\,M_\odot, 1584\,M_\odot]$ for the central IMBH.

The constrains for the *no IMBH/BHS* and *no IMBH+BHS* GCs also improve. The upper limits reduces to $M_\bullet \lesssim 3100\,M_\odot$ and $M_\bullet \lesssim 9900\,M_\odot$, respectively. The best fit value for the *no IMBH/BHS* is $M_\bullet \sim 0^{+3.1} \times 10^3\,M_\odot$, which is consistent with no central IMBH. For the *no IMBH+BHS* GC simulation, the best fit is now $M_\bullet \sim 0.5^{+9.4}_{-0.5} \times 10^3\,M_\odot$, more consistent with the no IMBH solution. However, within 2σ it is not possible to fully rule out a higher mass IMBH.

The *post core-collapse* GC also shows an improvement with a best fit IMBH mass which is consistent with zero ($M_\bullet \sim 0.0^{+0.6} \times 10^3\,M_\odot$). The upper limit reduces to $M_\bullet \lesssim 630\,M_\odot$ given the additional constraints on the velocity anisotropy with a recovered value of $\beta = -0.2^{+0.25}_{-0.55}$, which is closer to the actual value obtained from the simulation ($\beta_{50\%} = 0.0$).

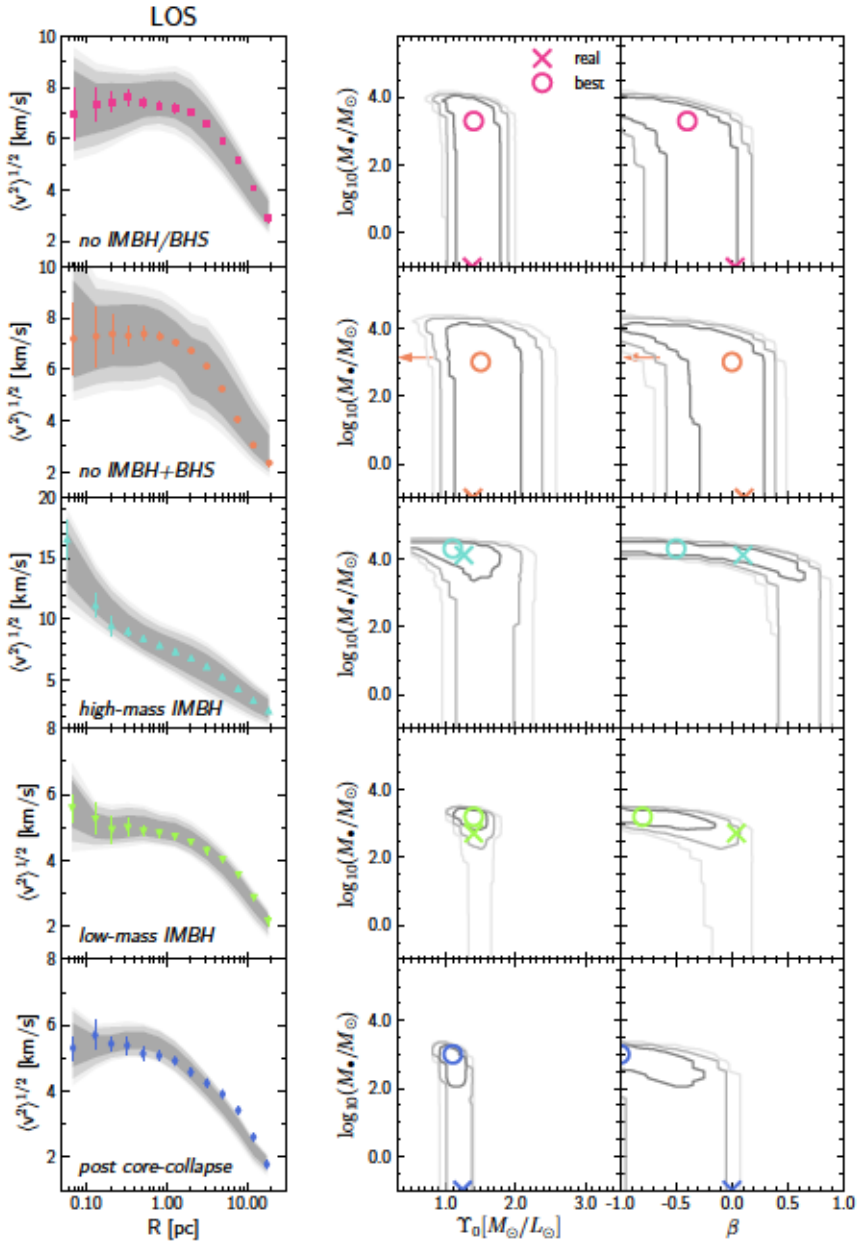

FIGURE 3.7: Fitted dynamical models and parameters space when only line-of-sight velocities (LOS) are used for the fit. The left panels show the measured second velocity moment projected in the sky (colored symbols), while the shaded are represent the $\Delta\chi^2 = 3.5$, $\Delta\chi^2 = 7.8$ and $\Delta\chi^2 = 11.3$ regions (from darker to lighter grey). The right panels shows the parameter space, whereas the circles mark the best-fit values (as in Table 3.3) and the '×' marks the expected value measured directly from the simulations (as in Table 3.2), the contours represent the $\Delta\chi^2 = 3.5$, $\Delta\chi^2 = 7.8$ and $\Delta\chi^2 = 11.3$ regions. For the *no IMBH+BHS* cluster, we indicate with arrows the total mass in stellar black holes (BHS) within the central 1 pc of the cluster. Over all the mass-to-light ratio Υ_0 is well constraint by only using LOS velocities. This is not the case for the velocity anisotropy, as the lack of constraints allows the models to have higher masses for the central IMBH at the cost of more tangential orbits. In the case of the *high-mass IMBH*, the cusp in $\langle v^2 \rangle^{1/2}$ is significant enough to detect the IMBH at its centre.

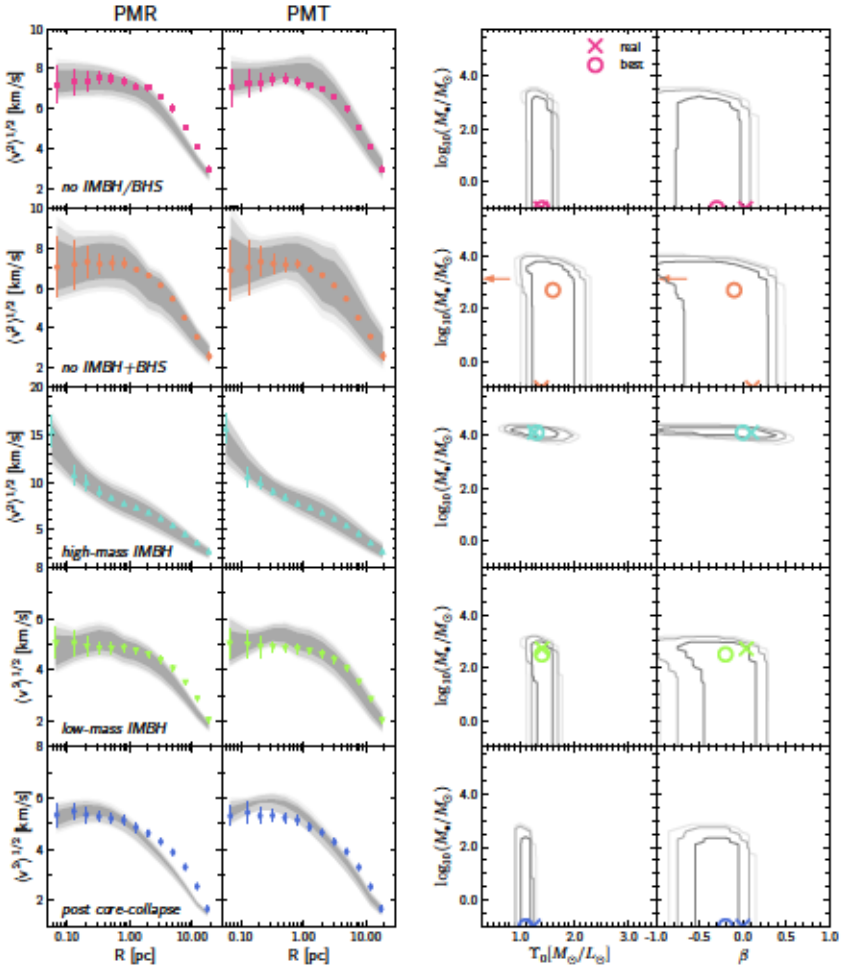

FIGURE 3.8: As in Figure 3.7, but when only the proper motions (PMR and PMT) are used for the fit. The additional data allows to have a better constraint in the velocity anisotropy, excluding all the models with significant tangential orbits. Although, the constraints for the mass of the possible central IMBH are similar to when only LOS are used in the fit.

3.3.2.3 Constraints from the full kinematic sample (LOS+PMs)

When the full kinematic sample is used to constrain the parameter space, as shown in Figure 3.9, we observe similar constraints on the different $\Delta\chi^2$ confidence regions as in the only proper motions case. The IMBH in the *high-mass IMBH* GC is again clearly identified with an inferred mass of $M_\bullet \sim 1.5 \pm 0.9 \times 10^4\, M_\odot$, while for the central IMBH in the *low-mass IMBH* simulation we find $M_\bullet \sim 0.6^{+0.9}_{-0.6} \times 10^3\, M_\odot$ and its presence is recovered within 1σ level. However, for larger confidence regions, we have models that still are consistent with a lower mass or no IMBH solution.

As in the case with only proper motions, the best fit value for the *no IMBH/BHS* GC is consistent with not having an IMBH ($M_\bullet \sim 0^{+3.2} \times 10^3\, M_\odot$), while still allowing a large upper limit ($M_\bullet \lesssim 2800\, M_\odot$). Similarly, for the *no IMBH+BHS* GC, we obtain an upper limit of $M_\bullet \lesssim 7900\, M_\odot$ which has improved from the only proper motion case.

The best fit value is now $M_\bullet \sim 0.6^{+7.3}_{-0.6} \times 10^3\,M_\odot$, the range of masses covered by the 2σ level goes from $0\,M_\odot$ to $7900\,M_\odot$. Also for the *post core-collapse* GC, we find a similar result as when only proper motions are used with an upper limit of $M_\bullet \sim 630\,M_\odot$, while the best fit value of $M_\bullet = 10^{+620}_{-10}\,M_\odot$ is consistent with not having an IMBH.

For all clusters the global mass-to-light ratio (Υ_0) is well constrained, while the velocity anisotropy (β) shows a significant improvement for all clusters with the exception of the high-mass IMBH, once the proper motions are considered (see Figure A.3). In the case of the *high-mass IMBH*, the velocity anisotropy does not show the same level of improvement after including the proper motions, as the Keplerian rise in velocity dispersion dominates over the velocity anisotropy in the inner kinematics. However, their inclusion allows the exclusion of highly radial anisotropic models.

As in the case when only proper motions are considered, we notice that our models are not fully consistent with the kinematic data, this is particularly true for the *post core-collapse* GC. These discrepancies are originating in the assumptions of our models and show the limitations they bring into the fitting. In the following section we discuss further how the assumptions of constant velocity anisotropy and mass-to-light ratio affect the modelling and the detection of a possible IMBH.

3.3.2.4 Additional kinematic samples

To explore the effects of our selection criteria (as described in Section 3.3.1) we applied the dynamical models to three additional kinematic samples. Figure A.5, in the appendix, shows the constraints in the parameter space for the mass-to-light ration and mass of the possible central IMBH for two fainter magnitude cuts: 4.6 mag below the main sequence turn-off, following current lower limits for precise proper motions at the cluster center (Anderson & van der Marel, 2010; Libralato et al., 2018), and 7.5 mag below the main sequence turn-off (Heyl et al., 2017), which is still only possible for proper motions outside the cluster's R_h, but works as an extreme hypothetical case. We do not observe any significant difference with our results for the brightest selection. We notice, though, that for the fainter magnitude cuts the best fit value for Υ_0 increase, this is expected due to the larger fraction of low-mass stars which have a systematically larger velocity dispersion (as in Figure 3.5). The third case we explored includes long period binaries ($P > 1\,\mathrm{yr}$) as in panel (b) of Figure 3.4. The comparison with our main results is illustrated in Figure A.6 and we, once again, do not observe any significant difference between our main results and the sample including long period binaries, which is also expected as both kinematic samples are similar (see Figure A.2).

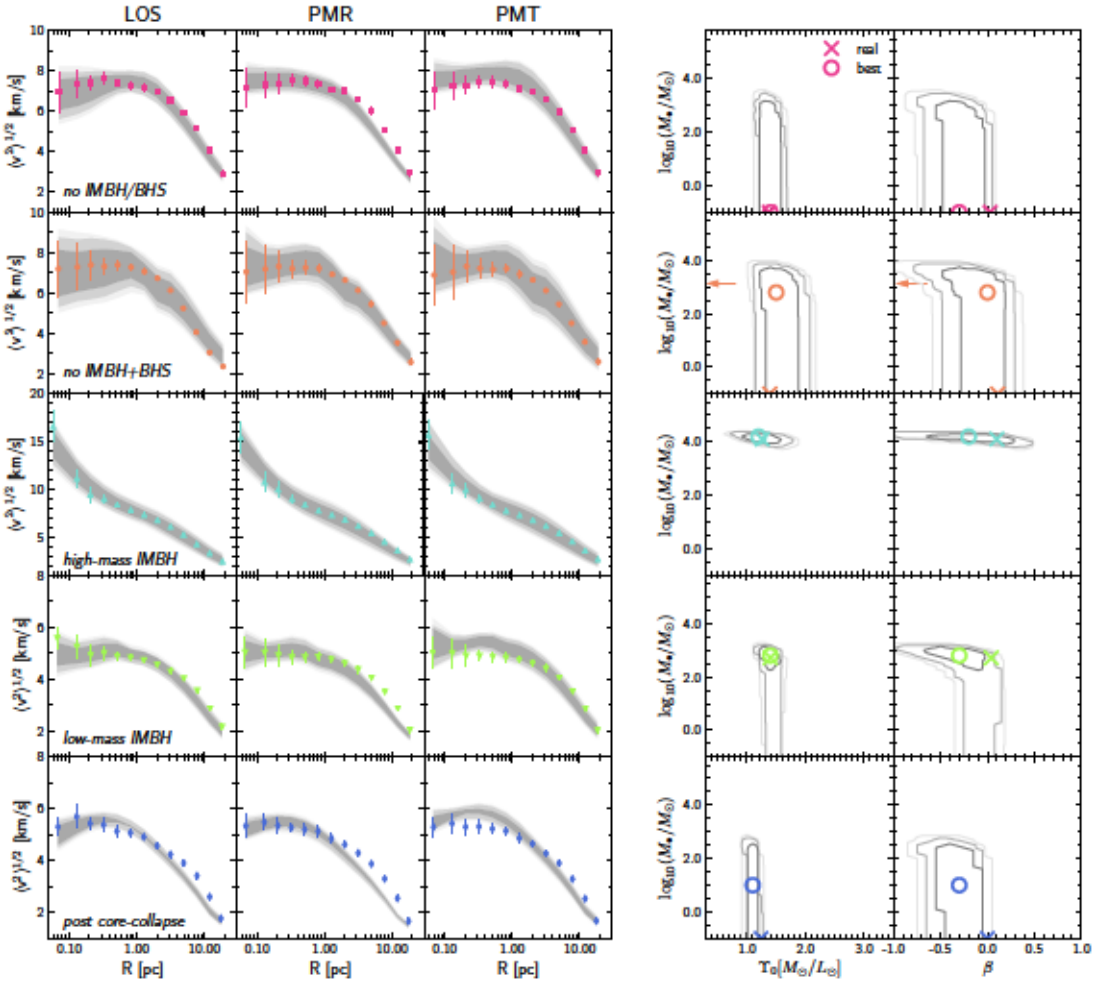

FIGURE 3.9: As in Figure 3.7, but when all velocities (LOS+PMs) are used for the fit. Compared to the constraints from the only PMs case, the fits does not improve significantly when using the full 3D kinematic data. Now we have a detection for the *low-mass IMBH* within the $\Delta\chi^2 \leq 3.5$ level ($\sim 1\sigma$). However, models without an IMBH are still allowed within the uncertainties ($\Delta\chi^2 \leq 7.8$ level, $\sim 2\sigma$). The upper limits on the inferred mass of the possible IMBH in the cases without one are still in the $M_\bullet \leq 1000\,M_\odot$ range.

3.4 Mass constraints from the Jeans models

The two main assumptions in our dynamical models, which could impact in the determination of the presence of an IMBH and its mass, are firstly the constant mass-to-light ratio and secondly the constant velocity anisotropy (see Section 3.2.3). As shown in Figure 3.11, the internal velocity anisotropy and mass-to-light ratio vary for all five GC simulations. The velocity anisotropy increases at large radii for all GCs, other than the *post core-collapse*. The mass-to-light ratio increases towards the centre and at large radii. While the central mass-to-light ratio depends on the type of central object in the cluster, the rise at large radii is similar for all simulations. In this section we explore in detail the effects of these factors on our dynamical models.

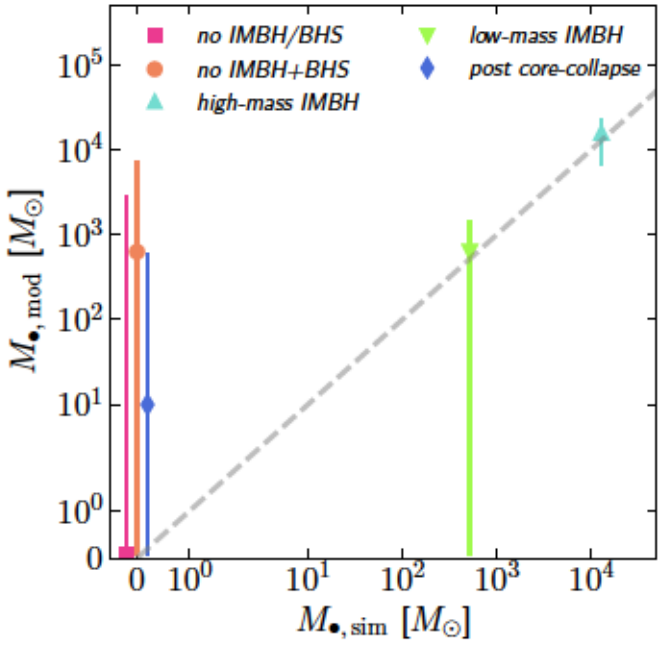

FIGURE 3.10: Recovered IMBHs masses from the full 3D kinematic sample (LOS+PMs). Our dynamical models robustly identify the IMBH in the *high-mass IMBH* simulation ($M_\bullet/M_{GC} = 4.1\%$). However, lower masses or the absence of the central IMBH cannot be excluded for the *low-mass IMBH* case ($M_\bullet/M_{GC} = 0.3\%$). The three simulations without a central IMBH show large upper limits (with an offset from $M_{\bullet,\,sim} = 0.0\,M_\odot$ for visibility).

3.4.1 Velocity anisotropy

The amount of velocity anisotropy in the central region of the GC can affect the measured mass of the possible central IMBH. A radial velocity anisotropy ($\beta > 0$) at the centre can reproduce an increase of the velocity dispersion without requiring additional mass (i.e. an IMBH). On the other hand if the central anisotropy becomes more tangential ($\beta < 0$) the model will require an additional mass in the centre of the GCs. This mass-anisotropy degeneracy is well known in dynamical models based on Jeans equations (see Binney & Mamon, 1982, for example).

The velocity anisotropy can be constrained by including 3D kinematic data namely proper motions, as discussed in Section 3.3.2. However, how strongly the anisotropy can be constrained will depend on the quality of the available proper motions. In the case of NGC 5139, van der Marel & Anderson (2010) show that anisotropic models are necessary to describe its observed kinematics and provide good fits to the observed proper motions without the need for a central IMBH, when using models based on Jeans equations. More recently, Zocchi et al. (2017) also show that models based on anisotropic distribution functions are consistent with the available kinematics of NGC 5139, while their models do not rule out a central IMBH, they put a cautionary note on the estimated mass of the central IMBH. Both works find a velocity anisotropy profile which is (or close-to) isotropic in the centre. However, while van der Marel &

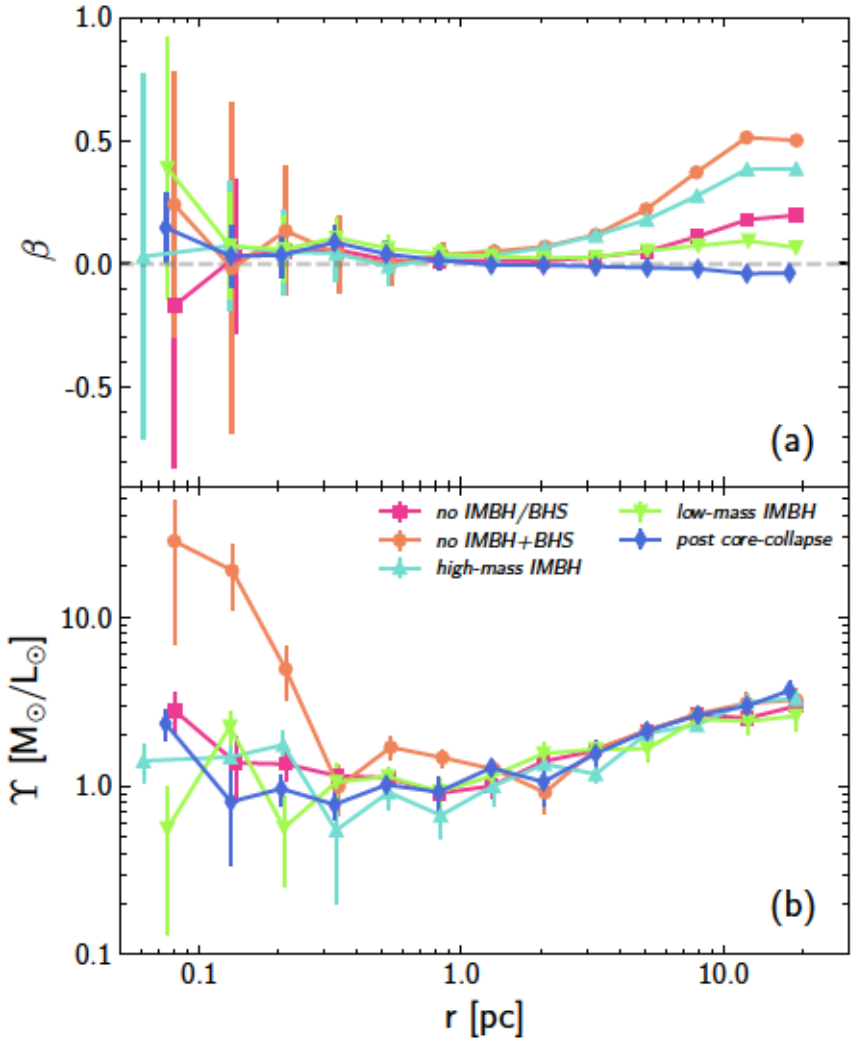

FIGURE 3.11: Velocity anisotropy (a) and mass-to-light ratio (b) profiles for each simulation. All simulated clusters, with the exception of the *post core-collapse*, have central velocity anisotropies consistent with being isotropic ($\beta = 0$) and become more radially anisotropic at large radii. The *post core-collapse* cluster is fairly isotropic at all radii. The stellar mass-to-light ratio (Υ) in the simulations varies with radius, increasing towards the centre and the outer regions of the cluster. The central slope of Υ varies with each cluster, where the *no IMBH+BHS* shows the most significant increase due the stellar black holes subsystem at is centre. On the other hand all simulated GCs shows the same behaviour at large radii.

Anderson (2010) find a tangential anisotropy at large radii, Zocchi et al. (2017) find a radially biased anisotropy profile at large radii (before becoming once again isotropic at the tidal radius). The latter is consistente with Watkins et al. (2015), who show that most galactic globular clusters in the HSTPROMO sample are isotropic towards the centre and become radially anisotropic at large radii. The upper limit on the possible IMBH mass in NGC 5139 suggests a mass-fraction of $M_\bullet/M_{GC} < 0.43\%$ (van der Marel & Anderson, 2010) similar to our *low-mass IMBH* case ($M_\bullet/M_{GC} = 0.30\%$). In this regime, the kinematic signature of the IMBH on the observed velocity dispersion profile is not strong enough for a clear detection and it can be reproduced as well by mildly radial anisotropic models ($\beta \sim 0.1$).

Panel (a) of Figure 3.11 shows the velocity anisotropy for all five GCs measured directly from the simulations. The low number of stars in the central bins is accounted for with the error bars (through bootstrapping in each bin). All GCs except for the *post core-collapse* are consistent with being isotropic at their centre and become more radially anisotropic at larger radii, while the *post core-collapse* is consistent with being isotropic at almost all radii. Once we include the proper motions in our dynamical models, the fits become consistent with an isotropic velocity anisotropy ($\beta = 0$, see Figures 3.8 and 3.9), while still allowing for models with a more tangential anisotropy (within our error bars). The bias toward tangential anisotropy seems to be a common limitation of standard Jeans modelling approaches (e.g. see Read & Steger, 2017).

Figure 3.12 shows the effects of anisotropy in the upper limits of the inferred mass of the central IMBH. Models with a fixed tangential anisotropy ($\beta = -0.1$) increase the inferred IMBH mass, while models with radial anisotropy ($\beta = 0.1$) reduce the upper limit. However, given the constraints from the proper motions, the variation on the upper limit of the inferred IMBH mass due anisotropy is not able to exclude the IMBH solution for the cases without one. The upper limits are still above $M_\bullet \sim 1000\,M_\odot$ ($M_\bullet \leq 630\,M_\odot$ for the *post core-collapse* GC).

3.4.2 Mass-to-light ratio

As shown in panel (b) of Figure 3.11, the mass-to-light ratio of all simulations is generally not constant. The variation with radius is a direct consequence of the two-body relaxation process of collisional systems such as GCs and it has been systematically observed in simulations (Bianchini et al., 2017; Baumgardt, 2017), which in turn has an impact on the mass profiles of our simulated clusters and the constrains from our models.

Figure 3.13 shows the cumulative mass profiles ($M(< r)$, left side panels) and mass-to-light ratios (Υ, right panels) for all five simulated GCs. The shaded area represents the models with $\Delta\chi^2 \leq 7.8$, while the black line represent the best fit model (for the

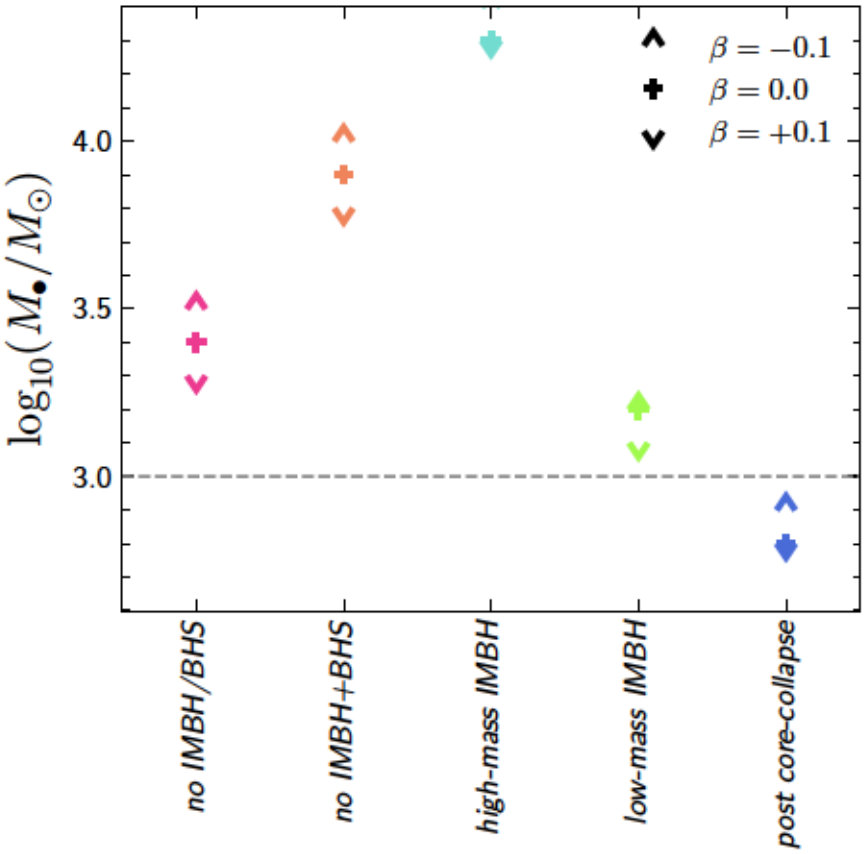

FIGURE 3.12: Upper limits of the $\chi^2 \leq 7.8$ region for the central IMBH mass given different velocity anisotropies for the full kinematic data case (LOS+PMs). The tangentially anisotropic case ($\beta = -0.1$, up-red arrow) gives systematically higher upper limits than the isotropic case ($\beta = 0.0$, black crosses) for the inferred mass of the IMBH. On the other hand the radial anisotropic case ($\beta = +0.1$, down-blue arrow) has systematically lower upper limits, as radial anisotropy can mimic an increase of velocity dispersion in the centre (mass-anisotropy degeneracy).

full kinematic sample, i.e. LOS+PMs as in Section 3.3.2.3); the symbols correspond to the measured values from each simulation. For the *no IMBH/BHS* and *no IMBH+BHS* simulations, the central mass of the GC is poorly constrained. The value of Υ_0 underestimates the central mass-to-light ratio of the cluster as shown in the right side panel of Figure 3.13. The dynamical model then requires additional mass to generate the observed velocity dispersion towards the centre, allowing for the presence of an IMBH. This effect is evident in the *no IMBH+BHS* case, as the cluster of stellar mass black holes increases drastically the mass-to-light ratio toward its centre. For this case the inferred mass of the central IMBH is $M_\bullet = 631^{+7312}_{-631}\, M_\odot$ when using the full kinematic sample. While no false central IMBH is detected, we cannot exclude it either, as the upper limit for such an inferred central IMBH is $M_\bullet < 7943\, M_\odot$. On the other hand, the presence of a central IMBH will quench mass segregation (see Gill et al., 2008a) and in turn change the shape of the mass-to-light ratio profile. This is the case of the *high-mass IMBH* simulation, where the central mass-to-light ratio is well represented

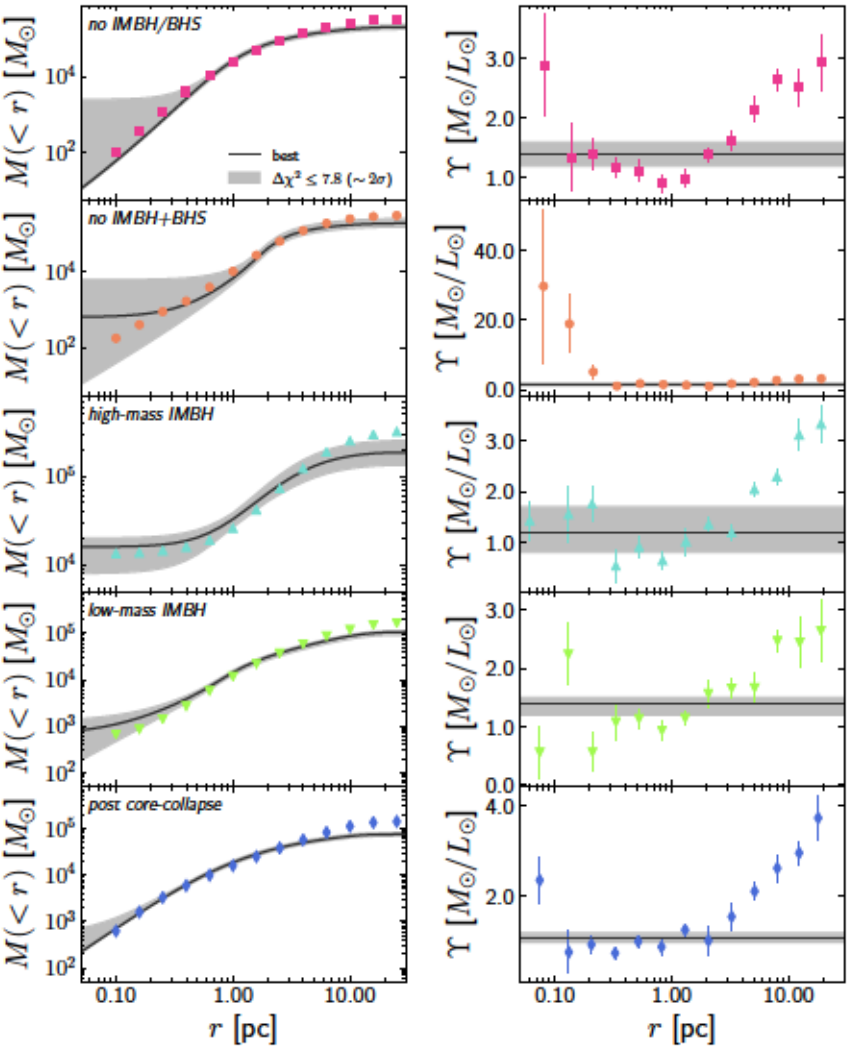

FIGURE 3.13: Mass profiles for all the simulated GCs. In the right column we include the cumulative mass profiles for each simulated GCs as coloured symbols. The black line represents the best-fit model, when all the velocity data are included in the fit. While the grey shaded area represents the $\Delta\chi^2 \leq 7.8$ region. The models tend to be less constrained towards the centre, in particular for the *no IMBH/BHS*, *no IMBH+BHS* and *low-mass IMBH cases*. The right panels show the mass-to-light ratio for each simulation. These profiles differ significantly from the assumption of a constant mass-to-light ratio. The case of the *no IMBH+BHS* simulation is quite extreme as the cluster of stellar-mass IMBH significantly increases the central values of the mass-to-light ratio profile. This is also shown in the cumulative mass profile, where it rises towards the centre instead of declining as in the *no IMBH/BHS* or *post core-collapse* simulations.

by the assumption of a constant mass-to-light ratio (see Figure 3.13).

The assumption of constant mass-to-light ratio is not only relevant for the central region of the simulated GCs. As massive particles sink towards the centre, the lighter ones populate the outer regions of the GC. This process also increases the mass-to-light ratio at larger radii, as faint low-mass stars dominate the exterior regions of the cluster. In panel (b) of Figure 3.11 we can see that all five simulated GCs have a similar increase in

their deprojected mass-to-light ratio profiles at larger radii. In the same way as for the centre of the cluster, our models underestimate the mass-to-light ratios and therefore the mass profiles (see Figure 3.13), which in turn could bias the estimates on the cluster mass. Panel (a) of Figure 3.14 shows the recovered enclosed mass within the deprojected half-light radius r_h from our dynamical models. For all five simulations our estimated mass within r_h is consistent with the mass measured directly from the simulation, our fitted values for Υ_0 are in agreement with the expected mass-to-light ratio within $r_{50\%}$ ($\Upsilon_{50\%}$, see Tables 3.3 and 3.2 respectively). However, this is not the case at larger radii; panel (b) in Figure 3.14 shows that for all simulated GCs their total masses are within 20% and 40% lower than the expected one. This is in agreement with other works: the effect of mass segregation on the recovering of global properties of GCs was discussed previously by Sollima et al. (2015), where they applied different modelling techniques from multi-mass distribution functions to N-body simulations of GCs. They show that single mass models systematically underestimate the total mass of the cluster, and found that the global parameters are well constrained within the radial range $r_h/2 < r < r_h$. In agreement with this, our models have a lower discrepancy on the recovered mass for radii close to r_h (see Figure A.4).

From the discussion above, one can infer that the assumption of a constant mass-to-light ratio has a larger impact on the constrains for the mass profiles, and in turn on the IMBH masses, than the assumption of constant velocity anisotropy. To characterize the real effect of these assumptions it is necessary to design a model which includes the variations on the mass-to-light ratio and velocity anisotropy profiles, which is beyond the scope of this paper.

3.5 Summary

The presence of IMBHs at the centre of galactic GCs is still an ongoing debate. Even with the diverse literature available on the topic (Noyola et al., 2008; van der Marel & Anderson, 2010; Lützgendorf et al., 2011; Kamann et al., 2014, 2016; Kızıltan et al., 2017, to name a few), a robust evidence is still missing. Limitations on the observations (such as kinematic centre and crowding, see Noyola et al., 2010; Lanzoni et al., 2013; de Vita et al., 2017) or in the modelling (due to anisotropy or a dark component, see van der Marel & Anderson, 2010; Zocchi et al., 2017, 2019; Mann et al., 2019; Baumgardt et al., 2019b) make the detection of IMBHs challenging. Here we explored the limitations of the dynamical model commonly used, namely models based on the Jeans equations. Using five Monte Carlo simulations of GCs with and without central IMBH from the MOCCA-survey (see Section 3.2.2), we have analyzed the reliability and limitations of spherically symmetric Jeans models (see Section 3.2.3) under the assumption of constant mass-to-light ratio and velocity anisotropy. We extracted a kinematic sample from the simulated GCs, excluding all binary systems and selecting stars brighter than 1 magnitude below

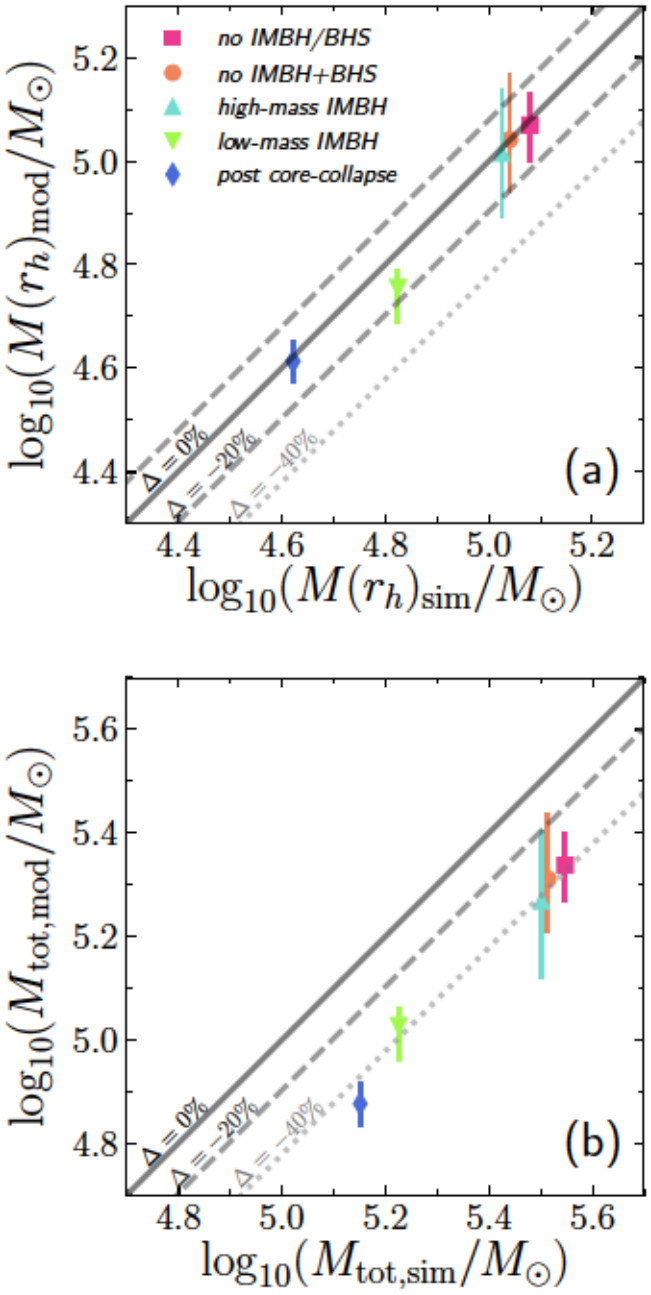

FIGURE 3.14: Recovered enclosed mass for the five simulated GCs. Panel (a): the mass within deprojected half-light radius r_h is recovered for all GCs (less than 20% error). On the other hand, in panel (b), the total mass of the simulated GCs is systematically underestimated.

the main sequence turn-off (see Section 3.3.1). We fit the Jeans models to the second velocity moment profiles, varying the mass-to-light ratio (Υ_0), the mass of the central IMBH ($M_\bullet$) and velocity anisotropy (β); we do so for only line-of-sight velocities (LOS, Section 3.3.2.1), only proper motion velocities (PMs, radial and tangential on the sky, see Section 3.3.2.2) and the full kinematic sample (i.e. LOS+PMs, in Section 3.3.2.3).

Our dynamical models can recover the mass of the high-mass IMBH ($M_\bullet/M_{GC} = 4.1\%$) quite well (see Section 3.3.2). The kinematic signature of such an IMBH is strong and the rise in velocity dispersion cannot be explained otherwise. On the other hand for the low-mass IMBH ($M_\bullet/M_{GC} = 0.3\%$) we can identify the central IMBH only within 1σ (i.e. $\Delta\chi^2 \leq 3.5$) level, and while the best fit model is consistent with the actual mass of the central IMBH ($M_\bullet = 519.3\,M_\odot$), models with no IMBH are possible within the errors (note that we only consider kinematic errors due to stochasticity of low numbers of stars per bin, observational errors could increase the uncertainty of the central IMBH mass). For all three simulations without a central IMBH we only get upper limits and while the no IMBH solution is within the range of masses, such upper limits allow for a possible IMBH in their centres.

The dynamical models are limited by two main assumptions: constant velocity anisotropy and constant mass-to-light ratio. Both have different consequences on the upper limits and detection of the central IMBH (see Section 3.4). Depending on the inferred amount of velocity anisotropy at the centre of the cluster, the dynamical model can slightly change the required IMBH mass to match the observed kinematics. This is relevant for identifying low-mass IMBHs. The upper limits for the inferred mass of the possible IMBH in NGC 5139 (van der Marel & Anderson, 2010) suggest a mass fraction of $M_\bullet/M_{GC} \leq 0.43\%$, which is close to our low-mass case ($M_\bullet/M_{GC} = 0.3\%$). While both, van der Marel & Anderson (2010) and Zocchi et al. (2017) find that anisotropic models are better when compared to the observed velocity dispersion of NGC 5139, the models by van der Marel & Anderson (2010) do not require a central IMBH to explain its observed kinematics. On the other hand, Zocchi et al. (2017) suggest strict upper limits, but do not rule out a central IMBH. Better understanding of the velocity anisotropy profiles and the effects of velocity errors on the analysis are necessary to fully disentangle the effects of anisotropy on the inferred mass of low-mass IMBHs. For the cases without an IMBH, we observe that anisotropy alone cannot reduce the upper limits as including the full kinematics sample (LOS+PMs) limits the range of anisotropy that the data allows (see Figure 3.12 and Section 3.4.1).

The assumption of constant mass-to-light ratio has a more significant impact on our analysis, as the mass-to-light ratio increases towards the centre and at larger radii (see panel (b) of Figure 3.11). For the cases without IMBH we underestimate the central mass due to mass segregation effects (i.e. rise in mass-to-light ratio), which allows the dynamical model to include a central IMBH to recover the observed velocity dispersion. This is even more relevant when the stellar black hole retention is higher, such as the

case of the model with a stellar black hole subsystem (*no IMBH+BHS*). By applying a multi-mass model which allows for a population of stellar mass black holes at the centre of NGC 5139, Zocchi et al. (2019) show that the population of black holes can reproduce the observed kinematic data, although it cannot discard completely a less massive IMBH. Using a different approach, Baumgardt et al. (2019b) also show that the presence of a cluster of stellar mass black holes can explain the observed kinematics of NGC 5139. In their case, they compare the observed kinematics to a library of N-body simulations, which intrinsically include a variable mass-to-light ratio.

The assumption of constant mass-to-light ratio not only limits our knowledge of the central mass of the GCs, but also its total mass. As two-body relaxation pushes outwards the faint low-mass stars, the mass-to-ligth ratio increases at large radii. We systematically underestimate the mass-to-light ratio in the cluster outskirts and therefore its total mass, as shown in Figure 3.14, is systematically underestimated with a difference of $\sim 40\%$ with respect to the expected mass for all simulated clusters. We are able to recover the mass enclosed within the half-light radius, which is consistent with the radial range proposed by Sollima et al. (2015) for estimating global properties of GCs with multi-mass distribution functions. Further improvements to our Jeans code are necessary to investigate if we can solve these issues by relaxing the constant mass-to-light ratio assumption.

GCs are collisional systems and their dynamical evolution is tied to the two-body relaxation process. Therefore, it is necessary to include the effects of collisionality in the dynamical models to be able to explain the observed kinematics, even more to robustly identify IMBHs at the centre of GCs. The results of applying our models to the *high-mass IMBH* ($M_\bullet/M_{GC} = 4.1\%$) suggest that there is a mass-fraction limit where the effects of collisionality can be excluded from the analysis, finding this limit requires further investigation beyond the scope of this paper. Ultimately, this will help to understand where we must improve the dynamical models. Most GC candidates for having an IMBH are in the low-mass range with $M_\bullet/M_{GC} \lesssim 1.0\%$ (van der Marel & Anderson, 2010), where the kinematic signature can also be explained by the effects of collisionality such as mass segregation, energy equipartition and a variable mass-to-light ratio. To be able to disentangle the different sources of a velocity dispersion rise in the centre of GC, models that can describe properly the mass profile of a GCs are a must. Recently, Hénault-Brunet et al. (2019b) provide a compilation of different dynamical methods and their reliability for recovering GC properties. Methods with multiple mass populations and variable mass-to-light ratio significantly improve the recovery of the mass profiles of GCs, although are still limited by observational constraints and large error bars.

While observational limitations will further complicate the detection of IMBHs in GCs, we have taken the first step in better understanding the ability to recover an IMBH from data with models based on the Jeans equation. The limitations presented here are identical for any such model under the same assumptions, not just ours. While

the dynamical models studied here do not lead towards a biased solution, they lack the sensitivity to robustly infer the presence or absence of a low-mass IMBH. Improving a model's ability to recover the mass profiles of GCs, and further understanding how the constant mass-to-light and velocity anisotropy assumptions along with the observed kinematics influence a model is crucial towards robustly identifying or rule out the presence of IMBHs in galactic GCs. We will further address observational challenges such as binaries in a subsequent paper.

Chapter 4

Using Binaries in Globular Clusters to Catch Sight of Intermediate-Mass Black Holes

This chapter has been submitted for publication to Monthly Notices of the Royal Astronomical Society under the title "Using Binaries in Globular Clusters to Catch Sight of Intermediate-Mass Black Holes" by ***F.I. Aros****, A. C. Sippel, A. Mastrobuono-Battisti, P. Bianchini, A. Askar and G. van de Ven.*

4.1 Introduction

Intermediate-mass black holes (IMBHs) with masses of $10^2 - 10^5\,M_\odot$ are one of the missing links in the formation and growth of the supermassive black holes found at the centre of massive galaxies; the early formation of IMBHs can serve as seeds capable of growing up to the masses of supermassive black holes supporting the quasars observed at high-redshift (Haiman, 2013). The possible formation scenarios of IMBHs (Portegies Zwart et al., 2004; Giersz et al., 2015; González et al., 2021; Rizzuto et al., 2021) point to dense stellar systems as their place of origin and therefore many studies have searched for IMBHs in the centres of globular clusters.

Globular clusters (GCs) are dense stellar systems with up to a few million stars and half-light radii of 2-5 pc (Harris, 1996, 2010 edition). In the last two decades, many studies have looked at the centres of Galactic GCs to search for kinematic evidence for the presence of an IMBH (Noyola et al., 2008; van der Marel & Anderson, 2010; McNamara et al., 2012; Lützgendorf et al., 2013a; Lanzoni et al., 2013; Kamann et al., 2014, to name a few). However, limitations on the observed kinematics (de Vita et al., 2017) and dynamical modelling (Aros et al., 2020) may hinder the robust detection of an

IMBH. No clear evidence for an IMBH has been found so far within Galactic GCs. The possible presence of a black hole system (BHS, see Section 4.4) in the cluster centre that add to this complex scenario, as it can produce similar velocity dispersions in the cluster core as a central IMBH (Zocchi et al., 2019; Baumgardt et al., 2019b; Mann et al., 2019; Vitral & Mamon, 2021).

Binary stars play a crucial role in the evolution of GCs. The dynamical evolution of GCs is driven by two-body relaxation that triggers mass segregation (Spitzer, 1987). Binaries, being more massive than single stars (two stars instead of one), segregate earlier to the cluster centre. Simulations of GCs with primordial binaries (Heggie et al., 2006; Hurley et al., 2007; Chatterjee et al., 2010; Wang et al., 2016) show how binaries segregate towards the cluster centre while becoming harder or getting disrupted by encounters with other stars in the dense core. These two processes provide energy to the cluster and play a significant role during the core-collapse period of the GCs' evolution.

Observations of binaries in Galactic GCs show that binaries follow the behaviour described in simulations. Measurements of the binary fraction at different radii show a decreasing gradient with radius (see Sollima et al., 2007; Milone et al., 2012a; Ji & Bregman, 2015) and serve as proof for the mass segregation of binaries in GCs. The connection between binaries and the dynamical evolution of the GC has also been explored with specific types of binaries and products of binary evolution. Ferraro et al. (2012, 2018) used the distribution of blue-straggler stars (BSS) to study the dynamical age of GCs. As formation channels of BSS include binary interactions (Mapelli et al., 2006; Chatterjee et al., 2013), the tracing of BSS stars is linked to the overall process of mass segregation. In a similar way, the distribution of X-ray binaries in GCs also describes the same process (Cheng et al., 2019a,b). The mass segregation driven by two body relaxation not only brings binary systems closer to the cluster centre, but it also efficiently accumulates more massive stars and massive stellar remnant such as stellar mass black holes.

A massive object in the cluster centre such as an IMBH will alter the dynamical evolution of the GC. The IMBH hampers mass segregation by working as a source of energy for the cluster (Baumgardt et al., 2004; Trenti et al., 2007b; Gill et al., 2008b) and in the process altering the distribution of binaries within the cluster core. Moreover, simulations of GCs with a central IMBH and primordial binaries show that binaries in the core are disrupted more efficiently than in the case without an IMBH (Trenti et al., 2007b). Whereas this is more likely to happen due to the high density of stars near the IMBH, some binaries could strongly interact with the IMBH. The strong interaction with the IMBH breaks the binary producing high-velocity stars (see Hills, 1988; Fragione & Gualandris, 2019; Šubr et al., 2019, for example).

In this work, we study the effects that the presence of an IMBH has on the binary population of its host GC. Motivated by the recent observations of binaries in NGC 3201

with VLT/MUSE by Giesers et al. (2019), we use a sample of simulated GCs from the MOCCA-Survey database I (Askar et al., 2017) with two goals: (1) explore the contamination of binaries in the line-of-sight velocity dispersion and (2) to use the detected binary sample to study the binary fraction in GCs with and without an IMBH. The first point is effectively extending the discussion of Figure 4 in Aros et al. (2020) where we show that binaries can systematically increase the observed line-of-sight velocity dispersion.

In Section 4.2 we describe the sample of simulated GCs and the detection method for binary stars. In Section 4.3 we explore the contamination of binaries in the observed line-of-sight velocity dispersion and its implication for current observations. In Section 4.4 we analyze the relation of binaries with the central IMBH and discuss how we could use their co-evolution as an indication for the presence of an IMBH. Finally, in Section 4.5 we summarize our findings and motivate future work.

4.2 Simulations and binary identification

The dynamical evolution of GCs is determined by two-body interactions leading towards partial energy equipartition (see e.g. Spitzer, 1969; Trenti & van der Marel, 2013; Bianchini et al., 2016a). A consequence of the drive towards energy equipartition is mass segregation, where more massive stars sink towards the centre of the GC. Binaries being on average more massive than single stars (two stars instead of one) segregate faster to the centre, ultimately increasing the binary fraction towards the cluster core. To study the general behaviour of binaries under the presence of an IMBH, we identify binaries in mock data from simulated GCs as described in the following sections.

4.2.1 Simulations and mock data

We have selected a sample of 143 simulated GCs from the MOCCA-Survey Database I (Askar et al., 2017) to study the effects of binaries in the observed kinematics and the interaction of binaries with a central IMBH. These simulations were evolved to 12 Gyr using the MOCCA code (Hypki & Giersz, 2013; Giersz et al., 2013), which follows a state-of-the-art implementation of the Monte Carlo method first proposed by Hénon (1971b,a). All 143 simulations have different initial conditions, but share the same initial binary fraction $f_{\rm bin} = 10\%$,consistent with observations (Sollima et al., 2007).

As described in detail by Giersz et al. (2015), IMBHs in MOCCA simulations form via dynamical interactions in two kinds of scenarios. The "FAST" scenario starts from the beginning of the simulation and requires an extremely high initial density ($\gtrsim 10^6\,M_\odot/{\rm pc}^3$, see also Hong et al., 2020), where a BH system can form early in the star cluster evolution and drive the formation of an IMBH by the dynamical interactions of single and binary BHs (similar to the runaway collapse proposed by Portegies Zwart et al., 2004).

The "SLOW" scenario, on the other hand, happens at later stages in the cluster evolution and in less dense systems ($10^5\,M_\odot/\mathrm{pc}^3$). The mass of a single BH can grow through dynamical interactions and mass accretion from a binary companion.

The binary-star evolution code (`BSE`, Hurley et al., 2002) models the binary stellar evolution in `MOCCA`, while the `FEWBODY` code (Fregeau et al., 2004) drives the dynamical interactions of binaries with single or binaries stars. The interplay of both codes allows `MOCCA` to follow the evolution of binary stars in a realistic way, while also keeping short simulation times. Hypki & Giersz (2013) describes the interplay of both codes within `MOCCA` extensively.

`MOCCA` simulations are spherically symmetric and only have three coordinates for each star: the radial position r, and the radial v_r and tangential v_t velocies. Therefore, we project each simulated GC into cartesian coordinates by randomly sampling the missing coordinates. We then project the simulated GC into the sky to get the position of each single and binary star, along with their radial velocity (RV) along the line-of-sight and the proper motions. We follow the same projection as in Aros et al. (2020).

For every binary system in the cluster, we obtain each component's relative velocity with respect to their centre of mass, drawing the orbit from the known eccentricity, semi-major axis and masses of each star in the binary. From these orbital parameters, we can obtain the individual positions and velocities of both components of the binary, the period and angular momentum. We randomly select the current position of the binary by selecting a fraction of the orbital period. In the same way, we randomly orientate the binary's orbital plane. Whereas this approach is similar to the projection described by Askar et al. (2018a), we use the direct solution of the Kepler orbit rather than the parameterization of the orbit using the eccentric anomaly.

We generate mock data for each cluster by adding errors to the velocities that are consistent with current observations. For line-of-sight radial velocities, we use the error distribution by magnitude from MUSE data (Giesers et al., 2019), with a median value of 3 km/s at $m_\mathrm{V} \sim 18$ mag at a distance of ~ 5 kpc (see Figure B.1). For proper motions, we assume the median error from Libralato et al. (2018), which is 0.1 mas/yr, which corresponds to 2 km/s at 5 kpc (see also Appendix B.1). In both cases, we add noise to the simulation's velocities by sampling the noise from a Gaussian distribution centred in zero with a dispersion given by the assigned error. Whereas we have assumed that all the clusters are at a distance of 5 kpc to have a comparable sample of stellar masses and observed stars, the simulated clusters have different Galactocentric distances ranging within $1 - 15$ kpc.

We have limited the "observed" stars within each cluster to those with line-of-sight RV errors smaller than 3km/s. This set a lower limit in magnitude around 1 mag below the main-sequence-turn-off (or ~ 18 mag), similar as used by Aros et al. (2020). From the sample of 143 simulated GCs in the `MOCCA`-Survey database I with an initial binary

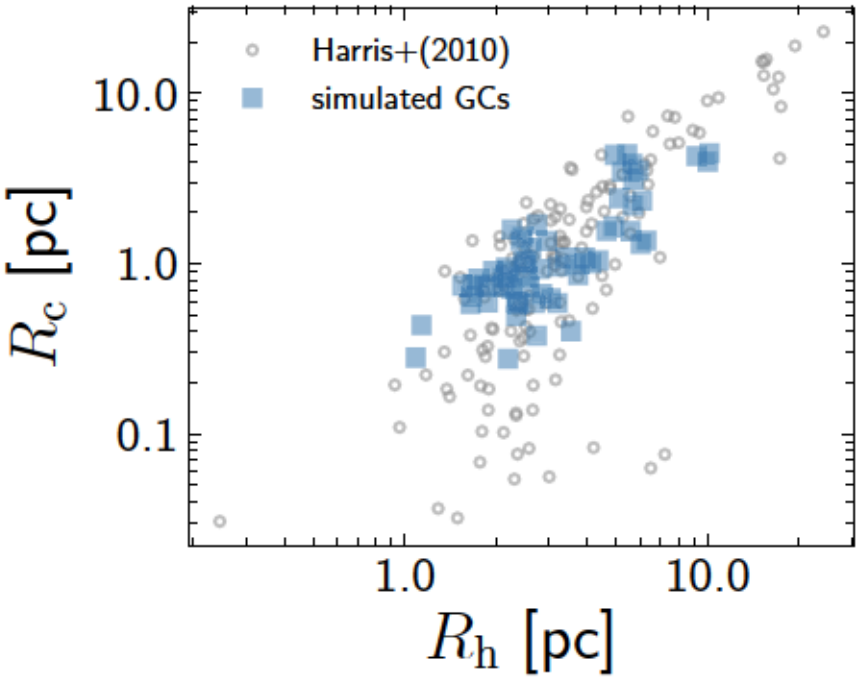

FIGURE 4.1: Core R_c and half-light R_h radii for simulated GCs. We have selected a sample of 65 simulated GCs with and without a central IMBH, with initial binary fraction of 10% (light-blue squares) and additional requirements on the quality of the data as described by Section 4.2.1. As a reference we show Galactic GCs from Harris (1996) (2010 edition). Our selected sample has comparable sizes as real GCs.

fraction of 10%, we selected a subsample of clusters that have: (a) more than 1000 stellar systems (binary and single) within the selected sample of bright stars, and (b) their intrinsic velocity dispersion is higher than 4 km/s, which is twice the median velocity error in line-of-sight velocities and proper motions at the assumed distance of 5 kpc. These two criteria help to reduce the stochasticity due to low numbers (binary fraction), and to measure velocity dispersion values that are not dominated by observational errors. Our sample then decreases to 65 GCs.

In the following sections of this work, we refer to the projected core (R_c) and half-light radii (R_h) of each cluster. Both radii are extracted from Arca Sedda et al. (2019), who fitted a King profile (King, 1962) to the cumulative surface brightness profile, following the method described by Morscher et al. (2015). Figure 4.1 shows the core and half-light radii for the subsample of 65 simulated GCs and for Galactic GCs from Harris (1996) (2010 edition). The sizes of our selected sample are comparable to observed GCs.

4.2.2 Identification of binaries

We identify binaries in the mock data by measuring the observed RV for each star at different observational epochs, i.e. different observations with time scales of hours,

weeks or months[1]. We do not evolve the simulations between epochs; therefore, the positions and velocities of single stars, and the centre of mass position and velocity of binary stars remain fixed[2]. Any variation on the RV of single stars is only due to observational errors. For binary stars, while the center of mass remains fixed, we update the position and velocities of both component at each epoch. We use the orbital parameters and subsequent orbit to follow the binary components relative positions and velocities around the binary centre of mass. The "observed" RV for the binary star is given then by the luminosity weighted velocity along the line of sight:

$$\mathrm{v_{los}} = \mathrm{v_{cm}} + \frac{\mathrm{v}_1 L_1 + \mathrm{v}_2 L_2}{L_1 + L_2}\,, \tag{4.1}$$

where $\mathrm{v_{cm}}$ is the centre of mass velocity of the binary, and v_i and L_i are the velocity and luminosity of each component.

Once we calculate the RVs for all epochs for single and binary stars in the simulated cluster, we proceed to assign a probability of variability. To do so, we follow the approach of Giesers et al. (2019), described in the following. The probability of variability is defined by analysing the RV curve and the scatter around the mean velocity for all epochs. For each star with n different epochs, the scatter in RV can be described by

$$\chi^2_{\mathrm{obs}} = \sum_{i=0}^{n} \frac{(\mathrm{v}_i - \overline{\mathrm{v}})^2}{\delta \mathrm{v}_i^2} \tag{4.2}$$

In a GC with only single stars, the scatter is dominated by errors only, and the distribution of observed χ^2 resembles a theoretical χ^2 distribution with $\nu = n - 1$ degrees of freedom. Variability due to the motion of binaries would show as an extended tail in the observed χ^2 distribution or a change in the slope of the cumulative distribution, as the scatter will be dominated by the orbital motions rather than observational errors.

Using this idea, Giesers et al. (2019) define the probability of a star to have a variable RV as

$$P(\chi^2_i, \nu_i) = \frac{F(\chi^2_i, \nu_i)_{\mathrm{theo}} - F(\chi^2_i, \nu_i)_{\mathrm{obs}}}{1 - F(\chi^2_i, \nu_i)_{\mathrm{obs}}}\,, \tag{4.3}$$

where $F(\chi^2_i, \nu_i)$ is the cumulative χ^2 distribution given ν_i degrees of freedom, evaluated at the measured χ^2 value of the i-th star. In our case, we use the same number of epochs for each star and cluster, a version which considers a different number of epochs is described in Giesers et al. (2019). In the case of the simulated clusters, we can link the probability of variable RV to a being a binary star, as no other effect could produce the same signature; therefore, we will use $P_{\mathrm{bin}} = P(\chi^2_i, \nu_i)$.

[1] We use 19 epochs given by $t_{\mathrm{epoch}} = [0, 6, 15, 24, 33, 360, 375, 384, 384.03, 384.06, 384.09, 384.12, 384.15, 384.93, 384.96, 384.99, 385.02, 385.05, 393]$ days.

[2] Stars would not significantly move in this time range since it is much lower than the dynamical time.

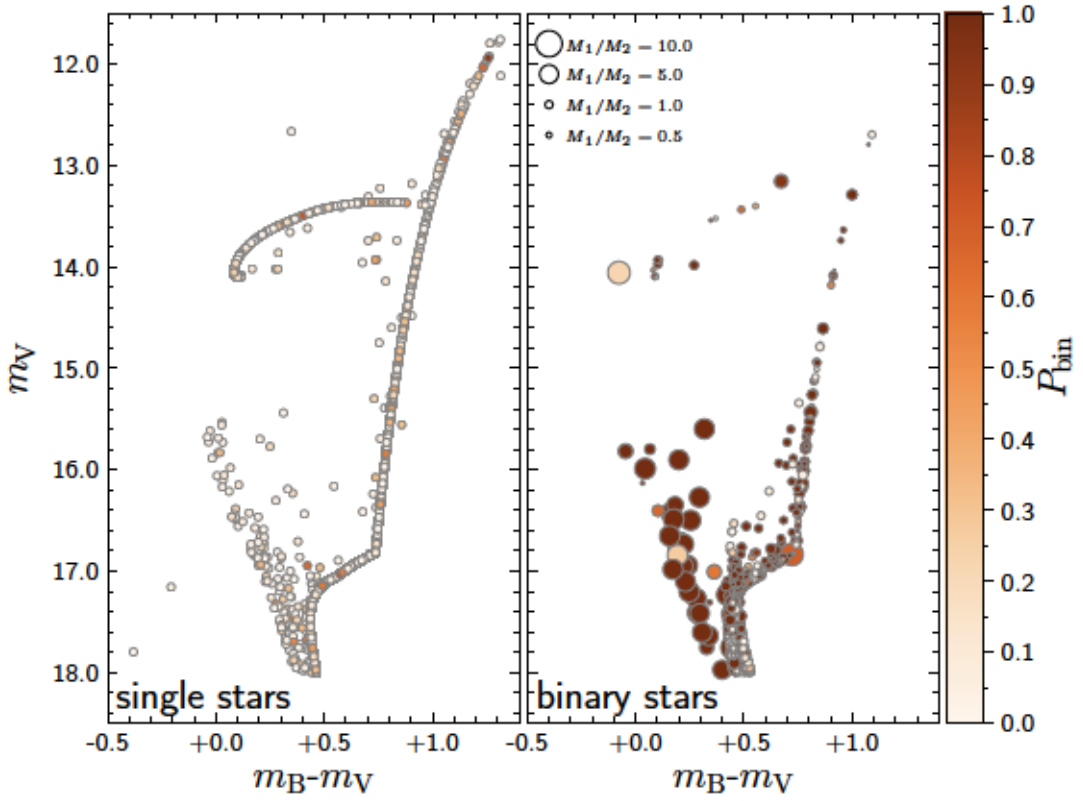

FIGURE 4.2: Color-magnitude diagram for single (left panel) and binary (right panel) stars in a simulated GC at 12 Gyr. The points are colour coded by the probability of being a binary with lighter colours corresponding to single stars. We can see in the left panel that most single stars have a low probability for being a binary. On the other hand, in the right panel not all binaries are identified, this is due either to having long periods or very face-on orbital planes. The size of the symbols on the right panel indicates the mass ratio between the binary components. We do not observe any particular trend with magnitude for the binary detectability. Binaries in the blue-stragglers branch are likely to be detected (close binaries).

Figure 4.2 shows the colour-magnitude diagram for a simulated GC with a binary fraction of $f_{\rm bin} = 7.8\%$ at 12 Gyr. Each star is colour coded by its probability of being variable in RV given by $P_{\rm bin}$. The left panel shows all single stars in our luminosity selection, the large majority of single stars have a low probability of being variable in RV and are unlikely to be binaries. On the right panel of Figure 4.2, we show all binaries in the simulated cluster also colour coded by their probability of being variable in RV, the sizes of the symbols represent the mass ratio between components. While many binaries have indeed a high probability of being variable in RV, a significant fraction does not and therefore are not identified as binaries. If the velocity amplitude of the binary in the RV curve is not large enough, it will not show as having a high scatter in χ^2 and will be assigned a low probability of variability in RV.

Three main effects play against the detection of binaries using this approach. The first

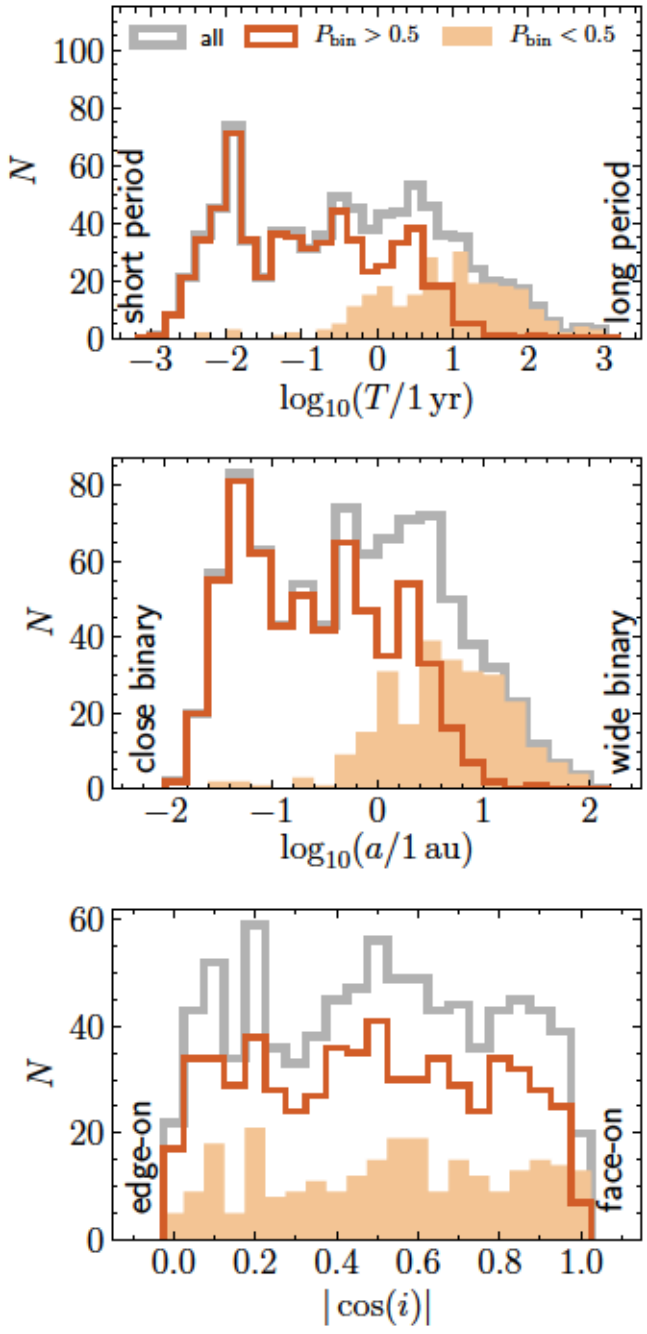

FIGURE 4.3: Period, semi-major axis and orbital plane inclination for all binaries in a simulated GC (the same as the cluster in Figure 4.2). Binaries that have short periods (top panel) and that have a small semi-major axis (middle panel), i.e. hard binaries, are robustly detected with variations in RVs, as the frequency and amplitude of such variations are higher. The inclination (bottom panel), on the other hand, adds a complexity as it limits the detection for any type of binary. As expected, we can see that binaries which are close to edge-on are more easily detected than the ones at face-on.

one is the luminosity ratio between the components. If both stars have similar luminosities, then the observed line-of-sight velocity given by Equation 4.1 will be dominated by the centre of mass velocity rather than for their orbital motion. In the right panel of Figure 4.2, we can see than many of the binaries with a low probability of variable RV have similar masses ($M_1/M_2 \sim 1$). While the mass ratio affects the orbital parameters, it also serves as a proxy for the luminosity ratio of binaries.

The second effect comes from the orbital parameters of the binary, which also have a role in their detection. In Figure 4.3 we ilustrate a selection of orbital parameters that have an impact on the probability of being variable in RV, and therefore on identifying binaries. We see that most of the binaries with a high probability $P_{\rm bin} > 0.5$ of being variable in RV have short periods and are close binaries, as shown in the top two panels of Figure 4.3. Short period binaries orbit faster around their centre of mass, increasing the amplitude of the variability in RV. All of the binaries detected in this simulated GC have periods below 1 yr. The length of the semi-major axis a goes in hand with the period, as binaries which survive sinking to the centre of the cluster become tighter and have shorter periods.

The third effect on the detectability of binaries comes from the inclination of the orbital plane. The orientation of the orbital plane is randomly chosen, therefore it is not directly related to other orbital parameters of the binaries. In the bottom panel of Figure 4.3, all binaries in the sample have an inclination angle i which follows a uniform distribution (over a sphere and therefore is uniform in $\cos(i)$). We can see that for a significant range of inclinations, most of the binaries have a high probability of being variables in RV ($P_{\rm bin} > 0.5$). However, this changes once the orbital plane becomes closer to be face-on, where the undetected binaries dominate the sample. This is expected as when the orbital plane becomes face-on, the line-of-sight velocity will be perpendicular to the orbital motion of the binary.

Using this approach we can identify binaries in each mock data set, corresponding to each simulated globular cluster. In the following sections, we will discuss the effects of the binaries on the kinematics of a cluster (Section 4.3) and their interaction with an IMBH (Section 4.4).

4.3 Kinematic effects of binaries

As we previously discussed in Aros et al. (2020), binaries have two main effects on the observed velocity dispersion of GCs. First, as binaries are more massive than single stars, they have, as a population, a different level of energy equipartition and hence spacial distribution. As this affects the centre of mass velocities of the binaries, both the line-of-sight velocity and the proper motions will show a lower velocity dispersion than what is expected for a cluster populated by single stars only. This effect has been studied for

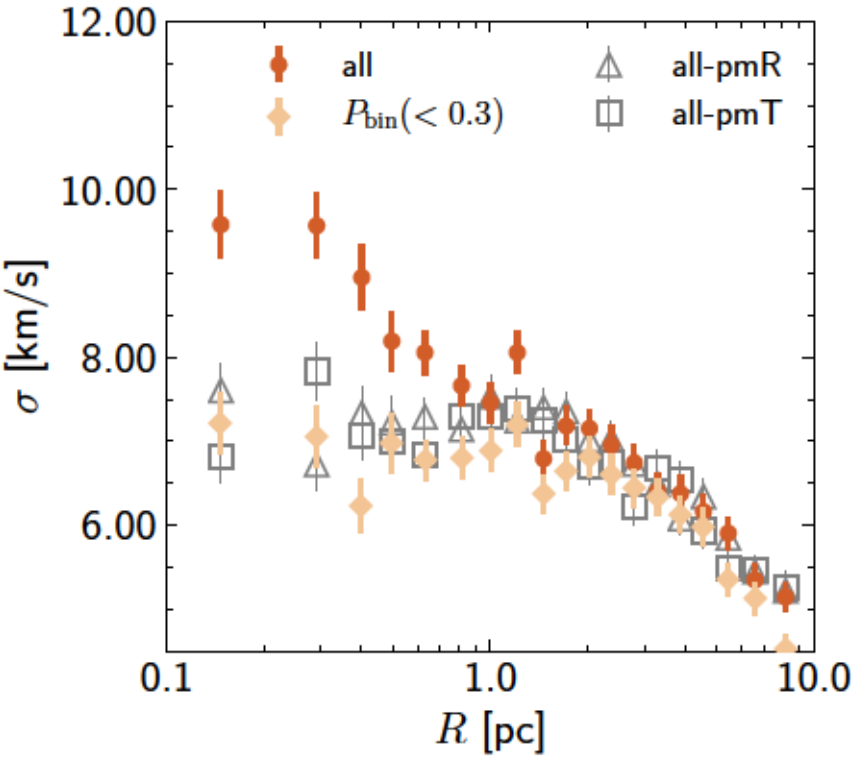

FIGURE 4.4: Line-of-sight velocity dispersion for a simulated GC with binaries (same cluster as in Figures 4.2 and 4.3). The dark-orange circles shows the velocity dispersion when all stars are considered for the kinematics, this includes all binaries in the sample. Once we use the probability of being a binary assigned to each star, we can select stars that have a low probability $P_{\rm bin} < 0.3$. The light-orange diamonds show the velocity dispersion profile when most binaries are excluded. We can see that once the sample is "cleaned" from binaries, the line-of-sight velocity dispersion is consistent with the proper motion velocity dispersion (gray triangles and squares).

proper motions by Bianchini et al. (2016b), while they find that in simulations there is a colour bias in the velocity dispersion due to the presence of binaries, i.e. the redder edge of the main sequence (binary stars) has a lower velocity dispersion than the blue edge (single stars). However, they do not detect this on HST observations for NGC 7078. In general, it is challenging to disentangle this effect, as it depends on the binary fraction and level of energy equipartition in the cluster.

Figure 4.4 shows the observed velocity dispersion for the same cluster used as in Figure 4.2 and 4.3. The dark orange circles show the line-of-sight velocity dispersion for all stars in the sample (single+binaries), while the ligh orange diamonds show the velocity dispersion when only stars with $P_{\rm bin} < 0.3$ (i.e. with a low probability of being variables and therefore mostly singles) are selected. The difference between the whole sample and the selection with $P_{\rm bin} < 0.3$ is a consequence of the scatter introduced by the orbital motion of binaries. For comparison, the radial (grey triangles) and tangential (grey squares) proper motions are also included. Both proper motions behave similarly to the sample with $P_{\rm bin} < 0.3$.

While the previous example comes from mock data of a simulated globular cluster, it is also possible to observe this effect in current observations of GCs. Using multi-epoch observations of VLT/MUSE data, Giesers et al. (2019) identified binaries in NGC 3201 using the variations in radial velocity (RV). We use the available RV data from their work to analyse the kinematic effect of the binaries in their sample. Figure 4.5 shows the line-of-sight velocity dispersion for the sample in Giesers et al. (2019), with the same approach as in Figure 4.4 we show the velocity dispersion for all stars (red circles) for and a sample of the stars with a probability of being variable in RV of $P_{\rm bin} < 0.3$ (blue squares). Each data point is calculated from approximately 150 stars for the two epochs that have the large sample of observations (~ 3000 stars, upper and lower panel). Note that we only select stars with velocity errors smaller than 3 km/s.

From Figure 4.5, we can see that for both epochs the sample with $P_{\rm bin} < 0.3$ indeed has a lower velocity dispersion and the difference increases towards the centre. For reference, we have also included previous measurements of the line-of-sight velocity dispersion from Kamann et al. (2018) who use VLT/MUSE data and from Baumgardt & Hilker (2018) for which their radial velocities come from RAVE (Kunder et al., 2017). It is important to highlight that the data from Giesers et al. (2019) are an extension of the data of Kamann et al. (2018), which increases the number of average epochs from 7 to 12. Kamann et al. (2018) already discussed the differences between their velocity dispersion profile and the one from Baumgardt & Hilker (2018), pointing to two probable sources, binaries or energy equipartition. For binaries, they excluded stars which were likely to be binaries based on RV variations between epochs, however, the additional epochs in Giesers et al. (2019) might have helped in detecting binaries which reminded undetected by Kamann et al. (2018), in particular short-period binaries.

The different effects of binaries in line-of-sight velocities and proper motions can help as a pointer of the level of contamination by binaries and the binary fraction of the cluster. If, as in Figure 4.4, a significant difference in the velocity dispersion between single epoch line-of-sight observations and proper motions is observed, then follow up line-of-sight velocity observations will be necessary to identify binaries and to clean up the kinematics. In other words, cleaning up the kinematics would be crucial for a 3D kinematic analysis of the cluster.

4.4 Binary fraction and IMBHs

As discussed in the previous section, binaries leave a clear signature on the observed velocity dispersion. Dynamical analysis that considers line-of-sight velocities needs to take into account their presence. While it is possible to clean the kinematic sample by multi-epoch observations, the identified binaries can also be used to help understand the dynamical state of a GC.

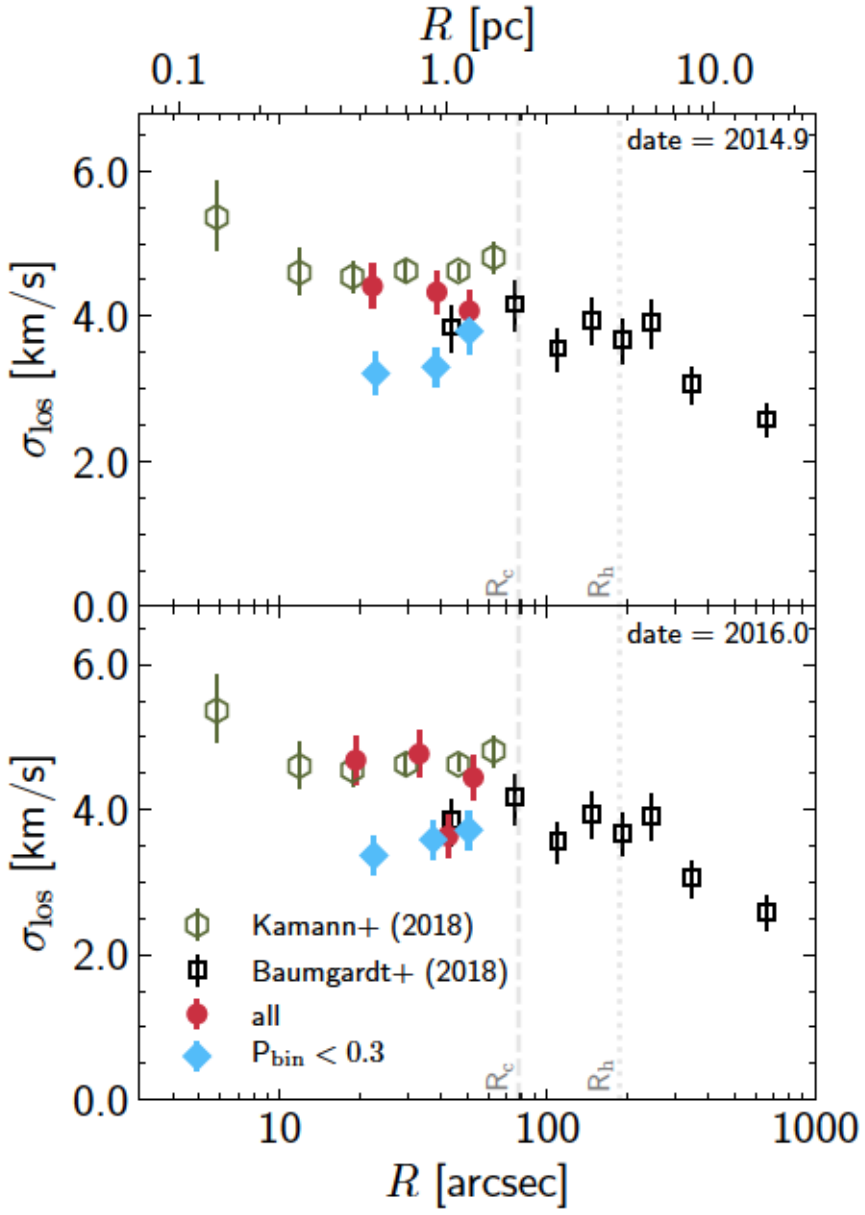

FIGURE 4.5: Line-of-sight velocity dispersion for NGC 3201. We include the data from Kamann et al. (2018) (green hexagons) and Baumgardt & Hilker (2018) (black squares), as well as the observations from Giesers et al. (2019) (red circles) in two different epochs (top and bottom panel). Once we exclude stars that have a high probability of being a binary (blue diamonds) we observe a drop in the velocity dispersion similar as in Figure 4.4. This is consistent for both epochs and shows the importance of multi-epoch observations to detected binaries in GCs. The Figure also shows the core and half-light radii of NGC 3201 from Harris (1996) (2010 edition).

4.4.1 Radial distribution of binaries

The binary distribution changes during the dynamical evolution of a GC, mainly as they segregate towards the cluster's centre and the formation and destruction of binaries by their interaction with surrounding stars. Consequently, the cluster's binary fraction increases towards the centre while decreasing at larger radii (see Figure 4.6). Early N-body simulations of GCs with binaries by Heggie et al. (2006) already show how the half-mass radius of the binary population is indeed smaller that of single stars.

The presence of a central IMBH affects particularly the surviving fraction of binaries in the cluster centre, as the rate of disrupted binaries increases significantly under the presence of a central IMBH. While the increased density of stars around the IMBH mainly drives the disruption of binaries that segregate towards the cluster centre by interactions with other stars (Trenti et al., 2007b), close encounters of a binary with the IMBH can also break the binary producing high-velocity stars (see Hills, 1988; Fragione & Gualandris, 2019; Šubr et al., 2019, for example). This implies that clusters with a central IMBH have a reduced binary fraction towards the centre of the cluster.

Using the detected binaries in the sample of simulated GCs, we have constructed binary fraction profiles to analyse the behaviour of GCs with and without IMBH. The top panel of Figure 4.6 shows the binary fraction profiles of our sample of 65 simulated GCs, and each profile is colour-coded by the most massive object in the cluster (from a star of $1\,M_\odot$ in dark blue to an IMBH of $10^4\,M_\odot$ in red).In clusters without an IMBH, the most massive object is in most cases a stellar mass black hole with on average $\sim 20\,M_\odot$. While all clusters started with the same fraction of 10% for primordial binaries, we can observe a large variety of radial distributions. However, a significant difference is the presence of an IMBH, as clusters with one clearly show a lower binary fraction at all radii as well as a flatter profile. To have more clarity in the differences of both populations of GCs (with and without IMBH), we show in the bottom panel of Figure 4.6 the median profile for each population. We find that median distribution are well represented by a power-law ($f_{\rm bin} \propto (R/R_{\rm h})^{-k}$), and that clusters without an IMBH have a steeper profile ($k = 0.34$) compared to those with one ($k = 0.19$).

An alternative way to observe the binary fraction profile behaviour is to focus on specific regions of the GCs. From Figure 4.6, we can see that the binary fraction at the centre and around the half-light radius matches more on clusters with an IMBH than for GCs without one. We now focus only on those two regions and measured the binary fraction within the GC's core radius and the area within one and two half-light radii. Figure 4.7 shows the binary fractions for all clusters in our sample, once again colour-coded by the most massive object in the GC. We can see that GCs with a central IMBH (in red) have a lower binary fraction and populate the figure's bottom-left region; furthermore, most of these clusters are close to the 1-to-1 relation (dashed line). Clusters without an IMBH have a higher binary fraction, particularly in the core, and move away from the

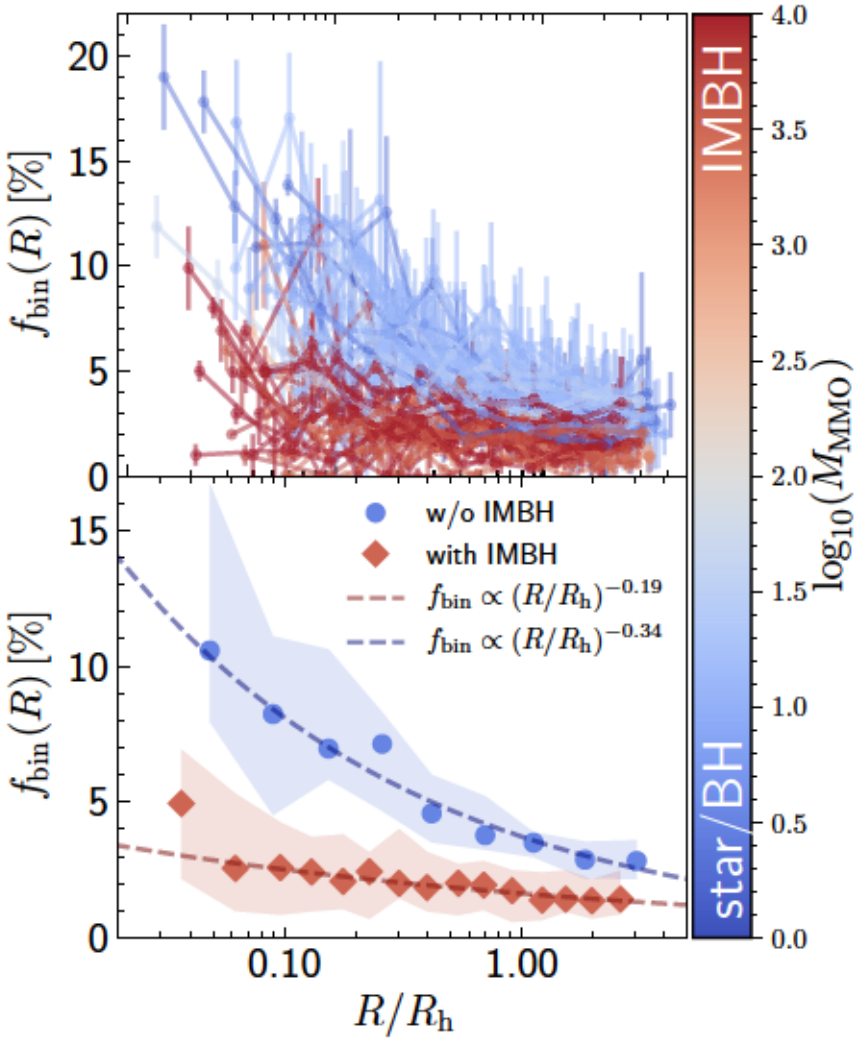

FIGURE 4.6: Radial distribution of binaries. The top panel shows the binary fraction $f_{\rm bin}$ profile for each simulated GC in our sample, colour-coded by the mass of the most massive object (stars in dark blue and IMBHs in red). The symbols mark the binary fraction using $P_{\rm bin} = 0.5$ as a delimitter for binaries and non-binaries (i.e. stars with $P_{\rm bin} > 0.5$ are binaries, while stars with $P_{\rm bin} < 0.5$ are single stars); the error bars represent the binary fraction by separating binary and non-binary stars at $P_{\rm bin} = 0.3$ (top error bar) and $P_{\rm bin} = 0.7$ (bottom error bar). The bottom panel shows the median binary fraction profile for both types of GCs, with and without and IMBH. We fitted a power-law to the median distributions (dashed lines) and show that clusters with an IMBH have a flatter profile and a lower binary fraction than GCs without one.

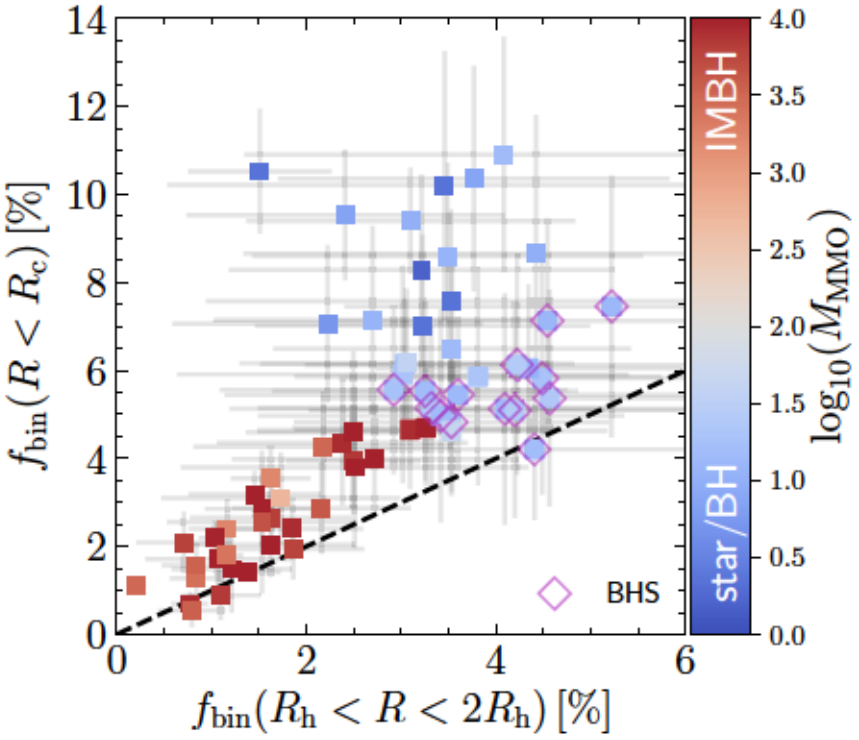

FIGURE 4.7: Binary fractions around half-light radius $R_{\rm h}$ and within the core radius $R_{\rm c}$. Each GC is colour-coded by its most massive object. Clusters with an IMBH stay near the dashed line showing the 1-to-1 ratio between the binary fractions, i.e. less mass segregated than above the line. These clusters also populate the left side of the figure as they have systematically fewer binaries, a difference with respect to GCs with a BHS (magenta diamonds) that are near the 1-to-1 line, but have retained more binaries overall.

1-to-1 line, which shows the expected effects and consequences of mass segregation in the binary population. On average, clusters with an IMBH have 67% fewer binaries in their core than cluster without one. A group of GCs without an IMBH is also located close to the 1-to-1 line. These clusters have retained many stellar-mass black holes instead of an IMBH, and to identify them, we have marked with a magenta diamond all GC with more than 50 stellar remnant black holes (i.e. a black hole system, BHS) within the half-mass radius. While they are closer to the 1-to-1 line with respect to clusters without a BHS, they still have a higher binary fraction within the core than clusters with an IMBH. On the other hand, they have a lower binary fraction than GCs without so many central black holes or an IMBH. Whereas the BHS works as an energy source for the cluster to halt mass segregation, the density within the core is not high enough to trigger an efficient disruption of binaries (see e.g. Mackey et al., 2008; Sippel & Hurley, 2013; Breen & Heggie, 2013b; Morscher et al., 2015; Weatherford et al., 2018).

The advantage of using integrated quantities over different regions of the cluster is that we can explore the behaviour of observed GCs. Milone et al. (2012a) surveyed the binary fraction of GCs using HST photometry along the main sequence. While there

are intrinsic differences in the detected binaries from their method and the one described here, this is a first-order approach to show that it is possible to test our results with photometric data. Figure 4.8 shows the binary fraction within the core radius and the region outside the half-mass radius, as given by Milone et al. (2012a). We see that almost all clusters are near or above the 1-to-1 relation (dashed line). Only NGC 288 falls clearly below the 1-to-1 line. While the error bars are big enough to include the 1-to-1 line, it is essential to keep in mind that this cluster has tidal tails (see Kaderali et al., 2019; Sollima, 2020, for the latest discussion using Gaia data) and could have a more complex dynamical evolution than other clusters in the sample. We compared the clusters in Milone et al. (2012a) sample with two studies that estimate the number of remaining stellar mass black holes (BHs): Askar et al. (2018b) (red diamonds) use properties such as the core radius and the central density to estimate the number of retained BHs, whereas Weatherford et al. (2020) (green squares) use the mass segregation of the clusters as an indicator for the remaining BHs. Although both studies estimate different numbers of BHs (see Table B.1 in the Appendix), the clusters with retained BHs are near the 1-to-1 line. Most clusters with candidate IMBHs do not have measured binary fraction within the core and have been excluded from Figure 4.8.

4.4.2 Kinematic effects due to binaries

We discussed how the binary fractions can point to GCs that could host an IMBH or a BHS. However, the observed kinematics are another piece of information that could also show the binaries interaction with a central IMBH. As we discussed in Section 4.3, binaries affect the line-of-sight and proper motion velocity dispersions differently. Figure 4.4 shows that the difference between line-of-sight and proper motion velocity dispersions increases significantly towards the centre, which goes in hand with the increase in the binary fraction in the cluster centre. To analyse this effect, we have measured the velocity dispersion within the core radius of each GC. We define a percentual difference for the velocity dispersion given by $(\sigma_{\rm los} - \sigma_{\rm ref})/\sigma_{\rm ref}$, where $\sigma_{\rm ref}$ is a reference velocity dispersion, which can be either from proper motions or a clean sample of line-of-sight velocities.

The top panel of Figure 4.9 shows the case when we compare the single epoch line-of-sight velocity dispersion (i.e. including the effect of binaries) with the radial proper motion. We observe that as the binary fraction increases, the difference between the velocity dispersions becomes larger. As discussed before, clusters with an IMBH have a lower binary fraction, and now we can see that they also have a smaller difference between the line-of-sight and proper motion velocity dispersions. GCs with a BHS (magenta diamonds) populate the region between the clusters with an IMBH and those without one. Obtaining comparable observations for line-of-sight velocities and proper motions is not straight forward, as not many cover the same region of the cluster or even

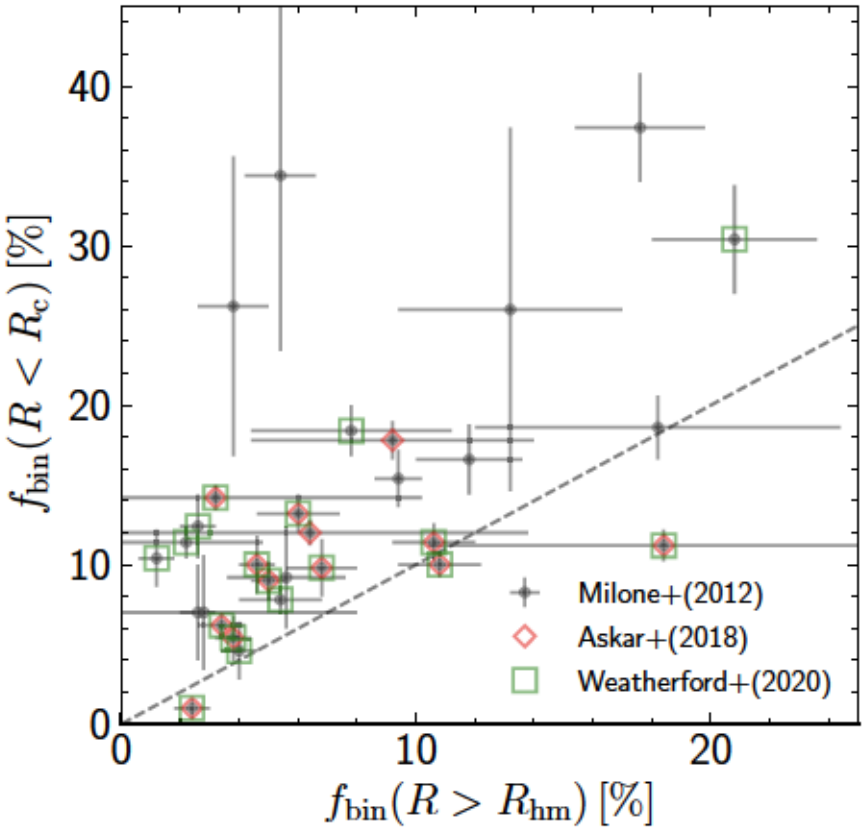

FIGURE 4.8: Binary fraction within the core radius $R_{\rm c}$ and outside the half-mass radius $R_{\rm hm}$ for Galactic globular clusters. The binary fractions measured by Milone et al. (2012a) show the same behaviour as Figure 4.7, almost all GCs are above the 1-to-1 dashed line, following the expected effect of mass segregation with the exception of ngc 288, see Section 4.1 for more details. We have marked GC candidates that may be hosting a BHS as given by Askar et al. (2018b) (red diamond) and Weatherford et al. (2020) (green squares). Most of the candidate GCs are located near the 1-to-1 line, in a similar way as in Figure 4.7.

the same stellar mass range. Due to the GC's evolution towards energy equipartition, it is crucial to sample the same stellar mass range for both velocities. A way to move around this issue is to only focus on the line-of-sight velocities, given multi-epoch observations to identify binaries. The difference between the line-of-sight velocity dispersion that includes all binaries and the cleaned sample will play the same role as the proper motion data. The bottom panel of Figure 4.9 shows the case when the reference velocity dispersion for $\Delta\sigma$ is the line-of-sight velocity dispersion after cleaning the binaries as described in Section 4.3. The GCs' behaviour is similar to the previous case, but it only depends on one observational data type, which is the RVs. We can now also include the kinematic data for NGC 3201 from Giesers et al. (2019). While this cluster has a higher binary fraction ($f_{\rm bin} = 17.1 \pm 1.9$) than our sample of simulated clusters, it follows the simulated clusters' trend. This approach could be more accessible as more GCs get observed in the same way as done by Giesers et al. (2019).

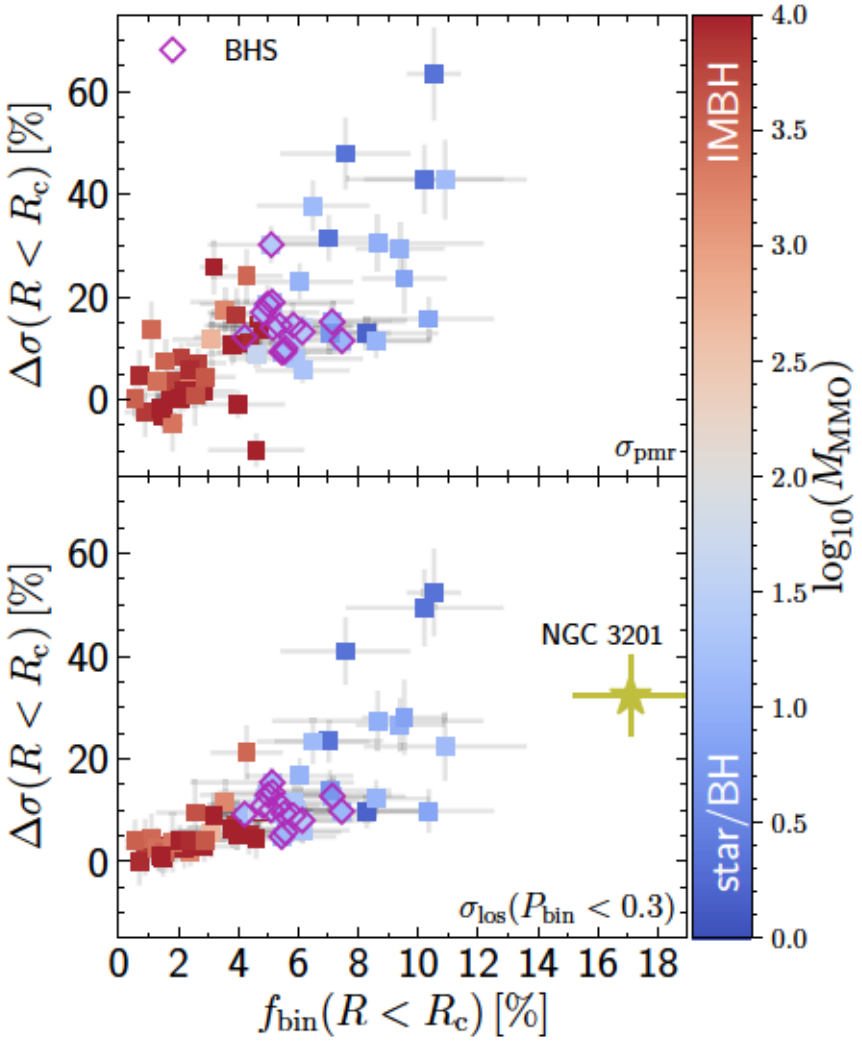

FIGURE 4.9: Difference in velocity dispersion and binary fraction within the core radius. By using the differences in velocity dispersion between the full line-of-sight contaminated sample and the proper motions (top panel) or the clean sample with $P_{\rm bin} < 0.3$ (bottom panel). All clusters are again colour-coded by their most massive object. In both panels, as the binary fraction within the core increases also does the difference in velocity dispersion, for some clusters the measured velocity dispersion with binaries overestimates up to 60% the core velocity dispersion. Using proper motions as a reference adds and additional scatter due to variations in the central velocity anisotropy, but when available could provide a first constraint on the velocity difference (in particular when multi-epoch observations are not available). A more self-consistent approach, once multi-epoch observations is to compare the contaminated velocity dispersion with the clean one as in the bottom panel. This approach is not affected by velocity anisotropy and can be used right away for current and upcoming MUSE data, such as for NGC 3201 (Giesers et al., 2019) marked as a star.

4.5 Summary

In this work, we explored the dynamical effects of a central IMBH on the binary population of GCs. We used a sample of simulated GCs from the MOCCA-Survey Database I (Askar et al., 2017) and applied the method proposed by Giesers et al. (2019) to identify binaries through multi-epoch radial velocity (RV) observations. We have produced mock observations for each cluster considering velocity errors in RVs and proper motions; for these mock observations, we follow the radial velocities during many epochs, considering long-term observations spanning over months as well as multiple observations during a single night. This approach allows us to identify binaries in the simulated GCs in the same manner as done for real observations.

Two-body relaxation drives the dynamical evolution of GCs; a consequence of this process is mass segregation. Binaries are on average more massive than single stars and segregate quickly towards the centre of the cluster. This phenomenon changes the distribution of binaries and the radial binary fraction. Early N-body simulations of GCs with primordial binaries show binaries migrate towards the cluster core while becoming harder (Heggie et al., 2006). Observations of main-sequence star binaries also show this trend (Sollima et al., 2007; Milone et al., 2012a; Ji & Bregman, 2015), as the binary fraction is smaller in regions outside the core radius. The higher fraction of binaries within the cluster core affects the observed line-of-sight kinematics, as the relative velocity of hard binaries dominates over their centre of mass velocity, increasing the observed velocity dispersion along the line-of-sight (see Figure 4.4 and discussion therein). While this effect does not affect proper motions, to take full advantage of proper motions and radial velocities, the identification of binaries is crucial. Whereas the effects on the dynamical modelling are beyond this work, we expect that due to the increase in the observed line-of-sight velocity dispersion, dynamical models will overestimate the cluster mass (larger mass-to-light ratio) and (or) the mass of a possible IMBH.

An IMBH in the cluster centre acts as an energy source, extending its dynamical life. It halts mass segregation, and therefore, fewer binaries move to the cluster centre, which reduces the binary fraction in the cluster core. Furthermore, the binaries that do segregate encounter a dense environment where interaction with other stars can disrupt them; if a binary manages to get close enough to the IMBH, this could also break the binary and one of the components might be ejected at high velocities (Hills, 1988; Fragione & Gualandris, 2019; Šubr et al., 2019). Given this more efficient break down of binaries, GCs with a central IMBH have a significantly lower binary fraction than clusters without one (see Figure 4.6). In average, GCs with an IMBH have 67% less binaries that those without an IMBH. We find that clusters that host a black hole system behave in a similar way as those with an IMBH and also show a flat binary fraction profile. However, as binary disruption is less effective than in clusters with a central IMBH, GCs with a BHS have on average higer binary fractions in their cores. This is in agreement with

previous simulations of GCs with BHS (see, e.g., Mackey et al., 2008; Sippel & Hurley, 2013; Morscher et al., 2015). The comparison of integrated quantities, such as the binary fraction within the central and outer regions of the GCs, serves as an indication for which cluster may host an IMBH or a BHS (see Figure 4.7). We find a handful of Galactic GCs are promising candidates, as they have a similar binary fraction within the cluster's core and outside of the half-mass radius (see Figure 4.8). A list of the names and properties of these clusters can be found in the appendix (see Table B.1)

By also taking into account the kinematic data, we can have a similar picture of the dynamical effect of an IMBH on the binary population of a cluster. Due to the lower binary fraction in clusters with a central IMBH, and in particular within the cluster core, we expect that the difference between line-of-sight and proper motion velocity dispersion will be small. We show that this is the case in Figure 4.9. However, comparing line-of-sight velocities and proper motions is not trivial. Different effects such as the intrinsic velocity anisotropy, the cluster regions covered by different observations, the magnitude range that translate in different masses for different observations, and precise distances; could add a systematic bias in the observed difference between line-of-sight and proper motion velocity dispersion.

A solution to these limitations will be to use only line-of-sight velocities once multi-epoch observations will be available as shown in the bottom panel of Figure 4.9. This approach will not only help as a method to identify systems that may host an IMBH or a BHS, but by knowing the binary fraction it will be possible to estimate the increase in velocity dispersion due to the effect of binaries; this is crucial for dynamical modelling that uses line-of-sight velocity as a tracer.

We have focused only on binaries brighter than one magnitude below the main-sequence turn-off ($m_V < 18$ mag at 5 kpc). The different mass range and binary detection biases limit the comparison with photometric studies (such as Sollima et al., 2007; Milone et al., 2012a; Ji & Bregman, 2015) that typically focus on the main-sequence. Extending or analysis to other detection techniques for binaries will provide a better link between the estimated binary fraction and kinematics effects of binaries. To do so, we first need to consider first multiple populations in the simulations (Hong et al., 2015) as they play a relevant role in the photometric binary detection (Milone et al., 2020). At the same time, it is necessary to check the different biases in the detection methods: radial velocity methods mainly detect binaries with short periods, whereas photometric methods depend on the mass ratio of binaries (Milone et al., 2012a).

We analysed simulations with initial binary fractions of $f_{\rm bin} = 10\%$. These clusters have total binary fractions of $f_{\rm bin} \sim 4\%$ at 12 Gyr. Whereas our initial binary fraction is consistent with observations, clusters that have higher binary fractions exist (see Figures 4.8 and 4.9). To compare with these observations, we need to study simulations with

higher binary fractions. We expect that the overall trends shown in this work will stay the same, but scaled up to higher binary fractions.

Here we presented the properties of the whole detected binary population. The next step will be to study how the relations described here connect with specific types of binaries or binary products. The distribution of blue-straggler stars traces the dynamical evolution of GCs Ferraro et al. (2012, 2018). By analysing the distribution of BBS and their relation with the binary fraction, it will be possible to study another tracer for the dynamical effects of a central IMBH. Similarly, the distribution of X-ray binaries could help separate clusters with a central IMBH from those with a BHS.

Chapter 5

Black hole scaling relations at lower masses

The following chapter describes work in progress aiming to apply dynamical models to a large sample of simulated globular clusters. The results presented here consider an initial sample of of approximately 10% *of all simulated GCs in the* MOCCA*-Survey I.*

5.1 Introduction

As introduced in Section 1.1.3, the mass of supermassive black holes correlates with their host galaxy properties. Two of these correlations are the $M_\bullet - \sigma$ and $M_\bullet - M_*$ scaling relations (Kormendy & Ho, 2013), with the $M_\bullet - \sigma$ being initially described 20 years ago (Ferrarese & Merritt, 2000; Gebhardt et al., 2000). However, so far, the origin of such scaling relations are still an open question. Jahnke & Macciò (2011) suggested that the observed scaling relations could be a consequence of multiple mergers between galaxies. On the other hand, the scaling relations could have a physical origin and indicate a co-evolution between the central massive BH and the host galaxy (Kormendy & Ho, 2013). If the latter is true, then these scaling relations should hold even at lower BH masses, like in the case of IMBHs and their host GCs.

The first effort by Lützgendorf et al. (2013b) to analyse the scaling relations for IMBHs in GCs shows that for Galactic GCs, the estimated masses for their central IMBH do follow a scaling relation. However, the slope of such relation is different than for Galaxies. Moreover, the difference is more significant for the $M_\bullet - \sigma$ relation than for the $M_\bullet - M_*$ relation (see Figure 1.1). Lützgendorf et al. (2013b) suggested that the discrepancy might be due to the continuous mass loss that GCs suffer during their evolution: the current masses and velocity dispersion of GCs do not represent their initial conditions. If the scaling relations have a physical origin, then the initial masses of GCs

should correlate with their central IMBH following a similar scaling relation than as galaxies. Following this idea, Kruijssen & Lutzgendorf (2013) used semi-analytic models to estimate the initial masses and velocity dispersions of Galactic GCs. Their models show that once they take into account the mass-loss and probable initial conditions, Galactic GCs do follow the same scaling relations as galaxies.

With the variety of simulations forming IMBHs in GCs (e.g., Gieles & Zocchi, 2015; Rizzuto et al., 2021; González et al., 2021), it is now possible to analyse if the different formation scenarios produce IMBH consistent with the scaling relations. In this chapter, we analyse a sample of simulated GCs with and without a central IMBH, first to test how the limitations of the dynamical models discussed in Chapter 3 and the kinematic effects of binaries discussed in Chapter 4 affect the estimation of putative IMBHs. Finally, we use the estimated IMBH masses to verify if our sample of simulated IMBHs is consistent with the scaling relations.

5.2 Methods

5.2.1 Simulations

We analyse a sample of simulated GCs from the `MOCCA`-Survey I (Askar et al., 2017). These clusters were evolved for 12 Gyr using the `MOCCA` code (Hypki & Giersz, 2013; Giersz et al., 2013), which follows the Monte Carlo method first described by Hénon (1971a,b). `MOCCA` includes single (SSE, Hurley et al., 2000) and binary (BSE, Hurley et al., 2002) stellar evolution. Dynamical interactions of binary stars with single or other binaries are followed with the `FEWBODY` code (Fregeau et al., 2004), which allows for the direct N-body integration of the dynamical formation, hardening and disruption of binaries. `MOCCA` includes different implementations for the natal-kicks of supernova remnants, which allows for a large retention fraction of stellar-mass black holes, as further described in Section 3.2.2. Furthermore, in `MOCCA` is possible to form IMBHs through runaway collisions of stellar-mass black holes during the first 100 Myr, a process called the 'FAST' scenario (Giersz et al., 2015). IMBHs can also form later in the GC evolution by the growth of a single stellar-mass BH through mergers with stars and other stellar-mass BHs, which is known as the 'SLOW' scenario (Giersz et al., 2015). Further details on the `MOCCA` code are described in Sections 3.2.1 and 4.2.1 and in detail in Hypki & Giersz (2013) and Giersz et al. (2013).

The `MOCCA`-Survey I (Askar et al., 2017) collects around 2000 star clusters composed by 10^4 to 10^6 stars, covering a broad range of parameters such as densities, metallicities, and binary fractions. From this collection, we select 274 GCs with masses between 5×10^4 and $2\times10^5\,M_\odot$; this is a preliminary selection which will be broadened in a more extensive analysis. The simulated clusters have initial binary fractions of $f_{\rm bin} = 10\%$

(143 clusters), $f_{\rm bin} = 30\%$ (18 clusters) and $f_{\rm bin} = 95\%$ (113 clusters). At 12 Gyr, the largest binary fraction observed is $f_{\rm bin} \sim 35\%$. Whereas the latter binary fraction is still an extreme case for observed GCs with binary fractions around 10% (see discussion in Section 1.2.1), it provides an opportunity to explore the effects of such binary fractions in our dynamical models. We select only bright stars in the range of $(-3, +1)$ magnitudes for each cluster with respect to its MSTO, similarly as done in Chapter 4. We limit our sample to GCs that have more than 2000 stars in the luminosity selected sample, which reduces our selection to 230 clusters. We do not distinguish if a GC hosts an IMBH or not, or if any BHS might be present in the cluster.

For each of the 230 simulated clusters in our sample, we build surface brightness and kinematic profiles by averaging multiple viewing angles to reduce stochasticity. To analyse the effects of the kinematic bias produced by binary stars, we produce two sets of profiles for each cluster: one with and another without binaries. The profiles with binaries follow the description presented in Sections 2.2.3 and 4.2.2 to project the luminosity weighted velocity of the binary components. While constructing the profiles, we also include a 3σ clipping, excluding stars (single or binaries) with an extremely high line-of-sight velocity and that can single-handedly bias the measured velocity dispersion.

5.2.2 Dynamical models

For each cluster, we build dynamical models based on the Jeans equation (Jeans, 1922) that for spherical coordinates (r, θ, ϕ) is given by:

$$\frac{d}{dr}\left(\nu(r)\langle \mathrm{v}_r^2\rangle\right) + \nu(r)\left(\frac{d\Phi}{dr} + \frac{2\langle \mathrm{v}_r^2\rangle - \langle \mathrm{v}_\phi^2\rangle - \langle \mathrm{v}_\theta^2\rangle}{r}\right) = 0\,, \tag{5.1}$$

where $\langle \mathrm{v}_r^2\rangle$, $\langle \mathrm{v}_\theta^2\rangle$, $\langle \mathrm{v}_\phi^2\rangle$ are the second velocity moments, $\nu(r)$ is the tracer density which in this case we assume follows the luminosity density $j(r)$ as $\nu(r) \propto j(r)$ (for further details on the Jeans equations see Sections 2.1.3 and 3.2.3). Φ is the gravitational potential, which for a spherically symmetric system is given by:

$$\Phi = -\frac{GM(r)}{r}. \tag{5.2}$$

We simplify Equation 5.1 by assuming that the GCs are isotropic and hence $\langle \mathrm{v}_r^2\rangle = \langle \mathrm{v}_\theta^2\rangle = \langle \mathrm{v}_\phi^2\rangle$. GCs usually have a nearly isotropic velocity dispersion towards the cluster centre and become more radially anisotropic towards their outskirts (Watkins et al., 2015). As we are interested mainly in the cluster centres where an IMBH resides, this assumption will not significantly affect the results. We show in Section 3.4.1 that velocity anisotropy alone cannot significantly bias the estimated mass for the IMBHs.

Following the approach described in Sections 2.1.3 and 3.3.1, we start with the surface brightness profile $L(R)$ to find the deprojected luminosity density $j(r)$:

$$j(r) = \frac{-1}{\pi} \int_r^\infty \frac{dR}{\sqrt{R^2 - r^2}} \frac{dL}{dR}, \tag{5.3}$$

which we use as a proxy for the tracer density $\nu(r)$ and the mass density $\rho(r)$ through a mass-to-light ratio υ_0, $\rho(r) = \Upsilon_0 j(r)$. The cumulative mass of the GC is given by:

$$M(r) = M_\bullet + 4\pi \int_0^r \rho(r') r'^2 dr', \tag{5.4}$$

where $M_\bullet$ is the mass of the putative IMBH.

We accelerate the fitting by defining $f_{\rm bh} = M_\bullet / M_*$, as the fit parameter instead of $M_\bullet$, the cumulative mass redefines to:

$$M(r) = f_{\rm bh} M_* + 4\pi \int_0^r \rho(r') r'^2 dr', \tag{5.5}$$

where M_* is the total stellar mass given integral of the the density $\rho(r)$. This redefinition of parameters allows us to build a small number of models that are later scaled using Υ_0 to compare to the observed kinematics. For each cluster, we explore a parameter space defined by $0 \leq f_{\rm bh} \leq 1$ and $0.4 \leq \Upsilon_0 \leq 20$.

We find the best fitting values through a χ^2 minimisation, as described in Sections 2.1.3 and 3.3.1, following:

$$\chi^2 = \sum \frac{\left(\langle \mathrm{v} \rangle_{\rm data}^{1/2} - \langle \mathrm{v} \rangle_{\rm model}^{1/2} \right)^2}{\left(\delta \langle \mathrm{v} \rangle_{\rm data}^{1/2} \right)^2}, \tag{5.6}$$

where $\langle \mathrm{v} \rangle_{\rm data}^{1/2}$ is the observed second velocity moment profile and $\langle \mathrm{v} \rangle_{\rm model}^{1/2}$ is the model given by:

$$\langle \mathrm{v} \rangle_{\rm model}(R) = \frac{1}{L(R)} \int_R^\infty \frac{j(r) dr}{\sqrt{r^2 - R^2}} \langle \mathrm{v}_r^2 \rangle . \tag{5.7}$$

5.3 Results

We obtain best-fit models for 230 simulated GCs with and without an IMBH, estimating the mass of the putative IMBH and the cluster mass-to-light ratio. From this sample, we only focus on clusters with a measured velocity dispersion within the half-light radius above 4 km/s and that have a reduced χ^2 below 2. The first criterion excludes GCs with low velocity dispersion, potentially dominated by binary stars (this happens at all initial binary fractions). The second criterion excludes dynamically old GCs with a significant degree of energy equipartition that our models describe insufficiently. Therefore, the

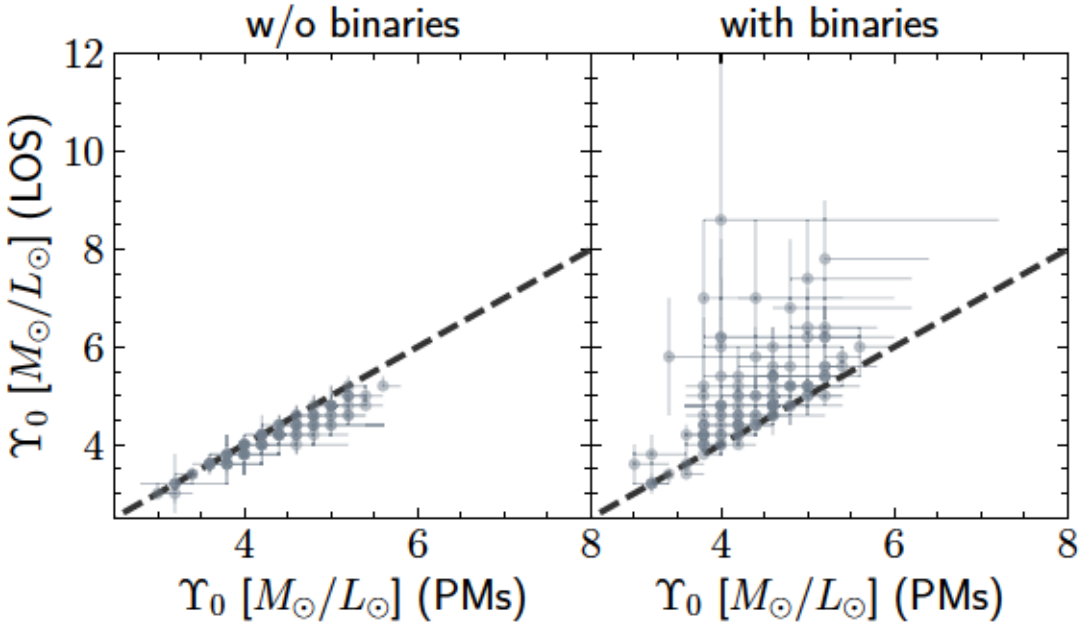

FIGURE 5.1: Best-fit mass-to-light ratio Υ_0 in our sample of simulated GCs. Left: without the effect of binaries. Right: with the effect of binaries. The estimation was carried out using kinematic constraints from line-of-sight (LOS) velocities or proper motions (PMs). The dashed line represents the one-to-one ratio. We can see that if we include the kinematic effect of binaries, the estimated mass-to-light ratio could be significantly overestimated for constraints given by line-of-sight velocities.

original sample reduces to 111 GCs, where 93 have an IMBH, and 16 do not have an IMBH, but have retained stellar-mass BHs.

Figure 5.1 shows the estimated mass-to-light ratios for the samples with and without binaries. We see that when binaries are excluded, the estimated mass-to-light ratios are consistent for fits using line-of-sight velocities (LOS) and proper motions (PMs). This is not the case when binary stars contaminate the line-of-sight velocities. We notice that for many GCs the estimated mass-to-light ratios when using line-of-sight velocities are much larger than for the estimates obtained using proper motions only. The overestimation of the mass-to-light ratio confirms the discussion presented in Section 4.5, where we first speculated on this consequence.

Figure 5.2 shows the case for the estimated IMBH masses. The samples that exclude binaries have similar estimates for both line-of-sight and proper motion velocities. Only at lower IMBH masses, we observe a significant scatter from the one-to-one relation; we will discuss this further in Section 5.4.1. On the other hand, when we allow for binary contamination, we see that the scatter extends to larger IMBH masses. As discussed in Section 4.4.2, GCs with an IMBH have lower binary fractions; therefore, the contamination is less significant than for GCs without an IMBH. However, the retained binaries still can affect the dynamical modelling. We note that for the high-mass IMBH cases, we systematically underestimate the IMBH mass using LOS velocities, which could

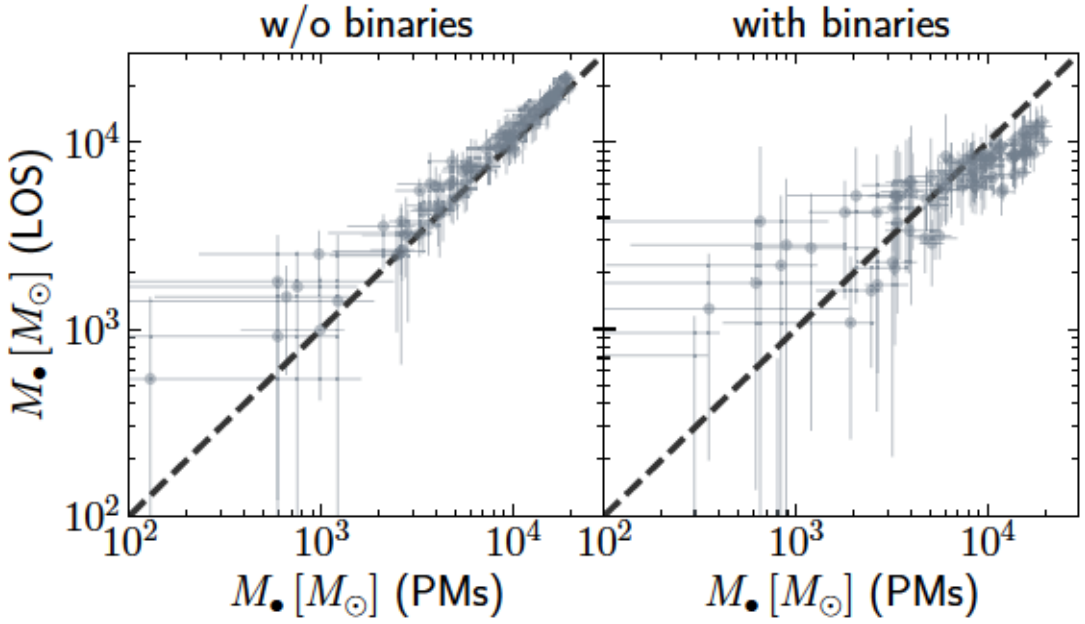

FIGURE 5.2: Best fit IMBH masses in our sample of simulated GCs. As in Figure 5.1, for cases with and without binary stars and constraints from two kinematic samples: line of sight velocities (LOS) and proper motions (PMs). Binary stars enhance the scatter at all masses, and particularly at low IMBH masses.

potentially be a consequence of the 3σ clipping that excluded some of the high-velocity stars that were not binaries, particularly for the innermost region of the clusters.

With the estimated IMBH masses, mass-to-light ratios and measured velocity dispersions, we include the simulated clusters into the $M_\bullet - \sigma$ and $M_\bullet - M_*$ scaling relations, as shown in Figure 5.3. Note that the simulated GCs have lower masses and velocity dispersions than the GCs from the Milky Way (Lützgendorf et al., 2013b); however, the IMBHs of the simulated GCs have larger masses than predicted by the scaling relations, locating them further away from the scaling relations estimated by Lützgendorf et al. (2013b). The IMBHs formed within `MOCCA` do not have any a priori description for the formation scenario; they mostly form due to runaway collisions in highly dense stellar systems (see discussion in Sections 3.2.1 and 4.2.1). The results presented in Figure 5.3 open a series of questions that we will further discuss in Sections 5.4.2 and 5.4.3.

5.4 Analysis

5.4.1 IMBH mass recovery

As pointed out in the discussion of Figure 5.2, low-mass IMBHs show an increased scatter and large error bars for both the sample with and without binary stars. In Chapter 3, we show that our dynamical models are able to robustly detect an IMBH

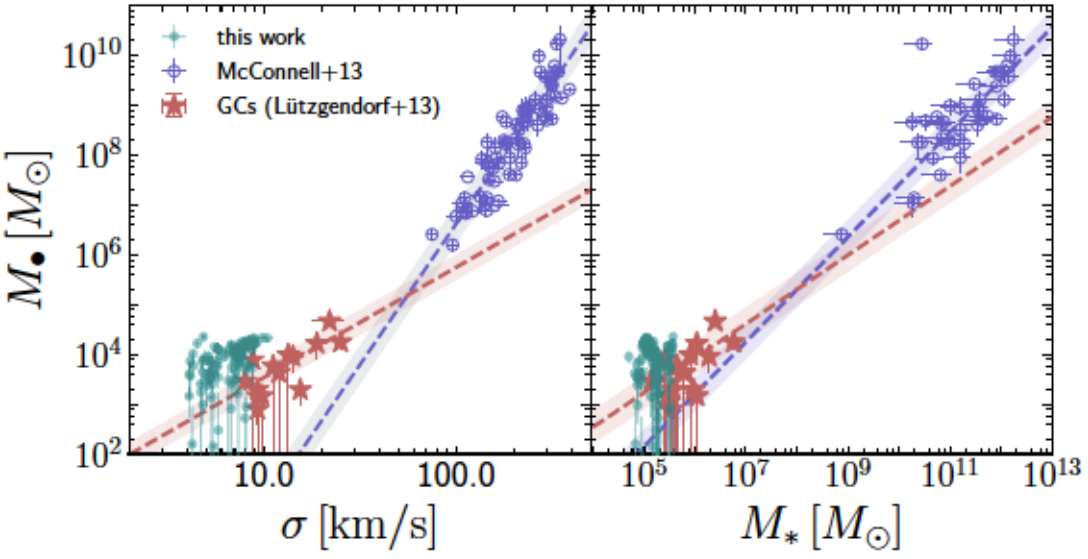

FIGURE 5.3: $M_\bullet - \sigma$ and $M_\bullet - M_*$ scaling relations, as shown in Figure 1.1. We include the estimated IMBH masses, velocity dispersions and total masses of the simulated GCs (teal dots). The scaling relations as given by Galactic GCs (Lützgendorf et al., 2013b) and galaxies (McConnell & Ma, 2013) are also included for comparison.

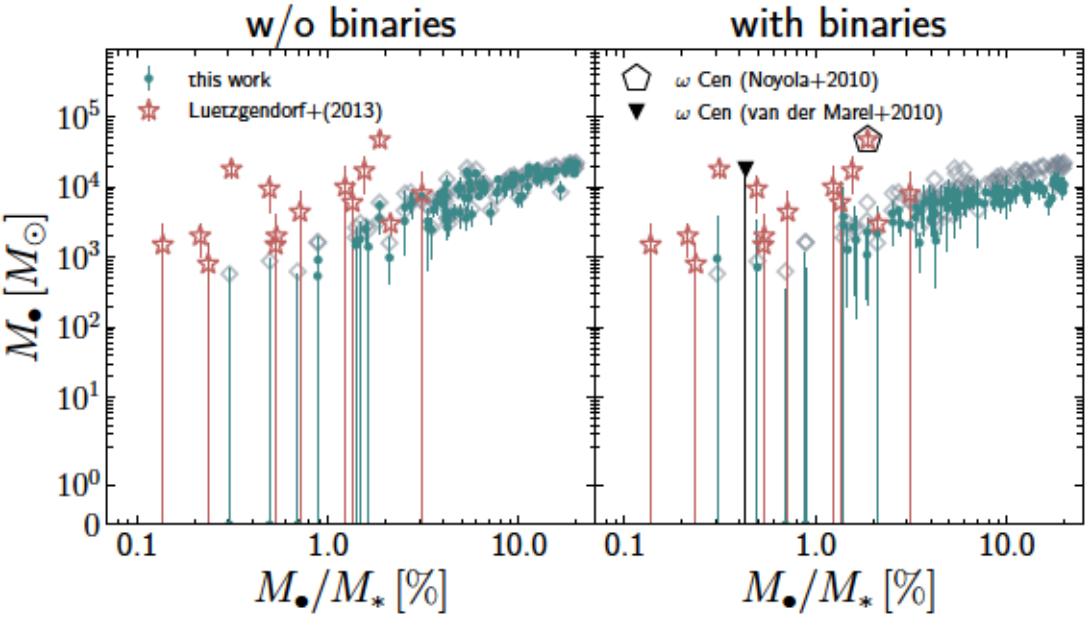

FIGURE 5.4: Estimated IMBH mass given the IMBH's mass fraction ($M_\bullet/M_*$) for the sample with (right) and without (left) binaries. In both cases we can see that for low IMBH mass fractions, the constraints are less robust, with large error bars and upper limits, particularly for $M_\bullet/M_* \leq 2\%$. We include a sample of estimated IMBH masses from the literature (Lützgendorf et al., 2013b). The grey diamonds represent the real IMBH masses obtained from the MOCCA-Survey I rather than our calculations.

with a mass fraction of $M_\bullet/M_* = 4.1\%$ but struggle with an IMBH with a mass fraction of $M_\bullet/M_* = 0.3\%$. Figure 5.4 shows the estimated IMBH masses with errors for all GCs with respect to the IMBH mass fraction, which was measured using the real IMBH and GC masses (teal dots). The real IMBH masses taken from the simulations are shown as open diamonds. It is immediately clear that for higher-mass IMBHs, the constraints are better and, for the sample without binaries, consistent with their real values. For the case that includes the effects of binaries, we notice an underestimation, which, as discussed in Section 5.3 could potentially be a consequence of the method used for making the kinematic profiles. On the other hand, at the low-mass end, we observe that we only obtain upper limits and large error bars in many cases. Given the current sample, we can infer that IMBHs with mass fraction below $M_\bullet/M_* < 2.0\%$ are harder to constrain. The lack of constraints could be because low mass fraction IMBHs do not produce a clear kinematic signature or because the assumption of constant mass-to-light ratio does not provide an adequate model for the stellar mass distribution. Further analysis is required to disentangle these effects.

The lack of constraints for low mass fractions serves as an attention call for the IMBH mass estimates for the Milky Ways GCs. Figure 5.4 also shows the estimated masses for a sample of Galactic GCs (Lützgendorf et al., 2013b). Many of these clusters are located in the low mass fraction end, showing upper limits and large error bars. As discussed in Section 1.3.2, many observational limitations make it difficult to detect an IMBH robustly. NGC 5139 (ω Cen) is an interesting case, as it has been analysed repeatedly with no robust IMBH estimate so far (see Table 1.2). In Figure 5.4, the IMBH mass and mass fraction for NGC 5139 are based on line-of-sight velocities by Noyola et al. (2010) with an IMBH mass of $M_\bullet = 4 \times 10^4\,M_\odot$ and mass fraction of $M_\bullet/M_* = 1.87\%$ (pentagon in Figure 5.4). In contrast, estimates with proper motions by van der Marel & Anderson (2010) put the mass at an upper limit of $M_\bullet \leq 1.8 \times 10^4\,M_\odot$ with a mass fraction of $M_\bullet/M_* \sim 0.43\%$ (black triangle in Figure 5.4). If line-of-sight velocities are contaminated by binary stars, they may increase the estimated mass of the putative IMBH up to a factor 4, as shown in Figure 5.2.

5.4.2 Stellar-mass black holes

We have earlier discussed how GCs that have retained a significant fraction of stellar-mass black holes (BHS) might have similar dynamical and kinematical properties (see Sections 3.4.2 and 4.4.1). We note that this is also the case for the scaling relations, as BHSs can be confused for IMBHs (or at least create significant upper IMBH mass limits). Figure 5.5 shows a close-up of the $M_\bullet - \sigma$ relation presented in Figure 5.3, focussing only on the simulated clusters. We see that GCs that have retained stellar-mass BHs are consistent with the population of simulated clusters with a central IMBH.

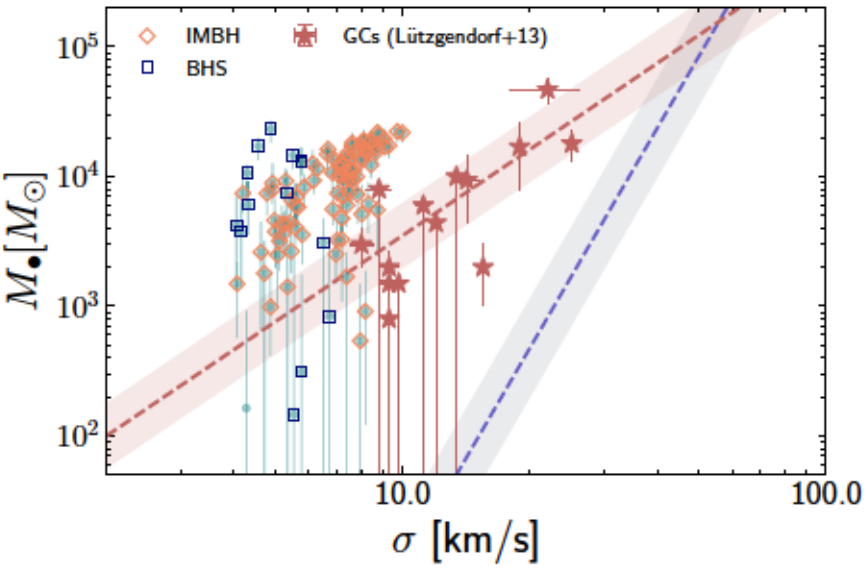

FIGURE 5.5: Zoom-in of the $M_\bullet - \sigma$ relation as shown in Figure 5.3. We have identified the simulated GCs with a central IMBH (orange diamonds) and those with retained stellar-mass BHs (BHS). Due to the limitations of our assumption on the constant mass-to-light ratio, GCs with a BHS can be confused with hosting a central IMBH. We see that the estimated masses for such cases are consistent with the masses of the real IMBHs.

Whereas the measured IMBH masses are a consequence of our models not being able to account for extended dark masses and variable mass-to-light ratio, it is important to highlight that under these conditions, it would be possible to mistake a BHS for an IMBH, and that they will still follow the scaling relations. This motivates the need for models that can take into account variable mass-to-light ratios.

5.4.3 Initial GC masses

A crucial difference between GCs and the centres of galaxies is that while GCs lose mass during their evolution, galaxies keep growing their central masses, questioning if GCs should follow the same scaling relations as galaxies. As suggested by Lützgendorf et al. (2013b) and followed up by Kruijssen & Lutzgendorf (2013) with semi-analytic models, the initial mass of the cluster could be closer to the scaling relation for galaxies. For the first time, thanks to our simulation catalogue and modelling technique, we can test this point directly.

Figure 5.6 shows the $M_\bullet - M_*$ scaling relation for our simulated clusters, where we consider each cluster's current and initial mass. The estimated scaling relations by the Milky Way GCs (dashed line, Lützgendorf et al., 2013b) and galaxies (dot-dashed line, McConnell & Ma, 2013) are shown as a reference. We see that with the initial mass, GCs move to the right and overlap with both scaling relations. However, it is not clear if they follow either of them. As mentioned before in Section 5.3, the IMBHs in `MOCCA`

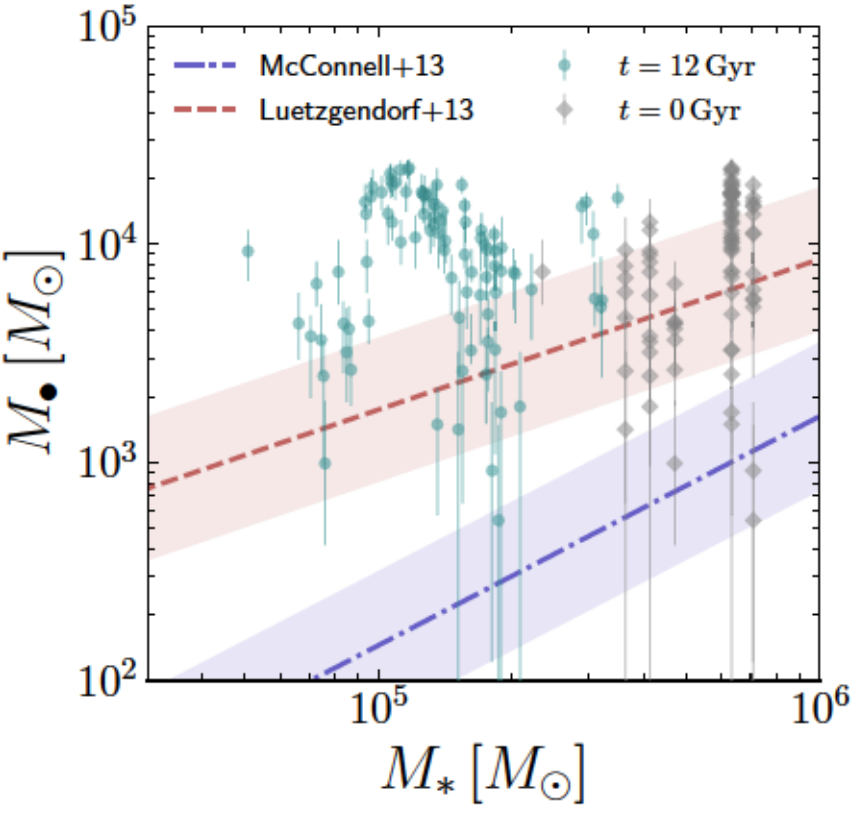

FIGURE 5.6: $M_\bullet - M_*$ scaling relation for the simulated GCs. When we consider the initial mass of GCs (grey diamonds) instead of the current mass (teal dots), we see that the simulated GCs are more consistent with the scaling relations estimated from Galactic GCs (Lützgendorf et al., 2013b) and galaxies (McConnell & Ma, 2013). However, we cannot disentangle which scaling relation they initially follow.

form trough runaway mergers early in the GC's evolution or later by many mergers through the GC's evolution. Furthermore, the treatment of the recoil after a merger of two stellar-mass black holes in `MOCCA` might produce a bias towards more massive IMBHs (Giersz et al., 2015).

5.5 Summary

In this chapter, we built dynamical models to estimate the mass of a putative IMBH and the mass-to-light ratio of 230 simulated GCs. We analysed the limitations of our dynamical model presented in Chapter 3 in a much larger sample of GCs and include the contamination of binary stars in the line-of-sight velocity dispersion discussed in Chapter 4.

We find that when we include the effects of binaries in the line-of-sight velocity dispersion, the estimated mass-to-light ratios systematically overestimate those obtained from proper motions, which could translate to an overestimation of the cluster mass. For

the estimated IMBH masses, we first find that those with a lower mass fraction either have large error bars or only have upper limits, which confirms the results of Chapter 3. When the kinematic effects of binaries are taken into account, we observe a larger scatter for low-mass IMBH, so mass estimates coming from line-of-sight and proper motions velocities are less consistent with each other.

With the estimated IMBH masses, we analyse the behaviour of the simulated GCs in the $M_\bullet - \sigma$ and $M_\bullet - M_*$ scaling relations. In both cases, we find that the simulated GCs follow neither of the scaling relations for Galactic GCs (Lützgendorf et al., 2013b) or galaxies (McConnell & Ma, 2013). GCs in our current sample are less massive than Galactic GCs, but many have more massive IMBHs than expected by comparing with the scaling relations from Galactic GCs. As discussed by Giersz et al. (2015), the treatment in `MOCCA` for the recoil after a BH-BH merge could have allowed for a more efficient growth of the final IMBH masses.

We also show that a retained population of stellar-mass black holes could be confused for an IMBH, and the estimated masses are consistent with the cases for real IMBHs (in agreement with, van der Marel & Anderson, 2010; Zocchi et al., 2019; Baumgardt et al., 2019b; Vitral & Mamon, 2021). Finally, we tested if our sample of simulated GCs follows the scaling relations once we consider their initial conditions. While the comparison improves from when the current GC's properties are considered, they still do not appear to follow the scaling relation for galaxies.

Through the dynamical analysis of simulated GCs, which form an IMBH, we can, for the first time, test if the formation scenarios are consistent with the scaling relations. While the results presented here are just the initial step, it will be possible to understand the origin of the scaling relations better by expanding our sample.

Chapter 6

Conclusions and outlook

This thesis explores the limitations due to the assumptions in the dynamical models commonly used to determine the masses of IMBHs in GCs. By applying models based on the Jeans equations (Section 2.1.3 and 3.2.3) to simulated GCs (Sections 2.2, 3.2.1 and 5.2), we analysed the recovery of putative IMBHs in GCs (Chapter 3). We suggest new paths of evidence for the presence or absence of an IMBH through its interaction with the binary population of GCs (Chapter 4). Finally we explore the consequences of the results linked to the $M_\bullet - \sigma$ and $M_\bullet - M_*$ scaling relations, between the black hole mass $M_\bullet$ and the velocity dispersion σ or mass M_* of their host stellar system (Chapter 5). The following section summarises the main results presented in these chapters and provides a series of follow-up ideas to further constrain the presence or absence of IMBHs at the centre of GCs.

6.1 Summary and conclusions

Intermediate-mass black holes with masses between $10^2 - 10^5\,M_\odot$ are an elusive population, with only a couple of promising candidates (Section 1.1.4). They have been proposed as possible seeds for the supermassive black holes observed at high redshifts (Section 1.1.1). Dense stellar systems such as nuclear star clusters and globular clusters, where runaway collisions are likely to happen, are the possible birthplaces of IMBHs (Section 1.1.2). The extrapolation of the $M_\bullet - \sigma$ relation points towards GCs as the systems where an IMBH of masses $10^2 - 10^4\,M_\odot$ can be found (Section 1.1.3). Considering both premises, many studies have looked into the centres of the Milky Way's GCs to find IMBHs (see Table 1.2); however, no robust evidence exists so far. Multiple observational limitations could be behind the lack of robust constraints (Section 1.3.2).

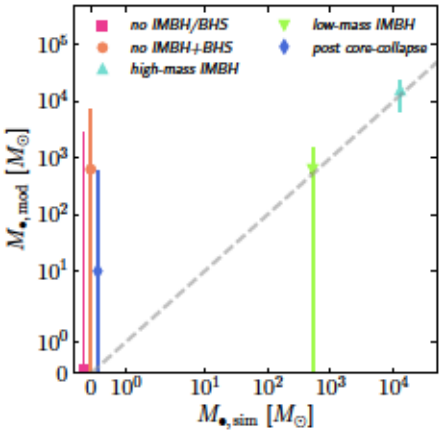

FIGURE 6.1: Primary result of Chapter 3. Inferred mass of a central IMBH in different GCs. Whereas dynamical models can easily detect a high-mass IMBH (with $M_\bullet/M_\star \sim 4\%$), it is challenging to detect a low-mass one ($M_\bullet/M_\star \sim 0.3\%$) or rule out IMBH candidates. This is a repetition of Figure 3.10, for further detail see Section 3.3.2

6.1.1 Dynamical constraints of IMBHs

Chapter 3 discusses the reliability of the commonly used dynamical modelling techniques to find IMBHs at the centres of GCs. For the first time, we take an independent approach to analyse GCs with an IMBH and GCs with features that could be misinterpreted as dynamical effects due to a central IMBH. We applied dynamical models based on the Jeans equations (Sections 2.1.3 and 3.2.3) to a sample of five selected Monte Carlo simulations from the MOCCA-Survey Askar et al. (2017), with similar masses and observed properties but different central central object: a cluster without an IMBH or significant fraction of stellar-mass black holes, a cluster with ~ 140 stellar-mass black holes (BHS), a cluster with a high-mass IMBH ($M_\bullet = 1.2 \times 10^4\, M_\odot$), a low-mass IMBH ($M_\bullet = 5.2 \times 10^2\, M_\odot$) and a cluster without an IMBH but after core-collapse.

We find that dynamical models are reliable to detect a high-mass IMBH ($M_\bullet/M_{\mathrm{GC}} \sim 4\%$), but struggle to robustly detect a low-mass IMBH ($M_\bullet/M_{\mathrm{GC}} \sim 0.3\%$) and to rule out the presence of an IMBH when it is not there (see Figure 6.1). We also show that the presence of a stellar black hole subsystem in the GC makes it even more challenging to rule out the presence of an IMBH.

We speculate that the reason behind this is the additional complexity caused by the collisional nature of the GC (see Section 1.2.2 and discussion in Section 3.4.2). Due to the two-body relaxation process, more massive stars in a GC segregate faster to the centre producing a mass-to-light ratio that varies with radius (see Figure 3.11). While the assumption of a constant mass-to-light ratio is suitable for estimating general properties like the mass within the half-light radius, it does not provide sufficient constraints for the central mass distribution or the cluster's total mass (for the latter, see Figure 3.14). It is necessary then to develop models that go beyond these assumptions and produce

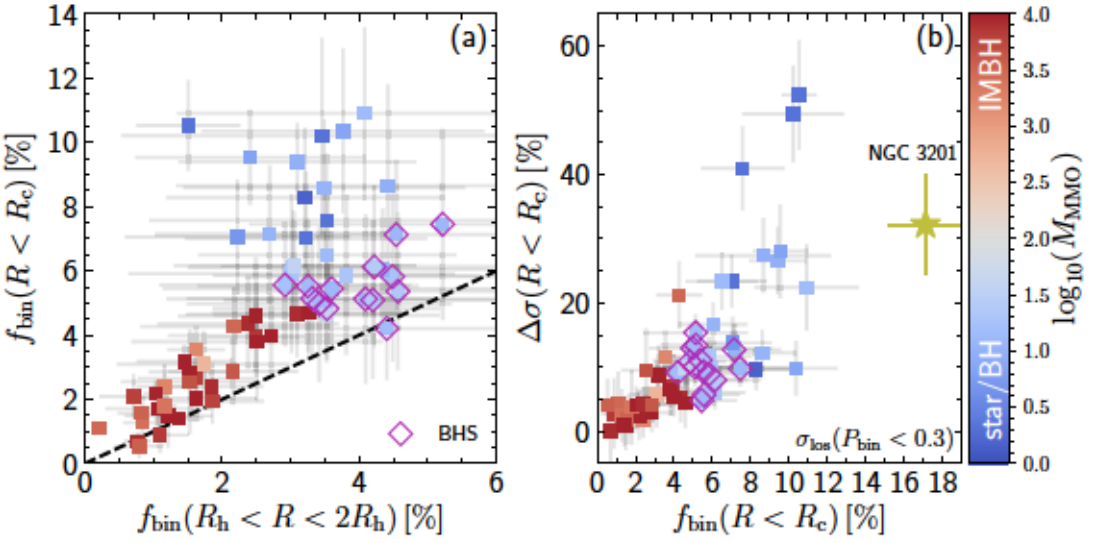

FIGURE 6.2: Primary results of Chapter 4. Panel (a): Binary fractions within the core radius and at the half-light radius. Panel (b): line-of-sight velocity dispersion difference for samples with and without binaries and binary fraction within the core radius. Both panels colour coded by the mass of the central object. The low binary fraction and velocity dispersion difference provide indirect evidence for the presence of an IMBH in GCs. Panel (a) is a repetition of Figure 4.7 while panel (b) corresponds to the bottom panel of Figure 4.9, for further details see Section 4.4.

a better representation of the mass distribution and kinematics of GCs. Improvements to the dynamical models presented in this thesis are described in Section 6.2.1.

6.1.2 Binary stars and IMBHs

In Chapter 4, we analyse the kinematic and dynamical effect of a central IMBH on the binary population of GCs. GCs have a non-negligible fraction of binary stars of around 10% (Sections 1.2.1 and 4.1). The interaction between binaries and a central IMBH can produce indirect evidence for the presence of an IMBH, as it can quench the segregation of binaries towards the centre and disrupt the binary systems that do segregate, leading to a lack of binaries around the IMBH (Section 4.4). We show for the first time that this lack of binaries can be interpreted as indirect evidence for the presence of an IMBH.

We study the lack of binary stars towards the cluster centre due to an IMBH by comparing the binary fractions within the GC's core radius for a sample of 65 simulated clusters. The simulations are part of the `MOCCA`-Survey and were evolved to 12 Gyr using the `MOCCA` code (Sections 2.2.2 and 4.2.1). All clusters have identical initial binary fraction of $f_{\rm bin} = 10\%$, but different central objects at 12 Gyr: an IMBH, a stellar-mass black holes system or neither of them (Section 4.2.1).

The left panel of Figure 6.2 shows the binary fraction for the GC sample within the core radius and at the half-light radius. Clusters with a central IMBH have fewer binaries

than clusters without one, given the same initial binary fraction; moreover, GCs with a central IMBH also stay near the one-to-one relation, consistent with a flatter radial profile for the observed binary fraction (see Figure 4.6). Clusters with retained stellar-mass black holes also show a flatter profile while still having a higher binary fraction than GCs with an IMBH. On the other hand, GCs without an IMBH or stellar-mass black holes have a much higher binary fraction within the core radius (Section 4.4.1).

The presence of binaries can increase the observed line-of-sight velocity dispersion, which is due to the binary components intrinsic orbital motion around their centre of mass (Section 4.3). The right panel of Figure 6.2 shows the difference between the observed line-of-sight velocity with and without binaries and the binary fraction, both within the core radius. Cluster with more binaries will have a larger increase in the observed line-of-sight velocity dispersion. As the intrinsic motion of binaries mainly affects the line-of-sight velocities, discrepancies between line-of-sight velocity dispersion and proper motions can provide an indirect detection for the presence of an IMBH, as a cluster with an IMBH will have similar velocity dispersions (see Figure 4.4 and discussion in Section 4.4.2).

Follow up observations such as the carried out by Giesers et al. (2019) in other Milky Way's GCs will open opportunities to study the binary fraction of GCs and directly analyse the kinematic effects of binaries, leading to new evidence for the presence of IMBHs in GCs.

6.1.3 IMBHs and scaling relations

In Chapter 5 we apply the dynamical models presented in Sections 2.1.3 and 3.2.3 to a selection of 230 simulated GCs. For each cluster, we use velocity dispersion profiles with and without the effects of binaries to constrain the mass-to-light ratio of the GCs and the mass of a possible central IMBH. We find that when the impact of binaries in the line-of-sight velocity dispersion discussed in Chapter 4 is considered, the best-fit models from line-of-sight velocities systematically overestimate those from proper motions alone. We also find that binaries make the estimated IMBH masses less consistent between line-of-sight and proper motion velocities, particularly at the low IMBH masses.

Figure 6.3 shows the primary result from the dynamical modelling on this larger GCs sample. Whereas the high-mass IMBHs are robustly detected, our models struggle to constraint the mass of low-mass IMBHs, particularly for those with a mass fraction below 2%. The lack of constraints could be due to our model assumptions (i.e. constant mass-to-light ratio) or be caused by the fact that these IMBHs do not produce clear enough kinematic signatures. Further analysis is necessary to disentangle both effects; however, this puts a cautionary note for the dynamical modelling of GCs with a possible

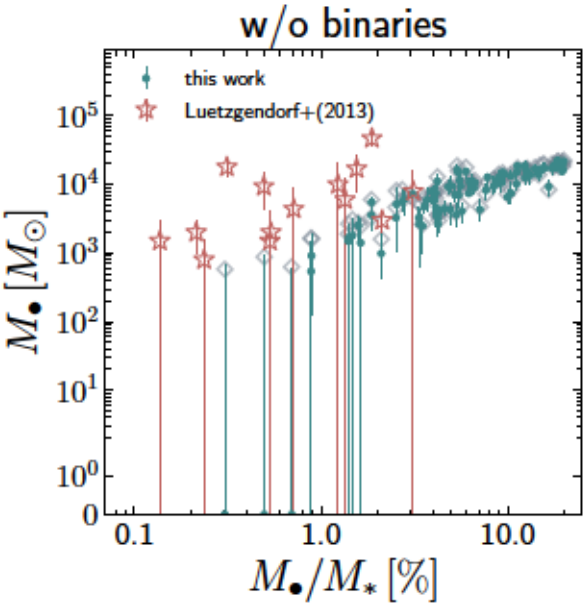

FIGURE 6.3: Primary result of Chapter 5. Estimated IMBH masses given the IMBH's mass fraction $M_\bullet/M_*$. Our models (teal dots) struggle to constrain the mass of IMBHs with lower mass fraction, particularly for those below 2%. As Galactic GCs (red stars, Lützgendorf et al., 2013b) also fall within this region, it is necessary to be aware of the model limitations. The real IMBH masses are included as grey diamonds. This figure corresponds to a repetition of Figure 5.4, and further details can be found in Section 5.4.1.

IMBH. Furthermore, we notice that a sample of Galactic GC candidates to host an IMBH fall within this region (red stars).

We compare the estimated IMBH masses of our sample with previous estimates for the $M_\bullet - \sigma$ and $M_\bullet - M_*$ scaling relations, comparing the mass of the central IMBH and properties of their host stellar system. The simulated GCs in our sample hosting an IMBH appear to follow the scaling relations for Galactic GCs (Lützgendorf et al., 2013b) or galaxies (McConnell & Ma, 2013). While the situation improves once we consider the initial conditions of our sample of simulated GCs, the IMBHs do not clearly follow the scaling relations. While further analysis is necessary, for the first time, we use dynamical models of simulated GCs hosting IMBHs to better understand the origin of scaling relations. If any of the formation scenarios discussed in Section 1.1.2 produce IMBHs that follow the scaling relations, it will help to clarify the physical origin of these relations.

6.2 Future projects

We are in a golden age for the study of the dynamical state of GCs. Current observations have unveiled the rotation of GCs (Ferraro et al., 2018; Bianchini et al., 2018; Kamann et al., 2018; Sollima et al., 2019), the characterization (Alfaro-Cuello et al., 2019) and

the distinct kinematics of multiple stellar populations in GCs (Dalessandro et al., 2018; Alfaro-Cuello et al., 2020; Kamann et al., 2020a), and the distribution of binary stars in GCs (Giesers et al., 2019; Milone et al., 2020). HST observations have allowed for the analysis of the energy equipartition in GCs (Heyl et al., 2017), and Gaia observations have been crucial for the identification of stars close and beyond the tidal radius of GCs (Bianchini et al., 2019b; Kundu et al., 2021). By combining these different pieces of the puzzle, one finds a unique opportunity to build an exhaustive view of the dynamical state of GCs.

6.2.1 Improvement of dynamical models

Chapter 3 described the dynamical model limitations produced by assuming a constant mass-to-light ratio. As observations keep improving it has become necessary to advance our dynamical models, as they are necessary to create a link between simulations and observations and to interpret these observations in the first place.

Dynamical models which allow for a non-parametric variable mass-to-light ratio have taken the first step forward towards improvement, but still, struggle to constrain the mass profiles (Lützgendorf et al., 2013a; den Brok et al., 2014; Hénault-Brunet et al., 2019b). An alternative is to instead represent the clusters as a collection of different mass populations, work in this directions has been carried out by van der Marel & Anderson (2010) who added an extended "dark-mass" component to their Jeans models. A similar approach has been followed by Vitral & Mamon (2021) which also included an extended "dark mass" to their Jeans model implementation and compared the models with a bright and faint stellar sample. The new implementation presented here will not only consider the effects of mass segregation through multiple-mass components as done by (Vitral & Mamon, 2021), but will also consider the direct effects of energy equipartition on the observed velocity dispersions.

The dynamical evolution of a GC follows the two-body relaxation, which produces two primary effects: mass segregation and energy equipartition (Section 1.2.2). A direct consequence of mass segregation is a variable mass-to-light ratio. If we constrain the variable mass-to-light ratio, it is possible to generate a dynamical model which represents the cluster. However, depending on the degree of energy equipartition of a given GC has, the observed velocity dispersion will differ from the expected one. In other words, above the velocity dispersion due to the overall gravitational potential, the velocity dispersion of each mass population changes depending on the kinetic energy interchange between more massive and less massive stars.

Now, if we represent the cluster with multiple single-mass stellar populations with constant mass-to-light ratio, as shown in Figure 6.4, the observed velocity dispersion for a

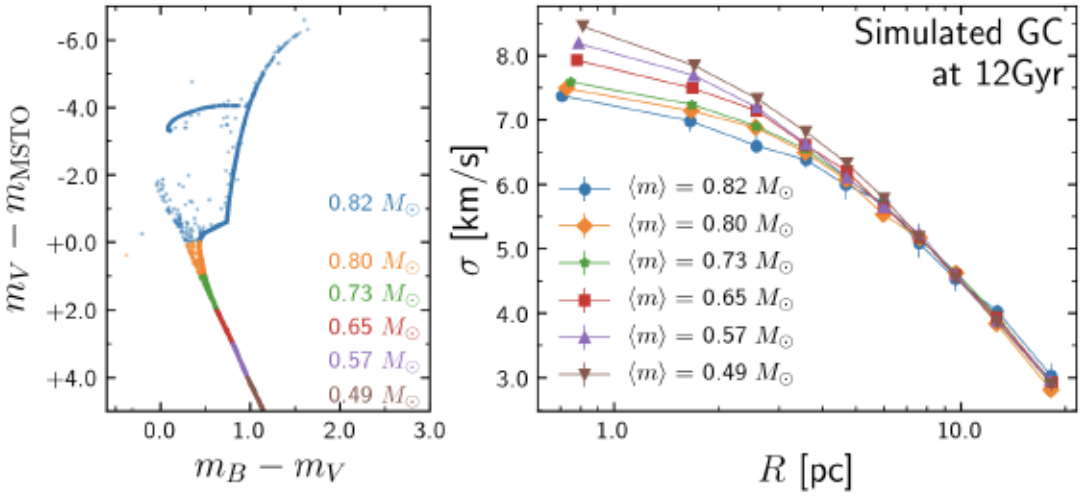

FIGURE 6.4: Color-magnitude diagram (left) and line-of-sight velocity dispersion (right) of a simulated globular cluster at an age of 12 Gyr. Different mass-populations in GCs will have a systematically different velocity dispersion due to mass segregation and energy equipartition, whose effects are stronger towards the cluster centre.

given single-mass population m_i will be:

$$\sigma_{\rm m_i,obs} = e(r, m_i) \times \sigma_{\rm m_i,\Phi}\,, \tag{6.1}$$

where $\sigma_{\rm m_i,\Phi}$ is the velocity dispersion implied by the overall potential Φ which includes the information of the variable mass-to-light ratio and $e(r)$ that represents the radial effect of energy equipartition.

Whereas disentangling the effects of the energy equipartition and the variable mass-to-light ratio is not trivial, we know that both are dependant on the dynamical age of the GCs (Bianchini et al., 2016a, 2017), and therefore, it should be possible to aim for self-consistent models that constrain the effects of both. As observations expand to lower mass stars, constraints on the level of energy equipartition will become available (Heyl et al., 2017).

Having a large set of populations can systematically increase the number of free parameters in the models, making them more challenging to constrain. For this reason, simulations will have an essential role to define the necessary observations for constraining the data. In particular, for defining which tracer for mass segregation or energy equipartition can work best along with the observed kinematics. This approach can also put constraints on the presence of stellar-mass black hole systems within the GCs as well as improve the ability to detect the presence of IMBHs. This is also relevant for gravitational wave studies, as it can provide upper limits on how many stellar-mass black holes could still exist in GCs, as well as predict their distribution.

6.2.2 Dynamics of multiple stellar populations

As discussed in Section 1.2.1, GCs have multiple stellar populations, characterized by different abundance ratios of light elements. The different populations also show unique kinematic features that not only can provide additional constraints for the dynamical modelling of the GC, but also could provide constraints for their origin. As the kinematics of these different populations could still have imprints from their formation time, they can be used to test different formation scenarios (Mastrobuono-Battisti & Perets, 2013; Hénault-Brunet et al., 2015; Tiongco et al., 2019).

One intriguing point is the difference in rotation (Cordero et al., 2017; Kamann et al., 2020a) that are expected from scenarios with extended or bursts of stellar formation, which, however, is disfavoured by the lack of an age difference between the stellar populations observed in young clusters (Martocchia et al., 2018; Saracino et al., 2020).

The dynamical models used throughout this thesis can also be adapted to consider different stellar populations, by adding chemical tags for each star. Moving forward to implement chemo-dynamical models of GCs will be the path to a better understanding of the different properties of the stellar populations. To do so, we can build on the tools developed here to analyse numerical simulation with dynamical models. By integrating simulations that follow the evolution of multiple populations (ref) with the chemical tagging described before.

In the same way, the methods discussed previously for binary stars (Chapter 4) can be extended to multiple populations, as more kinematic data for binaries becomes available (Kamann et al., 2020b). As the binary fraction in first and second-generation stars is different (Hong et al., 2015, 2016; Milone et al., 2020), the question that follows is: how does it affect the observed kinematics of each population and the difference in velocity dispersion? Also, do mixed population binaries have any impact on the observed kinematics? Simulations of GCs with multiple stellar populations with binaries (Hong et al., 2015, 2016) will be crucial for answering these questions.

* * * * * *

To conclude, I have for the first time carried out an independent analysis to quantify the reliability of dynamical models based on the Jeans equation to discover IMBHs in GCs and describe the cases when this method works efficiently. Furthermore, I have introduced a new method to utilise binaries in GCs to discover IMBHs. This approach allows us to distinguish between clusters that might or might not harbour an IMBH. Additionally, I have studied the effect of the overall binary population, finding that contamination by unknown binary stars can overestimate IMBH masses. Finally, I show that by using the dynamical modelling as it exists today (with constant mass-to-light

ratio) and taking care of the treatment of binaries, only IMBHs with mass fraction larger than 2% can robustly be detected. All these results are crucial in understanding current and upcoming observations in the centres of GCs. Finally, I have introduced a selection of possible follow-up projects.

Appendix A

Additional material for Chapter 3

A.1 Additional figures

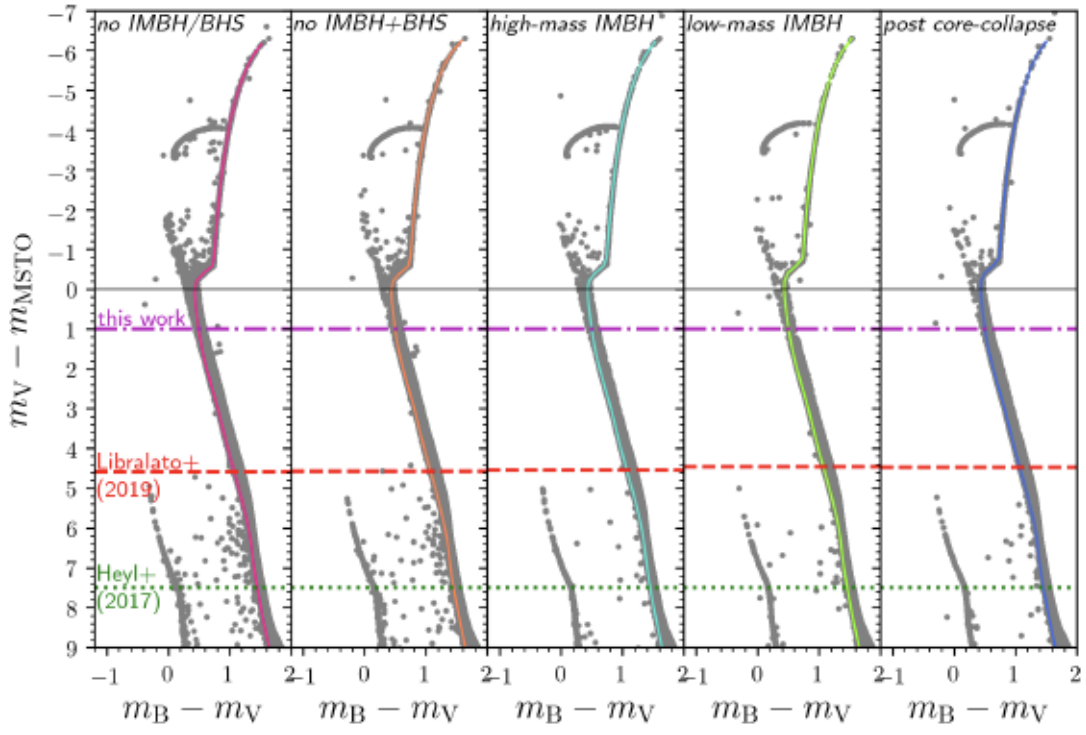

FIGURE A.1: CMD for all five GC simulations, each of them centred at their respective MSTO magnitude. Our selection on magnitude is represented by the dot-dashed line and it is equivalent to select all stars brighter than $m_V \sim 18.5$ at a distance of 5 kpc (as described in Section 3.3.1) and follows the magnitude limit in Watkins et al. (2015) for HST proper motions. For comparison we include limits from HST data for the central (Libralato et al., 2018, for NGC 362) and outer (Heyl et al., 2017, for NGC 104) regions of a GC.

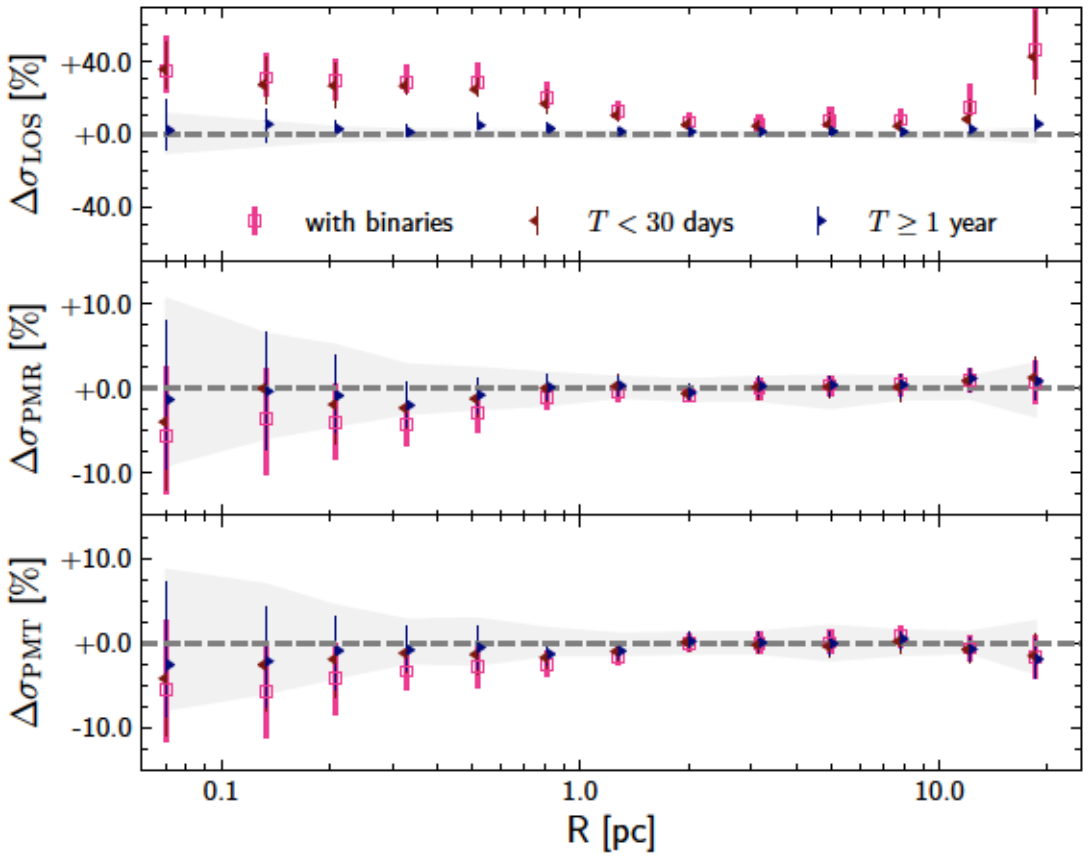

FIGURE A.2: Difference in velocity dispersion for different binary populations relative to the sample without binaries, for the *no IMBH/BHS* simulation (as in Figure 3.4). Binary systems have different effects in the velocity dispersion for each type of kinematic data. The observed line-of-sight (LOS) velocity of binary systems is mostly dominated by their internal orbital velocity, which translate in a increase in the measured velocity dispersion and it is mostly dominated by short period binaries ($T < 30$ days). On the other hand, proper motions (radial (PMR) and tangential (PMT) components) are not affected by the internal orbital motion of each component, rather the measured velocity dispersion will be affected by the level of energy equipartition of the binary systems.

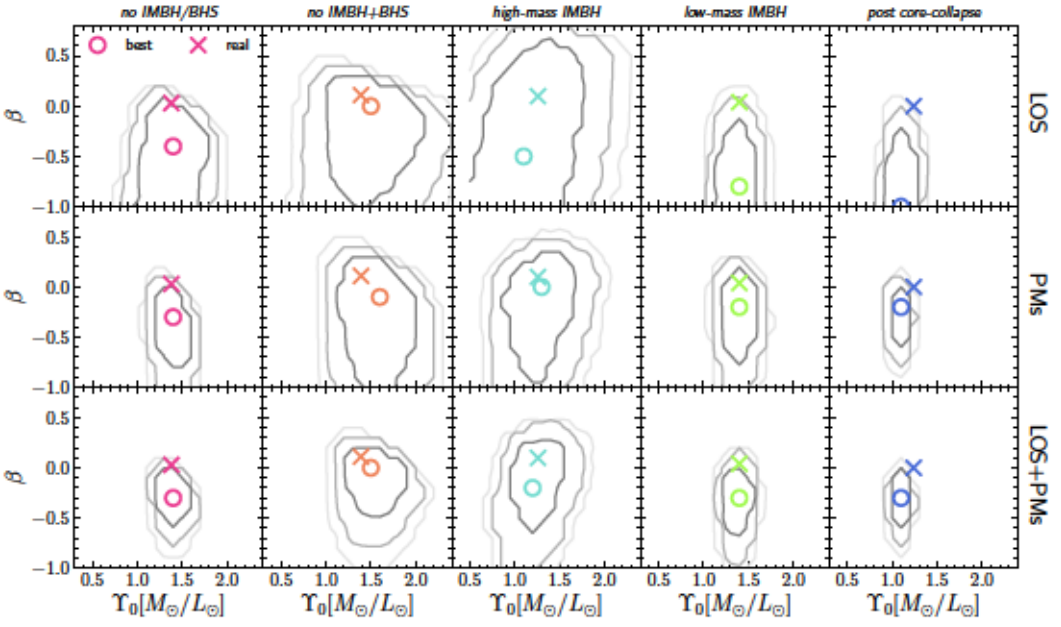

FIGURE A.3: Parameter space for the mass-to-light ratio and velocity anisotropy, for all simulations and kinematic data used for the fit. The contours represent the confidence regions we defined to trace the errors, while the open circle represent the best-fit value in each case and the x represent the value masured directly from the simulations within the half-mass radius. For most of the simulations the constraints improve while including more kinematic data. This is not the case for the high-mass IMBH model, where the constraints in the velocity anisotropy do not improve when including proper motions. The central shape of second velocity moment is significantly dominated by the IMBH, the changes due different velocity anisotropy values are watered-down by the presence of the high-mass IMBH.

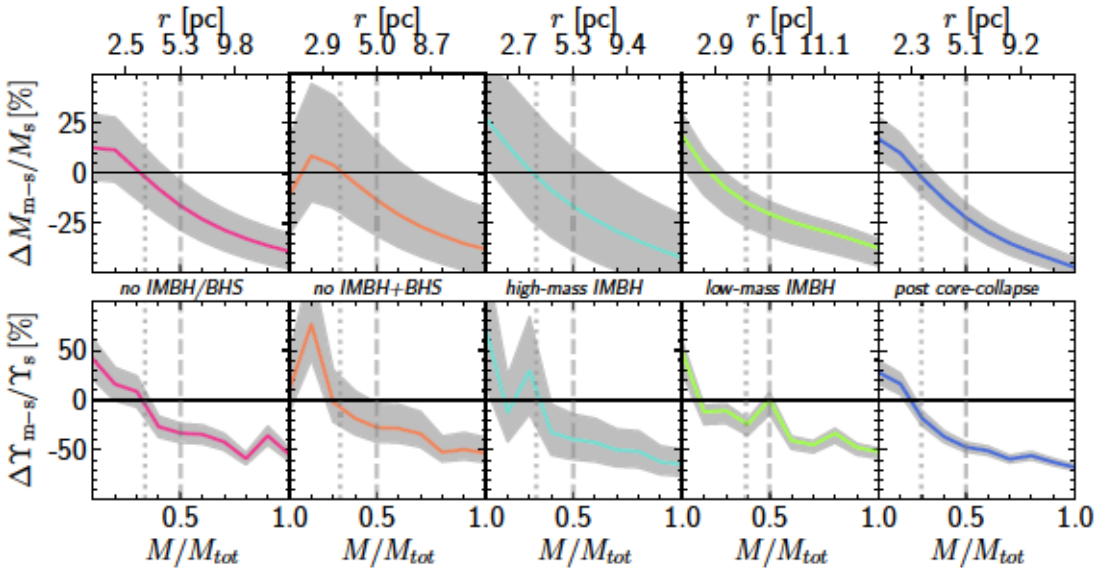

FIGURE A.4: Mass and mass-to-light error per radius for all simulated GCs. For all plots, the x-axis is in mass-fraction of the cluster from the centre (langrangian radii). The half-mass radius is marked as a vertical dashed line, the deprojected half-light radius is marked as a dotted line. The gray area represents the range of models with $\Delta\chi^2 \leq 7.8$ and the coloured line represent the best fit model. On top we illustrate the values in parsec for three langrangian radii as reference. In the top panels we see that for all five simulated GCs we systematically underestimate the total mass, while overestimating the inner regions (as we represented the profiles in mass-fraction, we are unable to observe the innermost region where the IMBH is relevant). The mass profile errors behavior by radius is tightly correlated to the difference between our assumed constant mass-to-light ratio and the one from the simulation (bottom panels). In all simulated GCs, the models and the simulations are in agreement (low relative error) around the half-light radius.

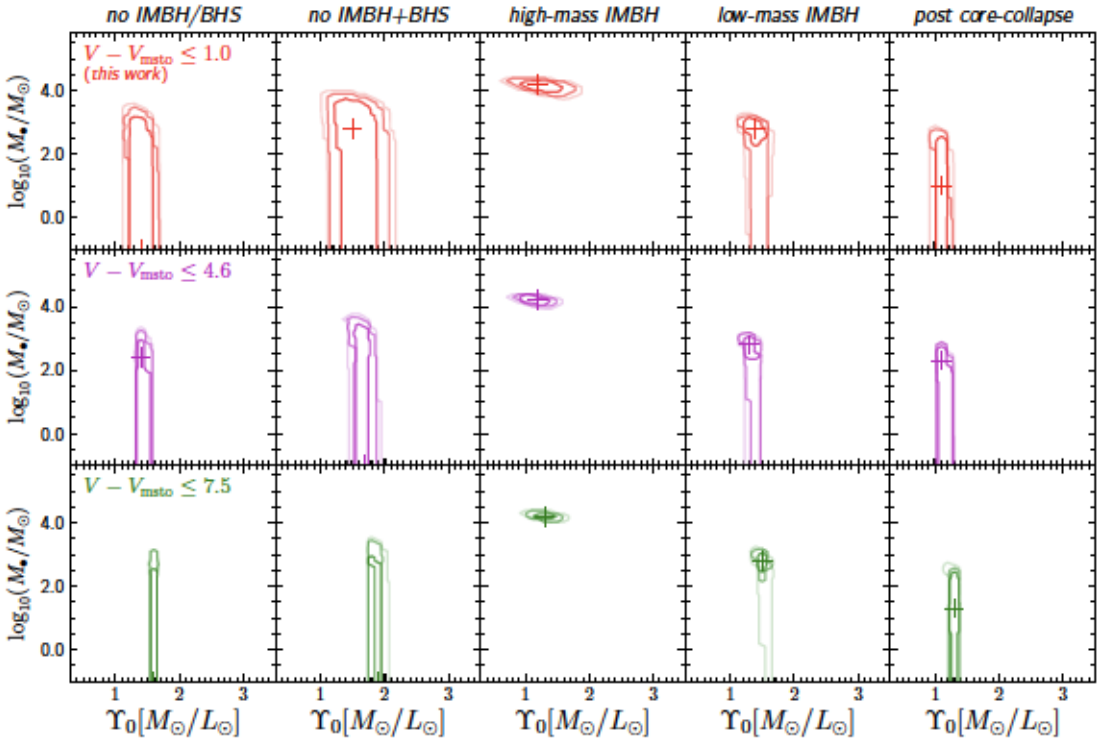

FIGURE A.5: Constraints on the mass-to-light ratio and mass of the possible central IMBH for all simulated GCs (each column), considering the full kinematic sample (as in Figure 3.9). Each row indicate a different selection sample in magnitude following the limits in Figure A.1. The constraints are consistent for all cases. Although the second and third row are beyond the current limits for line-of-sight velocities, while the third is only possible outside R_h, this comparison shows that the limitations in the modelling described in this work are intrinsic to the model and do not depend on the selected sample. For the *high-mass IMBH* and *low-mass IMBH*, the best-fit values are consistent with the expected values. On the other hand, for the three GCs without a central IMBH the best-fit values of the possible central IMBH do not converge. Once deeper observations are available allowing for a fainter limit in the luminosity cut, the Jeans modelling will automatically produce better results as our stochastic errors decrease with more stars in each bin.

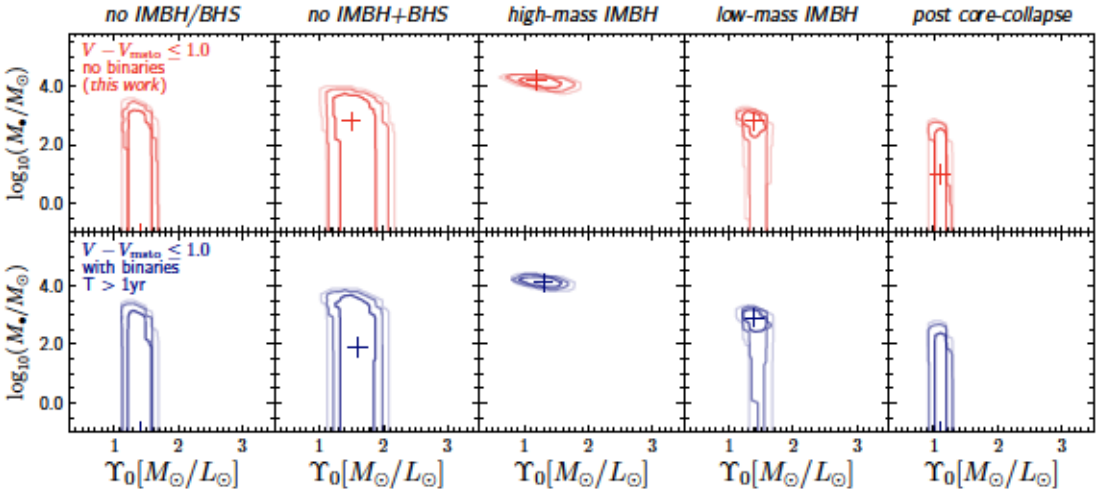

FIGURE A.6: As in Figure A.5, but considering different binary samples. The first row corresponds to the case without binaries as in our main analysis, while the bottom row shows the case when long period binaries ($T > 1\,\mathrm{yr}$) remains in the kinematic sample. The constraints from both cases are similar. As shown in panel (b) of Figure 3.4, the sample with contamination from long period binaries is consistent with the case without binaries (within errors), which is reflected on the parameter space.

Appendix B

Additional material for Chapter 4

B.1 Observational errors

In this study we have included observational errors and noise to the kinematics. For each simulated cluster we have the 3-dimensional velocities to which we add a noise accordingly the observational error expected for either the line-of-sight velocity or the proper motions. In both cases the *observed* velocity will be given by:

$$\mathrm{v}_{\mathrm{obs}} = \mathrm{v}_{\mathrm{sim}} + N(0, \delta^2)\,, \tag{B.1}$$

where $\mathrm{v}_{\mathrm{sim}}$ is the velocity from the simulation and $N(0, \delta^2)$ is a value randomly sampled form a Gaussian distribution centred in 0 with dispersion given by the observational error δ. The later serve as a noise due the observational errors.

In the case of the line-of-sight velocities we use the observational errors of MUSE/VLT data from Giesers et al. (2019). We bin the observed stars by magnitude and get the median error in each magnitude bin, Figure B.1 shows the distribution of errors and their median value. We use the V magnitude of each star in the simulation to assign an error and scatter, assuming the cluster is at a distance of 5 kpc.

We use a fix error of $\delta_{\mathrm{pm}} = 0.1$ mas/yr, taken from Libralato et al. (2018) for improved HST astrometry. We transform this value to km/s assuming the clusters are at a distance of 5 kpc.

As we added a noise to the observed kinematics we use the following likelihood approach to obtain the intrinsic velocity dispersion σ and mean velocitiy $\overline{\mathrm{v}}$:

$$\mathcal{L}(\sigma, \overline{\mathrm{v}} | \vec{\mathrm{v}}_{\mathrm{obs}}) = \prod_{i=0}^{N} \frac{1}{\sqrt{2\pi(\sigma^2 + \delta_i^2)}} \exp\left(\frac{(\mathrm{v}_{\mathrm{obs},i} - \overline{\mathrm{v}})^2}{2(\sigma^2 + \delta_i^2)}\right) \tag{B.2}$$

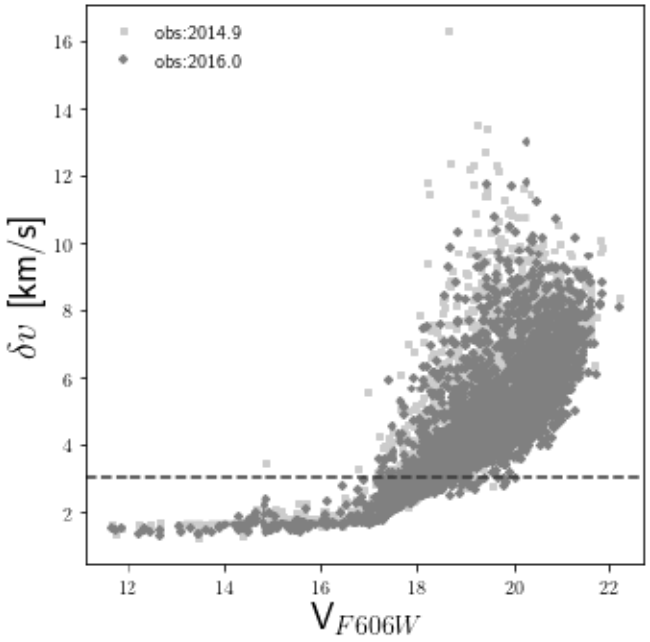

FIGURE B.1: Observational errors of line-of-sight radial velocities for NGC3201 from Giesers et al. (2019). The red line represent the median error value at different magnitude bins. The vertical dash line represent the error limit for kinematics in this work, assuming a maximum error of $\delta \sim 3\,\mathrm{km/s}$.

B.2 Gobular clusters hosting a black hole subsystem

In Figure 4.8 we show the binary fraction within the core radius and outside the half-mass radius for a sample of Galactic GCs (Milone et al., 2012a). We have cross-matched these clusters with the list of candidate Galactic GCs from Askar et al. (2018b) and Weatherford et al. (2020) to find those which have retained stellar mass black holes (BHs). We notice that indeed the candidate GCs fall closer to the 1-to-1 ratio of binary fractions (see Figure 4.8). We define an orthogonal distance to the 1-to-1 line, for each cluster in the sample, as:

$$\Delta = \frac{f_{\rm bin}(R < R_{\rm c}) - f_{\rm bin}(R > R_{\rm hm})}{\sqrt{2}}\,. \tag{B.3}$$

In Table B.1 we summarize the clusters used in Figure 4.8, indicating their names, binary fractions (core $f_{\rm c}$ and half-mass $f_{\rm hm}$) from Milone et al. (2012a), the distance from the 1-to-1 relation Δ. We have highlighted in bold face the clusters that have an off-set of $\Delta < 5$, which is below the median value for the distances to the 1-to-1 relation. We also include the number of retained BHs ($N_{\rm BHs}$) and the total mass of the retained BHs ($M_{\rm BHS}$) from both Askar et al. (2018b) and Weatherford et al. (2020). We include estimated mass of a central IMBH for three GCs in the sample with possible IMBHs in their centre.

TABLE B.1: Galactic globular clusters in Figure 4.8. For each cluster we show its name (GC), the binary fractions within the core radius f_c and outside the half-mass radius f_{hm} from Milone et al. (2012a)[a]. Both binary fraction from We calculated the distance Δ between each GC and the 1-to-1 line, and highlight those which has $\Delta < 5$. For the candidates clusters from Askar et al. (2018b)[b] and Weatherford et al. (2020)[c] we include the estimated number of retained BHs N_{BHs} and the total mass in BHs M_{BHs}. IMBH masses (M_{IMBH}) come from Kamann et al. (2014)[d] and Kamann et al. (2016)[e].

GC	$f_c^{(a)}$ [%]	$f_{hm}^{(a)}$ [%]	Δ	$N_{BHs}^{(b)}$	$M_{BHs}^{(b)}[M_\odot]$	$N_{BHs}^{(c)}$	$M_{BHs}^{(c)}[M_\odot]$	$M_{IMBH}[M_\odot]$
ARP 2	18.6 ± 2.0	18.2 ± 6.2	**0.3**					
E 3	72.0 ± 8.6	16.4 ± 21.4	39.3					
NGC 288	11.2 ± 1.0	18.4 ± 8.0	5.1	118^{+58}_{-35}	1473.0^{+566}_{-354}	26^{-14}_{+52}	594^{-305}_{+1216}	
NGC 1261	4.6 ± 1.8	4.0 ± 0.6	**0.4**			39^{-20}_{+81}	845^{-416}_{+1742}	
NGC 2298	15.4 ± 1.8	9.4 ± 0.8	**4.2**			1^{+0}_{+3}	21^{-4}_{+80}	
NGC 4147	26.2 ± 9.4	3.8 ± 1.2	15.8			2^{+0}_{+9}	55^{-9}_{+235}	
NGC 4590	11.4 ± 1.2	10.6 ± 1.4	**0.6**	71^{+29}_{-18}	847.8^{260}_{-166}	17^{-6}_{+38}	338^{-103}_{+888}	
NGC 5272	5.4 ± 1.4	3.8 ± 0.6	**1.1**	55^{+20}_{-13}	632.9^{+169}_{-109}	25^{-4}_{+112}	587^{-71}_{+2786}	$< 5.3 \times 10^3(d)$
NGC 5466	14.2 ± 0.8	3.2 ± 7.0	7.8	191^{+110}_{-63}	2512.2^{+1165}_{-703}	19^{-10}_{+67}	423^{-197}_{+1740}	
NGC 5927	10.4 ± 1.8	1.2 ± 0.6	6.5			123^{-69}_{+273}	2499^{-1320}_{+6110}	
NGC 6101	10.0 ± 0.8	10.8 ± 1.4	**0.6**	89^{+40}_{-24}	1085.6^{+370}_{-234}	125^{-104}_{+236}	3051^{-2497}_{+5880}	
NGC 6144	13.2 ± 1.2	6.0 ± 1.4	5.1	84^{+40}_{-23}	1012.2^{+335}_{-213}	13^{-7}_{+36}	299^{-144}_{+855}	
NGC 6205	1.0 ± 0.6	2.4 ± 0.6	**1.0**	34^{+10}_{-6}	366.8^{+72}_{-46}	128^{-61}_{+345}	2786^{-1178}_{+8444}	$< 8.1 \times 10^3(d)$
NGC 6218	11.4 ± 1.0	2.2 ± 2.6	6.5			22^{-11}_{+65}	509^{-233}_{+1507}	
NGC 6254	7.8 ± 0.8	5.4 ± 1.4	**1.7**			30^{-12}_{+69}	622^{-206}_{+1612}	
NGC 6352	18.4 ± 1.6	7.8 ± 3.4	7.5			14^{-5}_{+39}	298^{-98}_{+875}	
NGC 6362	12.0 ± 0.8	6.4 ± 7.4	**4.0**	86^{+38}_{-23}	1039.3^{+238}_{-221}			
NGC 6397	7.0 ± 3.6	2.8 ± 5.2	**3.0**			3^{+0}_{+16}	72^{+0}_{+421}	$600 \pm 200(e)$
NGC 6496	17.8 ± 1.2	9.2 ± 4.8	6.1	58^{+22}_{-14}	672.2^{+185}_{-119}			
NGC 6535	9.2 ± 3.2	5.6 ± 2.0	**2.5**			1^{+0}_{+5}	24^{-2}_{+125}	
NGC 6584	9.0 ± 1.2	5.0 ± 0.6	**2.8**	40^{+13}_{-8}	451.5^{+101}_{-64}	11^{-3}_{+29}	231^{-61}_{+687}	
NGC 6637	12.4 ± 2.0	2.6 ± 0.6	6.9			58^{-25}_{+123}	1154^{-478}_{+2728}	
NGC 6652	34.4 ± 11.0	5.4 ± 1.2	20.5			5^{-1}_{+22}	107^{-13}_{+501}	
NGC 6723	6.2 ± 0.8	3.4 ± 0.8	**2.0**	51^{+18}_{-11}	577.7^{+147}_{-95}	60^{-24}_{+189}	1243^{-491}_{+4528}	
NGC 6779	10.0 ± 1.8	4.6 ± 0.6	**3.8**	48^{+17}_{-11}	543.1^{220}_{-141}	51^{-24}_{+103}	1068^{-430}_{+2329}	
NGC 6838	30.4 ± 3.4	20.8 ± 2.8	6.8			17^{-6}_{+60}	363^{-119}_{+1446}	
NGC 6981	9.8 ± 1.8	6.8 ± 1.2	**2.1**	84^{+37}_{-22}	1010.6^{+334}_{-212}	27^{-17}_{+61}	573^{-334}_{+1747}	
NGC 7099	7.0 ± 3.0	2.6 ± 0.6	**3.1**			5^{+0}_{+28}	130^{-1}_{+714}	
PALOMAR 1	66.6 ± 19.2	19.0 ± 6.2	33.7					
PALOMAR 12	26.0 ± 11.4	13.2 ± 3.8	9.1					
TERZAN 7	37.4 ± 3.4	17.6 ± 2.2	14.0					
TERZAN 8	16.6 ± 2.2	11.8 ± 1.8	**3.4**					

Published Works

- **Dynamical modelling of globular clusters: challenges for the robust determination of IMBH candidate**

  F.I. Aros, A. C. Sippel, A. Mastrobuono-Battisti, A. Askar, P. Bianchini and G. van de Ven.

  Monthly Notices of the Royal Astronomical Society, Volume 499, Issue 4, December 2020, Pages 4646–4665, `https://doi.org/10.1093/mnras/staa2821`

Bibliography

Aarseth S. J., 1963, MNRAS, 126, 223

Aarseth S. J., 1999, PASP, 111, 1333

Abbott R., et al., 2020a, Phys. Rev. Lett., 125, 101102

Abbott R., et al., 2020b, The Astrophysical Journal, 900, L13

Alfaro-Cuello M., et al., 2019, ApJ, 886, 57

Alfaro-Cuello M., et al., 2020, ApJ, 892, 20

Amaro-Seoane P., Konstantinidis S., Brem P., Catelan M., 2013, MNRAS, 435, 809

Anderson J., van der Marel R. P., 2010, ApJ, 710, 1032

Anderson S. B., Gorham P. W., Kulkarni S. R., Prince T. A., Wolszczan A., 1990, Nature, 346, 42

Arca Sedda M., Askar A., Giersz M., 2018, MNRAS, 479, 4652

Arca Sedda M., Askar A., Giersz M., 2019, arXiv e-prints, p. arXiv:1905.00902

Aros F. I., Sippel A. C., Mastrobuono-Battisti A., Askar A., Bianchini P., van de Ven G., 2020, MNRAS, 499, 4646

Askar A., Szkudlarek M., Gondek-Rosińska D., Giersz M., Bulik T., 2017, MNRAS, 464, L36

Askar A., Giersz M., Pych W., Dalessand ro E., 2018a, MNRAS, 475, 4170

Askar A., Arca Sedda M., Giersz M., 2018b, MNRAS, 478, 1844

Askar A., Davies M. B., Church R. P., 2021, MNRAS, 502, 2682

Bañados E., et al., 2018, Nature, 553, 473

Bahramian A., et al., 2017, MNRAS, 467, 2199

Balick B., Brown R. L., 1974, ApJ, 194, 265

Bastian N., Lardo C., 2018, ARA&A, 56, 83

Baumgardt H., 2001, MNRAS, 325, 1323

Baumgardt H., 2017, MNRAS, 464, 2174

Baumgardt H., Hilker M., 2018, MNRAS, 478, 1520

Baumgardt H., Makino J., 2003, MNRAS, 340, 227

Baumgardt H., Hut P., Makino J., McMillan S., Portegies Zwart S., 2003, ApJ, 582, L21

Baumgardt H., Makino J., Ebisuzaki T., 2004, ApJ, 613, 1143

Baumgardt H., Makino J., Hut P., 2005, ApJ, 620, 238

Baumgardt H., Hilker M., Sollima A., Bellini A., 2019a, MNRAS, 482, 5138

Baumgardt H., et al., 2019b, MNRAS, 488, 5340

Beckert T., Duschl W. J., Mezger P. G., Zylka R., 1996, A&A, 307, 450

Belczynski K., Kalogera V., Bulik T., 2002, ApJ, 572, 407

Belczynski K., et al., 2016, A&A, 594, A97

Bellini A., Bedin L. R., Piotto G., Milone A. P., Marino A. F., Villanova S., 2010, AJ, 140, 631

Bellini A., et al., 2014, ApJ, 797, 115

Belokurov V., et al., 2020, MNRAS, 496, 1922

Berczik P., et al., 2011, in International conference on High Performance Computing. pp 8–18

Bianchini P., Varri A. L., Bertin G., Zocchi A., 2013, ApJ, 772, 67

Bianchini P., Norris M. A., van de Ven G., Schinnerer E., 2015, MNRAS, 453, 365

Bianchini P., van de Ven G., Norris M. A., Schinnerer E., Varri A. L., 2016a, MNRAS, 458, 3644

Bianchini P., Norris M. A., van de Ven G., Schinnerer E., Bellini A., van der Marel R. P., Watkins L. L., Anderson J., 2016b, ApJ, 820, L22

Bianchini P., Sills A., van de Ven G., Sippel A. C., 2017, MNRAS, 469, 4359

Bianchini P., van der Marel R. P., del Pino A., Watkins L. L., Bellini A., Fardal M. A., Libralato M., Sills A., 2018, MNRAS, 481, 2125

Bianchini P., Ibata R., Famaey B., 2019a, arXiv e-prints, p. arXiv:1912.02195

Bianchini P., Ibata R., Famaey B., 2019b, ApJ, 887, L12

Binney J., Mamon G. A., 1982, MNRAS, 200, 361

Binney J., Tremaine S., 2008, Galactic Dynamics: Second Edition. Princeton University Press

Bonaca A., Hogg D. W., Price-Whelan A. M., Conroy C., 2019, ApJ, 880, 38

Breen P. G., Heggie D. C., 2013a, MNRAS, 432, 2779

Breen P. G., Heggie D. C., 2013b, MNRAS, 436, 584

Brodie J. P., Strader J., 2006, ARA&A, 44, 193

Brown R. L., Liszt H. S., 1984, ARA&A, 22, 223

Camilo F., Lorimer D. R., Freire P., Lyne A. G., Manchester R. N., 2000, ApJ, 535, 975

Carretta E., Gratton R. G., Clementini G., Fusi Pecci F., 2000, ApJ, 533, 215

Carretta E., et al., 2009, A&A, 505, 117

Chatterjee S., Fregeau J. M., Umbreit S., Rasio F. A., 2010, ApJ, 719, 915

Chatterjee S., Rasio F. A., Sills A., Glebbeek E., 2013, ApJ, 777, 106

Cheng Z., Li Z., Li X., Xu X., Fang T., 2019a, ApJ, 876, 59

Cheng Z., Li Z., Fang T., Li X., Xu X., 2019b, ApJ, 883, 90

Chomiuk L., Strader J., Maccarone T. J., Miller-Jones J. C. A., Heinke C., Noyola E., Seth A. C., Ransom S., 2013, ApJ, 777, 69

Chun S.-H., et al., 2010, AJ, 139, 606

Claydon I., Gieles M., Varri A. L., Heggie D. C., Zocchi A., 2019, MNRAS, 487, 147

Cordero M. J., Hénault-Brunet V., Pilachowski C. A., Balbinot E., Johnson C. I., Varri A. L., 2017, MNRAS, 465, 3515

Cote P., Fischer P., 1996, AJ, 112, 565

Da Costa G. S., Freeman K. C., 1976, ApJ, 206, 128

Dage K. C., Zepf S. E., Bahramian A., Kundu A., Maccarone T. J., Peacock M. B., 2018, ApJ, 862, 108

Dalessandro E., et al., 2018, ApJ, 864, 33

Dullo B. T., Gil de Paz A., Knapen J. H., 2021, ApJ, 908, 134

Duquennoy A., Mayor M., 1991, A&A, 500, 337

Ebisuzaki T., et al., 2001, ApJ, 562, L19

Eckart A., Genzel R., Ott T., Schödel R., 2002, MNRAS, 331, 917

Ernst A., Glaschke P., Fiestas J., Just A., Spurzem R., 2007, MNRAS, 377, 465

Ernst A., Just A., Spurzem R., 2009, MNRAS, 399, 141

Farrell S. A., Webb N. A., Barret D., Godet O., Rodrigues J. M., 2009, Nature, 460, 73

Feldmeier A., et al., 2013, A&A, 554, A63

Ferrarese L., Merritt D., 2000, ApJ, 539, L9

Ferraro F. R., et al., 2012, Nature, 492, 393

Ferraro F. R., et al., 2018, ApJ, 860, 36

Foreman-Mackey D., Hogg D. W., Lang D., Goodman J., 2013, PASP, 125, 306

Fragione G., Gualandris A., 2019, MNRAS, 489, 4543

Fragione G., Loeb A., Rasio F. A., 2020, ApJ, 902, L26

Fregeau J. M., Gürkan M. A., Joshi K. J., Rasio F. A., 2003, ApJ, 593, 772

Fregeau J. M., Cheung P., Portegies Zwart S. F., Rasio F. A., 2004, MNRAS, 352, 1

Freire P. C. C., 2013, in van Leeuwen J., ed., Vol. 291, Neutron Stars and Pulsars: Challenges and Opportunities after 80 years. pp 243–250 (arXiv:1210.3984), doi:10.1017/S1743921312023770

Fukushige T., Heggie D. C., 2000, MNRAS, 318, 753

Gaia Collaboration et al., 2016, A&A, 595, A1

Gaia Collaboration et al., 2018, A&A, 616, A1

Gavagnin E., Mapelli M., Lake G., 2016, MNRAS, 461, 1276

Gebhardt K., et al., 2000, ApJ, 539, L13

Gebhardt K., Rich R. M., Ho L. C., 2002, ApJ, 578, L41

Gebhardt K., Rich R. M., Ho L. C., 2005, ApJ, 634, 1093

Genzel R., Eckart A., Ott T., Eisenhauer F., 1997, MNRAS, 291, 219

Georgiev I. Y., Böker T., 2014, MNRAS, 441, 3570

Gerssen J., van der Marel R. P., Gebhardt K., Guhathakurta P., Peterson R. C., Pryor C., 2002, AJ, 124, 3270

Ghez A. M., Klein B. L., Morris M., Becklin E. E., 1998, ApJ, 509, 678

Ghez A. M., Morris M., Becklin E. E., Tanner A., Kremenek T., 2000, Nature, 407, 349

Ghez A. M., et al., 2008, ApJ, 689, 1044

Gieles M., Zocchi A., 2015, MNRAS, 454, 576

Giersz M., 1998, MNRAS, 298, 1239

Giersz M., 2001, MNRAS, 324, 218

Giersz M., Spurzem R., 2000, MNRAS, 317, 581

Giersz M., Heggie D. C., Hurley J. R., 2008, MNRAS, 388, 429

Giersz M., Heggie D. C., Hurley J. R., Hypki A., 2013, MNRAS, 431, 2184

Giersz M., Leigh N., Hypki A., Lützgendorf N., Askar A., 2015, MNRAS, 454, 3150

Giesers B., et al., 2018, MNRAS, 475, L15

Giesers B., et al., 2019, arXiv e-prints, p. arXiv:1909.04050

Gill M., Trenti M., Miller M. C., van der Marel R., Hamilton D., Stiavelli M., 2008a, ApJ, 686, 303

Gill M., Trenti M., Miller M. C., van der Marel R., Hamilton D., Stiavelli M., 2008b, ApJ, 686, 303

Gomez-Leyton Y. J., Velazquez L., 2019, MNRAS, 488, 362

González E., Kremer K., Chatterjee S., Fragione G., Rodriguez C. L., Weatherford N. C., Ye C. S., Rasio F. A., 2021, ApJ, 908, L29

Gratton R., Bragaglia A., Carretta E., D'Orazi V., Lucatello S., Sollima A., 2019, A&ARv, 27, 8

Gravity Collaboration et al., 2018a, A&A, 615, L15

Gravity Collaboration et al., 2018b, A&A, 618, L10

Greene J. E., Strader J., Ho L. C., 2020, ARA&A, 58, 257

Grillmair C. J., Freeman K. C., Irwin M., Quinn P. J., 1995, AJ, 109, 2553

Gürkan M. A., Freitag M., Rasio F. A., 2004, ApJ, 604, 632

Haiman Z., 2013, The Formation of the First Massive Black Holes. p. 293, doi:10.1007/978-3-642-32362-1˙6

Harris W. E., 1996, AJ, 112, 1487

Harris W. E., van den Bergh S., 1981, AJ, 86, 1627

Heggie D. C., 1984, MNRAS, 206, 179

Heggie D. C., 2001, in Deiters S., Fuchs B., Just A., Spurzem R., Wielen R., eds, Astronomical Society of the Pacific Conference Series Vol. 228, Dynamics of Star Clusters and the Milky Way. p. 29 (arXiv:astro-ph/0007336)

Heggie D. C., Aarseth S. J., 1992, MNRAS, 257, 513

Heggie D. C., Giersz M., 2014, MNRAS, 439, 2459

Heggie D., Hut P., 2003, The Gravitational Million-Body Problem: A Multidisciplinary Approach to Star Cluster Dynamics

Heggie D. C., Trenti M., Hut P., 2006, MNRAS, 368, 677

Hénault-Brunet V., Gieles M., Agertz O., Read J. I., 2015, MNRAS, 450, 1164

Hénault-Brunet V., Gieles M., Strader J., Peuten M., Balbinot E., Douglas K. E. K., 2019a, arXiv e-prints, p. arXiv:1908.08538

Hénault-Brunet V., Gieles M., Sollima A., Watkins L. L., Zocchi A., Claydon I., Pancino E., Baumgardt H., 2019b, MNRAS, 483, 1400

Hénon M., 1971a, Ap&SS, 13, 284

Hénon M. H., 1971b, Ap&SS, 14, 151

Heyl J., Caiazzo I., Richer H., Anderson J., Kalirai J., Parada J., 2017, ApJ, 850, 186

Hills J. G., 1988, Nature, 331, 687

Hobbs G., Lorimer D. R., Lyne A. G., Kramer M., 2005, MNRAS, 360, 974

Hong J., Vesperini E., Sollima A., McMillan S. L. W., D'Antona F., D'Ercole A., 2015, MNRAS, 449, 629

Hong J., Vesperini E., Sollima A., McMillan S. L. W., D'Antona F., D'Ercole A., 2016, MNRAS, 457, 4507

Hong J., Vesperini E., Askar A., Giersz M., Szkudlarek M., Bulik T., 2018, MNRAS, 480, 5645

Hong J., Askar A., Giersz M., Hypki A., Yoon S.-J., 2020, MNRAS, 498, 4287

Hurley J. R., Pols O. R., Tout C. A., 2000, MNRAS, 315, 543

Hurley J. R., Tout C. A., Pols O. R., 2002, MNRAS, 329, 897

Hurley J. R., Aarseth S. J., Shara M. M., 2007, ApJ, 665, 707

Hurley J. R., et al., 2008, AJ, 135, 2129

Hut P., 2003, in Makino J., Hut P., eds, Vol. 208, Astrophysical Supercomputing using Particle Simulations. p. 331 (arXiv:astro-ph/0204431)

Hypki A., Giersz M., 2013, MNRAS, 429, 1221

Hypki A., Giersz M., 2017, MNRAS, 471, 2537

Inayoshi K., Visbal E., Haiman Z., 2020, ARA&A, 58, 27

Jahnke K., Macciò A. V., 2011, ApJ, 734, 92

Jeans J. H., 1915, MNRAS, 76, 70

Jeans J. H., 1922, MNRAS, 82, 122

Ji J., Bregman J. N., 2015, ApJ, 807, 32

Jordi K., Grebel E. K., 2010, A&A, 522, A71

Kaderali S., Hunt J. A. S., Webb J. J., Price-Jones N., Carlberg R., 2019, MNRAS, 484, L114

Kamann S., Wisotzki L., Roth M. M., Gerssen J., Husser T. O., Sandin C., Weilbacher P., 2014, A&A, 566, A58

Kamann S., et al., 2016, A&A, 588, A149

Kamann S., et al., 2018, MNRAS, 473, 5591

Kamann S., et al., 2020a, MNRAS, 492, 966

Kamann S., et al., 2020b, A&A, 635, A65

King I., 1962, AJ, 67, 471

King I. R., 1966, AJ, 71, 64

Kızıltan B., Baumgardt H., Loeb A., 2017, Nature, 542, 203

Kormendy J., Ho L. C., 2013, ARA&A, 51, 511

Kremer K., Chatterjee S., Ye C. S., Rodriguez C. L., Rasio F. A., 2019, ApJ, 871, 38

Kruijssen J. M. D., Lutzgendorf N., 2013, MNRAS, 434, L41

Kulkarni S. R., Hut P., McMillan S., 1993, Nature, 364, 421

Kunder A., et al., 2017, AJ, 153, 75

Kundu R., Navarrete C., Fernández-Trincado J. G., Minniti D., Singh H. P., Sbordone L., Piatti A. E., Reylé C., 2021, A&A, 645, A116

Küpper A. H. W., Kroupa P., Baumgardt H., Heggie D. C., 2010, MNRAS, 401, 105

Lanzoni B., et al., 2013, ApJ, 769, 107

Leigh N. W. C., Lützgendorf N., Geller A. M., Maccarone T. J., Heinke C., Sesana A., 2014, MNRAS, 444, 29

Leon S., Meylan G., Combes F., 2000, A&A, 359, 907

Libralato M., et al., 2018, ApJ, 861, 99

Liu B., Lai D., 2021, MNRAS, 502, 2049

Lützgendorf N., Kissler-Patig M., Noyola E., Jalali B., de Zeeuw P. T., Gebhardt K., Baumgardt H., 2011, A&A, 533, A36

Lützgendorf N., Kissler-Patig M., Gebhardt K., Baumgardt H., Noyola E., Jalali B., de Zeeuw P. T., Neumayer N., 2012, A&A, 542, A129

Lützgendorf N., et al., 2013a, A&A, 552, A49

Lützgendorf N., et al., 2013b, A&A, 555, A26

Lützgendorf N., Baumgardt H., Kruijssen J. M. D., 2013c, A&A, 558, A117

Lützgendorf N., Gebhardt K., Baumgardt H., Noyola E., Neumayer N., Kissler-Patig M., de Zeeuw T., 2015, A&A, 581, A1

Lynden-Bell D., Wood R., 1968, MNRAS, 138, 495

Maccarone T. J., Kundu A., Zepf S. E., Rhode K. L., 2007, Nature, 445, 183

Mackey A. D., Wilkinson M. I., Davies M. B., Gilmore G. F., 2008, MNRAS, 386, 65

Madau P., Rees M. J., 2001, ApJ, 551, L27

Madrid J. P., Leigh N. W. C., Hurley J. R., Giersz M., 2017, MNRAS, 470, 1729

Makino J., 1991, ApJ, 369, 200

Makino J., 1996, ApJ, 471, 796

Makino J., Kokubo E., Taiji M., 1993, PASJ, 45, 349

Mann C. R., et al., 2019, ApJ, 875, 1

Mapelli M., 2016, MNRAS, 459, 3432

Mapelli M., Sigurdsson S., Ferraro F. R., Colpi M., Possenti A., Lanzoni B., 2006, MNRAS, 373, 361

Martocchia S., et al., 2018, MNRAS, 477, 4696

Mashchenko S., Sills A., 2005, ApJ, 619, 243

Mastrobuono-Battisti A., Perets H. B., 2013, ApJ, 779, 85

Mastrobuono-Battisti A., Perets H. B., 2016, ApJ, 823, 61

Mastrobuono-Battisti A., Di Matteo P., Montuori M., Haywood M., 2012, A&A, 546, L7

Mastrobuono-Battisti A., Perets H. B., Loeb A., 2014, ApJ, 796, 40

Mastrobuono-Battisti A., Khoperskov S., Di Matteo P., Haywood M., 2019, A&A, 622, A86

McConnell N. J., Ma C.-P., 2013, ApJ, 764, 184

McLaughlin D. E., Anderson J., Meylan G., Gebhardt K., Pryor C., Minniti D., Phinney S., 2006, ApJS, 166, 249

McMillan S., Hut P., Makino J., 1990, ApJ, 362, 522

McNamara B. J., Harrison T. E., Anderson J., 2003, ApJ, 595, 187

McNamara B. J., Harrison T. E., Baumgardt H., Khalaj P., 2012, ApJ, 745, 175

Meylan G., Heggie D. C., 1997, A&ARv, 8, 1

Michie R. W., 1961, ApJ, 133, 781

Michie R. W., 1963, MNRAS, 126, 331

Miller M. C., Hamilton D. P., 2002, MNRAS, 330, 232

Miller-Jones J. C. A., et al., 2015, MNRAS, 453, 3918

Milone A. P., et al., 2012a, A&A, 540, A16

Milone A. P., et al., 2012b, ApJ, 744, 58

Milone A. P., et al., 2020, MNRAS, 492, 5457

Minniti D., et al., 2017, ApJ, 849, L24

Moehler S., Bono G., 2008, arXiv e-prints, p. arXiv:0806.4456

Monelli M., et al., 2005, ApJ, 621, L117

Morscher M., Umbreit S., Farr W. M., Rasio F. A., 2013, ApJ, 763, L15

Morscher M., Pattabiraman B., Rodriguez C., Rasio F. A., Umbreit S., 2015, ApJ, 800, 9

Mortlock D. J., et al., 2011, Nature, 474, 616

Neumayer N., Seth A., Böker T., 2020, A&ARv, 28, 4

Nguyen D. D., et al., 2019, ApJ, 872, 104

Nitadori K., Aarseth S. J., 2012, MNRAS, 424, 545

Noyola E., Baumgardt H., 2011, ApJ, 743, 52

Noyola E., Gebhardt K., Bergmann M., 2008, ApJ, 676, 1008

Noyola E., Gebhardt K., Kissler-Patig M., Lützgendorf N., Jalali B., de Zeeuw P. T., Baumgardt H., 2010, ApJ, 719, L60

O'Leary R. M., Rasio F. A., Fregeau J. M., Ivanova N., O'Shaughnessy R., 2006, ApJ, 637, 937

Odenkirchen M., et al., 2001, ApJ, 548, L165

Odenkirchen M., et al., 2003, AJ, 126, 2385

Pasquato M., Di Cintio P., 2020, A&A, 640, A79

Petts J. A., Gualandris A., 2017, MNRAS, 467, 3775

Peuten M., Zocchi A., Gieles M., Hénault-Brunet V., 2017, MNRAS, 470, 2736

Piotto G., et al., 2007, ApJ, 661, L53

Plummer H. C., 1911, MNRAS, 71, 460

Pooley D., Rappaport S., 2006, ApJ, 644, L45

Portegies Zwart S. F., McMillan S. L. W., 2002, ApJ, 576, 899

Portegies Zwart S. F., Makino J., McMillan S. L. W., Hut P., 1999, A&A, 348, 117

Portegies Zwart S. F., Baumgardt H., Hut P., Makino J., McMillan S. L. W., 2004, Nature, 428, 724

Portegies Zwart S. F., Baumgardt H., McMillan S. L. W., Makino J., Hut P., Ebisuzaki T., 2006, ApJ, 641, 319

Pryor C. P., Latham D. W., Hazen M. L., 1988, AJ, 96, 123

Ransom S. M., 2008, in Vesperini E., Giersz M., Sills A., eds, Vol. 246, Dynamical Evolution of Dense Stellar Systems. pp 291–300, doi:10.1017/S1743921308015810

Read J. I., Steger P., 2017, MNRAS, 471, 4541

Richer H. B., et al., 1997, ApJ, 484, 741

Rizzuto F. P., et al., 2021, MNRAS, 501, 5257

Rodriguez C. L., Chatterjee S., Rasio F. A., 2016, Phys. Rev. D, 93, 084029

Rogers A. E. E., et al., 1994, ApJ, 434, L59

Saracino S., et al., 2020, MNRAS, 493, 6060

Schwarzschild M., 1979, ApJ, 232, 236

Shishkovsky L., et al., 2018, ApJ, 855, 55

Sigurdsson S., Hernquist L., 1993, Nature, 364, 423

Sippel A. C., Hurley J. R., 2013, MNRAS, 430, L30

Sollima A., 2020, MNRAS, 495, 2222

Sollima A., 2021, MNRAS, 502, 1974

Sollima A., Beccari G., Ferraro F. R., Fusi Pecci F., Sarajedini A., 2007, MNRAS, 380, 781

Sollima A., Baumgardt H., Zocchi A., Balbinot E., Gieles M., Hénault-Brunet V., Varri A. L., 2015, MNRAS, 451, 2185

Sollima A., Baumgardt H., Hilker M., 2019, MNRAS, 485, 1460

Spera M., Mapelli M., 2017, MNRAS, 470, 4739

Spitzer Lyman J., 1969, ApJ, 158, L139

Spitzer L., 1987, Dynamical evolution of globular clusters. Princeton University Press

Spitzer Lyman J., Hart M. H., 1971, ApJ, 164, 399

Spurzem R., Aarseth S. J., 1996, MNRAS, 282, 19

Stodolkiewicz J. S., 1982, Acta Astron., 32, 63

Stodolkiewicz J. S., 1986, Acta Astron., 36, 19

Strader J., Chomiuk L., Maccarone T. J., Miller-Jones J. C. A., Seth A. C., 2012a, Nature, 490, 71

Strader J., Chomiuk L., Maccarone T. J., Miller-Jones J. C. A., Seth A. C., Heinke C. O., Sivakoff G. R., 2012b, ApJ, 750, L27

Sugimoto D., Chikada Y., Makino J., Ito T., Ebisuzaki T., Umemura M., 1990, Nature, 345, 33

Tiongco M. A., Vesperini E., Varri A. L., 2017, MNRAS, 469, 683

Tiongco M. A., Vesperini E., Varri A. L., 2018, MNRAS, 475, L86

Tiongco M. A., Vesperini E., Varri A. L., 2019, MNRAS, 487, 5535

Tonry J. L., 1984, ApJ, 283, L27

Tonry J. L., 1987, ApJ, 322, 632

Tremou E., et al., 2018, ApJ, 862, 16

Trenti M., van der Marel R., 2013, MNRAS, 435, 3272

Trenti M., Heggie D. C., Hut P., 2007a, MNRAS, 374, 344

Trenti M., Ardi E., Mineshige S., Hut P., 2007b, MNRAS, 374, 857

VandenBerg D. A., Brogaard K., Leaman R., Casagrande L., 2013, ApJ, 775, 134

Vandenberg D. A., Bolte M., Stetson P. B., 1996, ARA&A, 34, 461

Varri A. L., Bertin G., 2012, A&A, 540, A94

Vesperini E., Trenti M., 2010, ApJ, 720, L179

Vesperini E., McMillan S. L. W., D'Antona F., D'Ercole A., 2013, MNRAS, 429, 1913

Vesperini E., Hong J., Giersz M., Hypki A., 2021, MNRAS, 502, 4290

Vitral E., Mamon G. A., 2021, A&A, 646, A63

Volonteri M., 2010, A&ARv, 18, 279

Wang L., Spurzem R., Aarseth S., Nitadori K., Berczik P., Kouwenhoven M. B. N., Naab T., 2015, MNRAS, 450, 4070

Wang L., et al., 2016, MNRAS, 458, 1450

Watkins L. L., van der Marel R. P., Bellini A., Anderson J., 2015, ApJ, 812, 149

Weatherford N. C., Chatterjee S., Rodriguez C. L., Rasio F. A., 2018, ApJ, 864, 13

Weatherford N. C., Chatterjee S., Kremer K., Rasio F. A., 2019, arXiv e-prints, p. arXiv:1911.09125

Weatherford N. C., Chatterjee S., Kremer K., Rasio F. A., 2020, ApJ, 898, 162

Woo J.-H., Cho H., Gallo E., Hodges-Kluck E., Le H. A. N., Shin J., Son D., Horst J. C., 2019, Nature Astronomy, 3, 755

Wu X.-B., et al., 2015, Nature, 518, 512

Zhang W., Woosley S. E., Heger A., 2008, ApJ, 679, 639

Zocchi A., Bertin G., Varri A. L., 2012, A&A, 539, A65

Zocchi A., Gieles M., Hénault-Brunet V., Varri A. L., 2016, MNRAS, 462, 696

Zocchi A., Gieles M., Hénault-Brunet V., 2017, MNRAS, 468, 4429

Zocchi A., Gieles M., Hénault-Brunet V., 2019, MNRAS, 482, 4713

de Vita R., Trenti M., Bianchini P., Askar A., Giersz M., van de Ven G., 2017, MNRAS, 467, 4057

de Vita R., Trenti M., MacLeod M., 2018, MNRAS, 475, 1574

den Brok M., van de Ven G., van den Bosch R., Watkins L., 2014, MNRAS, 438, 487

Šubr L., Fragione G., Dabringhausen J., 2019, MNRAS, 484, 2974

van de Ven G., van den Bosch R. C. E., Verolme E. K., de Zeeuw P. T., 2006, A&A, 445, 513

van den Bergh S., 2008, AJ, 135, 1731

van den Bosch R. C. E., 2016, ApJ, 831, 134

van den Bosch R., de Zeeuw T., Gebhardt K., Noyola E., van de Ven G., 2006, ApJ, 641, 852

van der Marel R. P., Anderson J., 2010, ApJ, 710, 1063

von Hoerner S., 1960, Z. Astrophys., 50, 184